UCLouvain

École polytechnique de Louvain

Study of the transfer between helicity components in vortex ring configurations

Author: **Romain Rezsöhazy**
Supervisors: **Grégoire Winckelmans, Philippe Chatelain**
Reader: **Jean-François Remacle**
Academic year 2020–2021
Master [120] in Mechanical Engineering

Contents

Abstract

The present master's thesis has the aim to implement and study vortex ring configurations with the objective to characterise the evolution of their helicity content, constituting a relatively controversial dynamic quantity.

That work has been carried out within the continuity of previous master's theses tackling vortex rings evolutions, led within the Thermodynamics and Fluid Mechanics (TFL) pole of UCLouvain.

First, the framework of the present work is delineated. Dynamic quantities of interest are presented and defined, and helicity is introduced as a combination of three storage modes. The study of the possible transfer from one mode to another is then undertaken. The final objective is indeed to identify the relative stability of each mode, the exchanges between them and the potential ability for helicity to be conserved.

The three main chapters of the document thus tackle the investigation of the three constituting storage modes. Then, a chapter is dedicated to the gathering of the obtained results as a manner to describe the interactions between the helicity contents and compare them.

Finally, the point of view of the knot theory is embraced, as a tool to further analyse and describe the topologies adopted by the various initiated structures, as well as the contribution of the topology in the protection of the helicity from viscosity.

The appendices describe the implementation of the main tools developed as a part of the present investigation.

Acknowledgements

First of all, it is of high importance to me to thank the people and organisations without whom none of what follows would have been made feasible.

I sincerely want to thank my supervisors, Pr. Grégoire Winckelmans and Pr. Philippe Chatelain, who always showed true interest for the results I presented to them, guided me with kindness and benevolence and advised me all the way during my work.

Besides, I feel grateful for the precious help I received from Pierre Balty, who supervised me along my master's thesis pathway, and showed an irreproachable availability for my questions and discussions.

The computational ressources used in order to perform the simulations present in that work have been furnished by the Cenaero and by the *Consortium des Équipements de Calcul Intensif* (CÉCI), financed thanks to the *Fond National de la Recherche Scientifique de Belgique* (F.R.S.-FNRS).

Finally, I thank you, dear readers, for the attention you will pay when discovering the result of my work.

List of Figures

Introduction

Vortex rings are at the center of the attention from decades now when talking about the study of the dynamics of vortical structures. Previous master's theses led within the TFL pole of UCLouvain have tackled the study of their evolution and interaction with walls, among others. The initial goal of the present work was the investigation of a configuration with two vortex rings set in a knot-type arrangement, as it will be described in the following chapters. This linked aspect would thus add the involvement of a peculiar physical quantity: helicity.

After deepening the literature addressing the examination of the helicity content inside various vortex rings, the work has extended the exploration to further implementations of arrangements of pseudo-vortex rings, containing different traces of helicity content. Indeed, helicity constitutes a challenging quantity to capture and describe, and vortex structures are seen to constitute a highly relevant domain in order to study its behaviour.

Several inspirations for this master's thesis come from the studies led by Moffatt, which has been the first main researcher to address the subject of helicity within vortex lines, in 1968 [1]. In the early 90s, Moffat and Ricca further investigated the helicity content, with notions from the knot theory, and looked into the helicity tenor of turbulent flows.

Mathematically speaking, and as presented in the following chapters, helicity may be captured thanks to the knot theory, relative to the description of the entanglement of a curve. Călugăreanu, in 1961 [2], described the isotopy classes of knots, from which the Călugăreanu invariant is drawn. Fuller, in 1971 [3], further depicted the knottedness of a line, allowing the addition of a topological perspective to the helicity content inside some vortex tubes.

Motivations for structures implementations were also found in the studies undertaken by Scheeler and van Rees [4] [5], who experimentally generated helicity containing vortex rings, and made them evolving with the goal to understand the transformations undergone by their helicity content.

All the configurations presented in the current work, and from which the conclusions have been drawn, have been numerically implemented in the solver presented in the following Framework chapter.

Chapter 1

Framework

1.1 The VPM solver

All the simulations from which the results of the present work are obtained have been performed thanks to the state-of-the art in house-developed research code `VPM`, from the TFL pole of UCLouvain.

The vortex particle mesh method is a hybrid method using particle and mesh discretisations. The particles are used in order to discretise the Navier-Stokes equations in a vorticity-velocity formulation, in a Lagrangian form. Besides, a mesh is used to tackle the problem of the inhomogeneous distribution of the particles when the latters are used alone. The mesh is also solicited in order to perform the fast computation of the Poisson equation, using Fast Fourier Transforms (FFT), as well as the one of operators for diffusion and vortex stretching [6]. The motivation for the use of a Lagrangian method is the lower severity for the stability regarding the time steps required. Hence, the linking of it with a mesh, for computational and convergence reasons, constitutes the hybrid vortex method of the `VPM` solver.

The Navier-Stokes equations

The Navier-Stokes equations are reminded, in the case of an incompressible flow:

$$\nabla \cdot \mathbf{u} = 0 \tag{1.1}$$

$$\frac{D\,\mathbf{u}}{D\,t} = \frac{\partial \mathbf{u}}{\partial t} + \mathbf{u} \cdot \nabla \mathbf{u} = -\nabla P + \nu \nabla^2 \mathbf{u} \tag{1.2}$$

Eq. (1.2) may be expressed in its vorticity formulation (developments are omitted):

$$\frac{D\,\boldsymbol{\omega}}{D\,t} = (\boldsymbol{\omega} \cdot \nabla)\,\mathbf{u} \;+\; \nu \nabla^2 \boldsymbol{\omega} \tag{1.3}$$

With $\boldsymbol{\omega}$ the vorticity, defined as

$$\boldsymbol{\omega} = \nabla \times \mathbf{u} \tag{1.4}$$

And where the material derivative of the vorticity is seen as being the result of a **stretching** term and a **diffusion** term. It is important to stress that the stretching term only makes sense when considering three-dimensional phenomena, and is responsible for making the flow become more and more complex. A 2D flow will never really become turbulent, simply because it only has a one-dimensional vorticity component. It is thus said that a 2D flow only diffuses and convects.

The Vortex Particle method

Eqs. (1.1) and (1.3) constitute the velocity-vorticity form of the Navier-Stokes equations for a 3D incompressible flow. Those are the ones discretised and solved in the `VPM`.
Based on the vorticity obtained by the discretisation of Eq. (1.2) and using the incompressibility, the velocity is obtained by solving the Poisson equation (Eq. (1.5)).

$$\nabla^2 \mathbf{u} = -\nabla \times \boldsymbol{\omega} \tag{1.5}$$

The vortex particle method assigns to every particle:

- a position $\mathbf{x}_p$
- a volume V_p
- a strength $\alpha_p = \int_{V_p} \omega \, d\mathbf{x} \approx \omega_p \, V_p$

The Lagrangian part of the method is thus represented by the fact that the strength value is drawn by the particles, convected with the flow, and thus solved from Eq. (1.6) and Eq. (1.7):

$$\frac{d\mathbf{x}_p}{dt} = \mathbf{u}_p \tag{1.6}$$

$$\frac{d\alpha_p}{dt} = \int_{V_p} \left((\boldsymbol{\omega} \cdot \nabla)\, \mathbf{u} + \nu \nabla^2 \boldsymbol{\omega} \right) \, d\mathbf{x} \tag{1.7}$$

However, the right hand side (RHS) of Eq. (1.7) (diffusive and stretching terms) is solved on the mesh, making the method hybrid, thus not completely Lagrangian.

The VPM method

In order to compute the latter RHS, as well as to solve the Poisson equation (using FFT), an interpolation of the particles vorticity field is performed towards the mesh (*Particle To Mesh*, P2M). This is achieved through a high order scheme, transferring the information carried by the particles onto the mesh, at each time step, using the M_4' formula of Monaghan. For the vorticity, it reads

$$\boldsymbol{\omega}(\mathbf{x}_q) = \sum_p \frac{\alpha_p}{h^3} M_4' \left(\frac{\mathbf{x}_q - \mathbf{x}_p}{h} \right) \tag{1.8}$$

Where the subscript q refers to a mesh quantity, whereas p refers to a particle quantity.

Once the computations of the stretching and the diffusion terms as well as the solvation of the Poisson equation performed on the mesh, the interpolation of both the vorticity and the velocity

is done back on the particles (*Mesh To Particle*, M2P) in order to perform the time-integration, using the third order low storage Runge-Kutta scheme.

Furthermore, the mesh is used in order to perform **remeshing** and **reprojection** operations. Indeed, one drawback of a completely Lagrangian method is the fact that the particles may not be distributed uniformly enough, inducing a high distorsion. That way, their position is reinitialised each n_{remesh} time steps, while their vorticity value is stored on the mesh.
In addition to that, reprojections are needed each n_{reproj} time steps in order to ensure a divergence-free vorticity field. This is required as the discretisation of the 3D vorticity field does not imply $\nabla \cdot \boldsymbol{\omega} = 0$. The reprojection step is an explicit enforcement of it.
With those considerations, the general VPM scheme may be presented (in a simple way) as in Fig. 1.1.

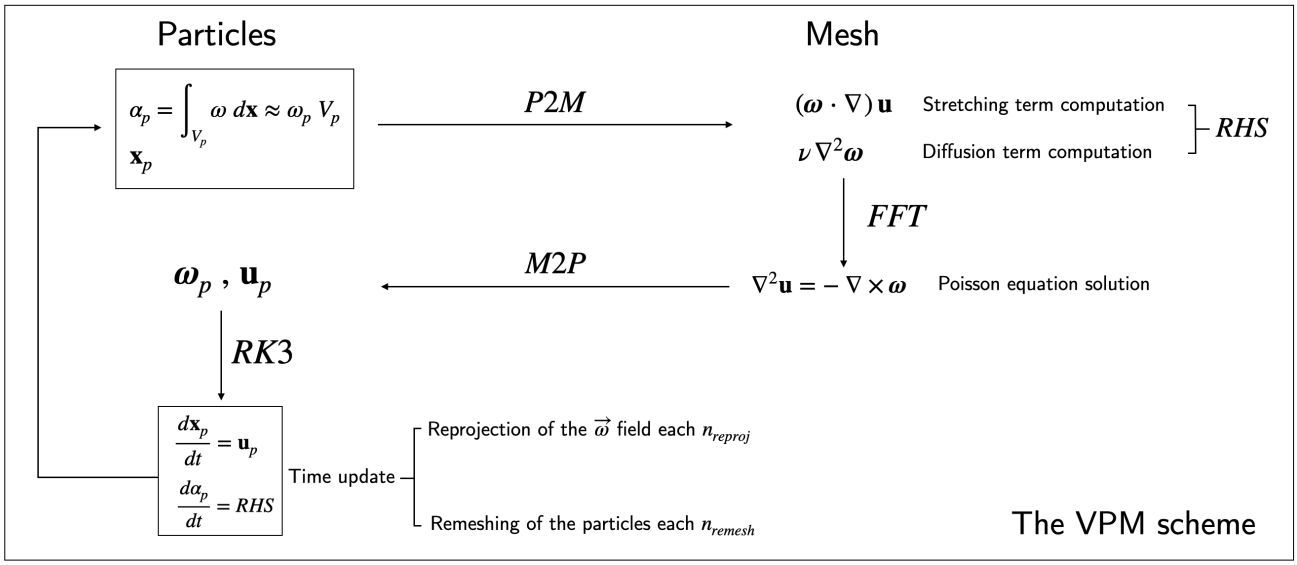

Figure 1.1: Schematic representation of the VPM method

1.2 The vortex ring setup

A **vortex line** is defined as a line being everywhere tangent to the local vorticity vector. A **vortex tube** is defined as a tube formed by a set of vortex lines intersecting its cross section S. That way, a **vortex ring** may be defined as being a vortex tube whose vortex centerline is a circle.

The vortex rings studied in the present work are defined by the strength assigned to the particles composing it. This local strength may be distributed following a Gaussian distribution according to the distance from the vortex centerline. Hence, by doing so, the support of vorticity would expand on the whole computational domain (basically, up to the infinity). This is the reason why, and as was done for several previous master's thesis led at the TFL pole of UCLouvain, a compact Gaussian distribution is considered. The latter is defined based on geometrical quantities. Those

geometrical characteristics are presented in Fig. 1.2.

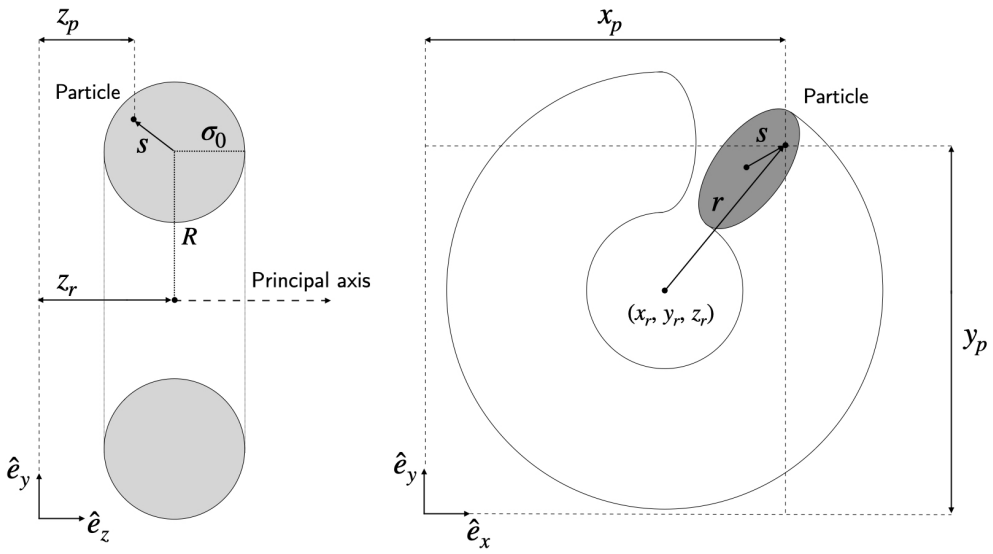

Figure 1.2: Description of the geometrical quantities characterising the vortex ring

Taking, for this case, $\hat{\mathbf{e}}_z$ as being the principal axis of the ring, the following parameters are defined:

$$r = \sqrt{(x_p - x_r)^2 \ + \ (y_p - y_r)^2} \qquad z = z_p \ - \ z_r \qquad s = \sqrt{z^2 + (r - R)^2}$$

$$\rho_1 = \frac{s}{\sigma} \qquad \rho_2 = \frac{s}{\sigma_0} \qquad \beta = \frac{\sigma}{\sigma_0} \qquad \longrightarrow \qquad \rho_2 = \beta\rho_1$$

Where s is the position of the particle with respect to the centerline, σ is the compactness of the Gaussian distribution and σ_0 is the radius of the vorticity support. β thus determines the compact aspect of the vortex ring.

Also, the circulation of a ring is defined, with S depicting the cross section of the circular vortex tube.

$$\Gamma = \int_S \omega \ dS \tag{1.9}$$

Then, the compact Gaussian profile may be defined, according to s, the distance of a point from the vortex centerline of the ring. The latter distribution is made dimensionless thanks to σ and Γ. Knowing that the initial vorticity only has an azimutal component:

$$\frac{\omega_\theta(s)\pi\sigma^2}{\Gamma} = \begin{cases} C(\beta^2) \ \exp\left(-\frac{\rho_1^2}{(1-\rho_2^2)}\right) & \text{for } \rho_2 < 1 \\ 0 & \text{elsewhere} \end{cases}$$

The following identity has then to be ensured:

$$\int_0^{2\pi} \int_0^{\sigma_0} \omega_\theta \; s \; ds \; d\theta = \Gamma$$

For which the constant $C(\beta^2)$ is derived:

$$\frac{C(\beta^2)}{\pi\sigma^2} \; 2\pi \; \int_0^{\sigma_0} \exp\left(-\frac{(s/\sigma)^2}{(1-\beta^2(s/\sigma)^2)}\right) \; s \; ds = 1 \qquad \text{thus} \qquad C(\beta^2) = \frac{\sigma^2 \; \beta^2}{2 \; \sigma^2 \; \underbrace{\int_0^1 \exp\left(-\frac{\rho_1^2}{\left(1-\beta^2\rho_1^2\right)}\right) \; \rho_1 \; d\rho_1}_{\mathcal{S}}}$$

Where the choice has been made to work with $\beta = 1$.

$$\mathcal{S} = \int_0^1 \exp\left(-\frac{\rho_1^2}{(1-\beta^2\rho_1^2)}\right) \; \rho_1 \; d\rho_1$$

$\mathcal{S}$ has been computed numerically using the `trapz` function of `Matlab`, so that

$$C(\beta^2) = \frac{\beta^2}{2 \; \mathcal{S}} = \frac{1}{0.4036} = 2.4774 \tag{1.10}$$

Based on that, the vorticity profile along the s coordinate is established, and presented in Fig. 1.3.

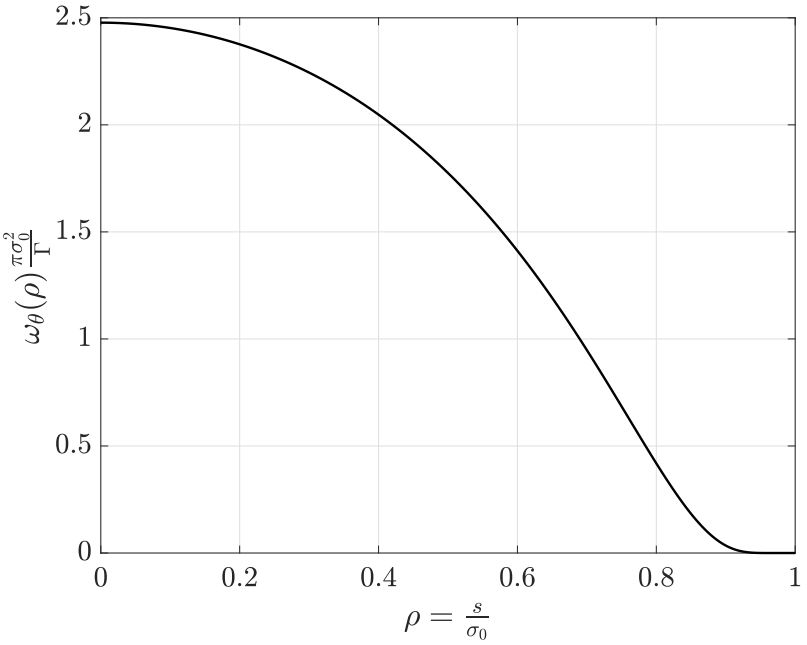

Figure 1.3: Vorticity distribution in the vortex ring cross section

1.3 Helicity content in vortex rings

Helicity is a physical quantity which has raised concern since more than a century when referring to the knot theory. Considering a contour C, helicity characterises the degree at which that line winds on itself, at which frequency and at which intensity, before finally closing the contour. In 1858, Helmholtz [7] derived the first mathematical characterisations of helicity for a velocity field. Since then, that quantity went on being at the center of interest for purely mathematical descriptions of lines and knots. The categorisation of the latter quantity between several storage modes and the eventual transfer between them has been achieved on purely topological basis by Călugăreanu [2] in 1961, and further discussed by Moffatt and Ricca [8] in 1992. Moffatt also put the accent on the helicity for proper tangled vortex lines [1], by studying their "degree of knottedness" in 1969, as well as the helicity in turbulent flows [9] in 1992.

The question of the content and evolution of the helicity in vortex ring configurations has already been tackled by Scheeler and van Rees [4] [5], thanks to hydrodynamically generated vortex ring structures. By laser measurements, they quantified the entanglement of their experimentally generated fields and evoked assumptions on the potential transfer of helicity from one mode to another. The general question they tried to answer was whether or not helicity could be considered as being a conserved quantity for a field under the action of viscosity.

This master's thesis has the aim to numerically investigate the behaviour of helicity containing configurations. That way, it hopes to characterise the way this content transfers from potential storage modes to others, to what extent it is likely to be conserved and by which mechanisms.

1.3.1 Helicity - Definitions

Helicity may be described as the degree at which vortex lines of a flow are interwined. Its general mathematical expression is given by

$$H = \int_V \overrightarrow{u} \cdot \overrightarrow{\omega} \, dV \tag{1.11}$$

i.e. the integral over the considered domain of the dot product between the local velocity and vorticity vectors. As a first approach, helicity may be considered as fed by 3 contributions:

$$H = \int_V \overrightarrow{u} \cdot \overrightarrow{\omega} \, dV = Linking \; + \; Writhing \; + \; Twisting \tag{1.12}$$

Those three storage modes of helicity content represent the configurations a vortex line may adopt in order to create helicity. Those are graphically represented in Fig. 1.4.

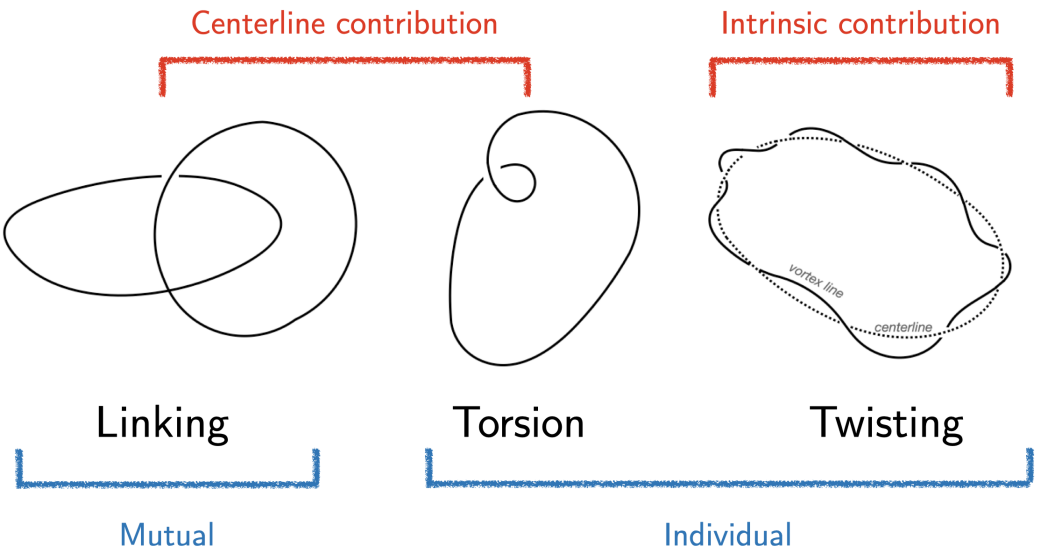

Figure 1.4: Schematic representation of the different modes of helicity storage

The modes may be classified as follows: linking is the only contribution involving the influence of one ring on the other whereas writhing and twisting contributions are only determined by rings considered on their own. That way, it is possible to extend the formulation as

$$H_{link} = \int_V \overrightarrow{u_1} \cdot \overrightarrow{\omega_2}\, dV + \int_V \overrightarrow{u_2} \cdot \overrightarrow{\omega_1}\, dV \tag{1.13}$$

And

$$H_{writhe\,+\,twist} = \int_V \overrightarrow{u_1} \cdot \overrightarrow{\omega_1}\, dV + \int_V \overrightarrow{u_2} \cdot \overrightarrow{\omega_2}\, dV \tag{1.14}$$

Where the subscript i refers to a quantity relative to $ring_i$.
Also, the difference has to be made between *centerline helicity contribution* and the rest, i.e. *intrinsic contribution* or *bundle contribution*, when considering a vortex tube as an assembly of vortex lines. Centerline helicity refers to an helicity contribution that may only be characterised by looking at the central vortex line of the ring: so are called the writhing and linking contributions. In other words, the helicity content of a purely writhed ring, deprived from twisting, may be completely described by concentrating the circulation of the entire tube onto the vortex centerline.

However, twisting can not be defined as so: the consideration of the entire bundle of vortex lines is necessary to characterise it. This is the reason why twisting is often referred as being the intrinsic contribution to helicity: it is there the addition of the contribution of each vortex line of the tube that contributes to the global twist. That way, Fig. 1.4 depicts both characteristics differentiating the three helicity contributions: the duality *individual/mutual* and the duality *intrinsic/centerline contribution*. More advanced mathematical descriptions of the helicity are described in Chapter 6, related to the knot theory, and adopting a purely topological point of view.

First, the already derived Navier-Stokes equation in vorticity-velocity formulation is recalled:

$$\frac{D\,\boldsymbol{\omega}}{D\,t} = (\boldsymbol{\omega} \cdot \nabla)\,\mathbf{u} \;+\; \nu \nabla^2 \boldsymbol{\omega} \tag{1.15}$$

Where the material derivative of the vorticity is seen to be the result of a **stretching** term and a **diffusion** term.

From Eq. (1.15), it may be concluded that, in a inviscid ($\nu = 0$) configuration, a vortex line will behave like a material line (2^{nd} theorem of Helmholtz). That way, vortex lines will not be able to cross each others and "destroy information": in a inviscid flow, it is known that helicity is a conserved quantity. However, it is still not clear about the evolution and potential conservation of helicity when considering viscous flows. In addition to its evolution, the transfer of it from scales to scales and from components to others is also raising concern. The present master's thesis aims thus at the initialisation and study of various configurations with the hope to characterise those transfer, conservations and dynamic evolutions.

1.3.2 Intrinsic quantities - Definitions

The developments performed in order to obtain Eq. (1.15) may lead to the definition of a particular physical quantity: enstrophy. By dot-producting Eq. (1.15) by ω, and re-arranging it, one obtains

$$\frac{D}{Dt}\left(\frac{\omega_i\,\omega_i}{2}\right) = \omega_i\,d_{ij}\,\omega_j + \nu\frac{\partial}{\partial x_j}\frac{\partial}{\partial x_j}\left(\frac{\omega_i\,\omega_i}{2}\right) - \nu\frac{\partial\omega_i}{\partial x_j}\frac{\partial\omega_i}{\partial x_j} \tag{1.16}$$

Enabling the definition of local enstrophy:

$$\mathcal{E} = \frac{\overrightarrow{\omega}\cdot\overrightarrow{\omega}}{2} \tag{1.17}$$

Integrating Eq. (1.16) over the volume of computation yields

$$\frac{D}{Dt}\overline{\mathcal{E}} = \overline{\omega_i\,d_{ij}\,\omega_j} - \nu\frac{\partial\omega_i}{\partial x_j}\frac{\partial\omega_i}{\partial x_j} \tag{1.18}$$

With

$$\mathcal{E} = \frac{1}{V}\int_V \frac{\omega_i\,\omega_i}{2}dV = \frac{\overline{\omega\cdot\omega}}{2} = \left\langle\frac{\omega\cdot\omega}{2}\right\rangle \tag{1.19}$$

Eq. (1.18) is seen as being composed of a **source term** and a **sink term**, the latter always making the enstrophy go down. As enstrophy is a direct indicator of the complexity of a flow, viscosity is seen as "making the flow become less complex". It may also be observed that the source term is basically a three-dimensional phenomenon.
The link between enstrophy and energy dissipation is now possible (developments are omitted):

$$\overline{\epsilon} = 2\nu\overline{\mathcal{E}} \tag{1.20}$$

It is then considered that, when using numerical simulations, the total dissipation of the turbulent kinetic energy (TKE) is the result of both the enstrophy contribution and a numerical dissipation

$$\overline{\epsilon}_{tot} = \overline{\epsilon}_{kolmo} + \overline{\epsilon}_{SGS} \tag{1.21}$$

where the subscript *kolmo* refers to the dissipation performed by the Kolmogorov scales and *SGS*

to the one relative to the subgrid-scale modeling.

Next, the mesh Reynolds is defined:

$$Re_{h,\omega} = \frac{|\omega|\, h^2}{\nu} \tag{1.22}$$

as well as the Kolmogorov scale

$$\eta = \left(\frac{\nu^3}{\epsilon}\right)^{1/4} \tag{1.23}$$

Thus, the expression of η (being a local quantity) based on $Re_{h,\omega}$ is derived:

$$\epsilon = 2\nu\frac{\omega\cdot\omega}{2} \qquad \longrightarrow \qquad \eta^2 = \frac{\nu}{(\omega\cdot\omega)^{1/2}} \tag{1.24}$$

$$\text{With} \qquad Re_\omega = \frac{(\omega\cdot\omega)^{1/2}\, h^2}{\nu} \tag{1.25}$$

$$\text{Yielding} \qquad \frac{\eta^2}{h^2} = \frac{1}{Re_\omega} \qquad \text{thus} \qquad \boxed{\frac{\eta}{h} = \frac{1}{\sqrt{Re_\omega}}} \tag{1.26}$$

Where η has been divided by the grid size in order to study dimensionless scales, and being able to compare values with the criterion for DNS-resolution in spectral codes, $h \leq 2\eta$.

The following chapters tackle the research question of this master's thesis itself, and will be organised following the three modes of helicity storage introduced in the present section, Section 1.3.1. That way, studies over linking, writhing and twisting are led and presented, followed by a chapter dedicated to the gathering of drawn conclusions, in order to fully characterise the evolution of the helicity content in vortex ring configurations.

Chapter 2

The linking content

In terms of helicity, as defined previously, linking represents the only way a curve with a strength may confer helicity to a system by acting on another curve. The present chapter aims at the study of the evolution of that latter content through the analysis of two vortex ring configurations. It is desired that in both configurations presented here, the whole initial helicity content is entirely due to the linking.

The investigation of the linking storage mode has first been performed through the study of the dynamics of two vortex rings in a knot-type configuration, with the same circulation and at $Re_\Gamma = 2000$. Then, the case of the evolution of that same knotted arrangement has been analysed, with both rings circulations being different, $\Gamma_1 \neq \Gamma_2$, and $Re_{\Gamma_1} = 2000$.

2.1 The knot-type configuration

2.1.1 Configuration initiation

The initialisation of a single vortex ring has been developed in Chapter 1.2, as well as the vorticity distribution across the section of the vortex tube. The present analysis aims at the study of two vortex rings of same circulation such that the initial helicity content is only due to the action of the fields of $ring_1$ on the fields of $ring_2$, and vice-versa. Indeed, each of both rings is qualified as *planar*: their respective vortex centerlines (i.e. the vortex line joining the center-point of each cross section of the ring) are confined in a plane. This means that no centerline helicity is initiated. Besides, those planes are perpendicular. As the vorticity field of each of both rings is initially purely azimutal, and for a ring with principal axis $\overrightarrow{x}_i$, at $\tau = 0$, $\omega_i = 0$ for the whole ring. It is thus directly concluded that, for each ring

$$H_i = \int_V \overrightarrow{u_i} \cdot \overrightarrow{\omega_i} \, dV = 0$$

And thus that the helicity content of the system comes from, for $i \neq j$

$$H = \int_V \overrightarrow{u_i} \cdot \overrightarrow{\omega_j} \, dV + \int_V \overrightarrow{u_j} \cdot \overrightarrow{\omega_i} \, dV$$

The simulation presented in this section has been performed on a fully periodic domain of size $[L \times L \times L] = [-4R\,;\,4R] \times [-4R\,;\,4R] \times [-4R\,;\,4R]$, with a grid-resolution of 513^3 nodes, and with R being the radius of the ring. Table 2.1 summarises the main parameters characterising the knot configuration studied here.

Table 2.1: Main parameters of the knot-type configuration

	$ring_1$	$ring_2$
Circulation	$Re_{\Gamma_1} = 2000$	$Re_{\Gamma_2} = 2000$
Principal axis	[0 0 1]	[0 1 0]
Ring center	$\overrightarrow{O_1} = [0\ 0\ 0]$	$\overrightarrow{O_2} = \overrightarrow{O_1} + [R\ 0\ 0]$
R	L/8	L/8
σ_0	R/4	R/4

2.1.2 Study of the dynamics

The present configuration is characterised by a Reynolds number based on the circulation

$$Re_\Gamma = \frac{\Gamma}{\nu} = 2000$$

The interaction between both rings is described in Fig. 2.1, for

$$0 \leq \tau \leq 5 \qquad \text{with } \tau \text{ defined as} \qquad \tau = \frac{t\,\Gamma}{R^2} \tag{2.1}$$

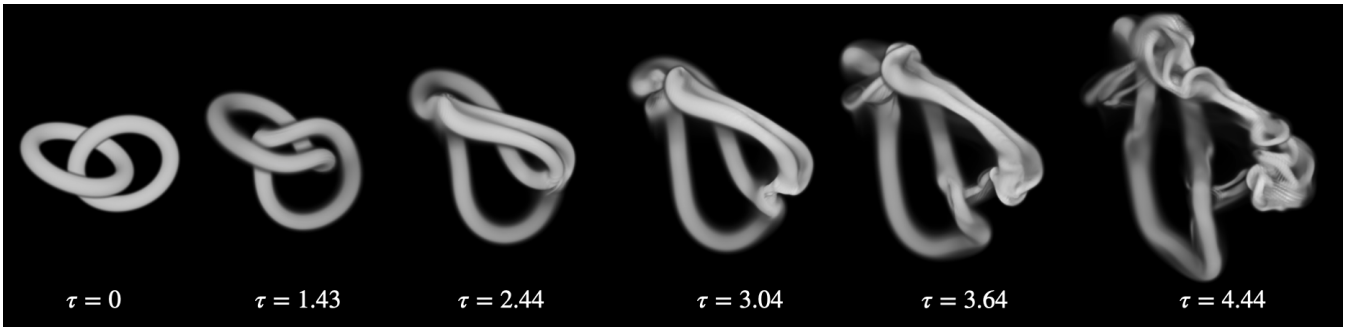

Figure 2.1: Time evolution of the knotted configuration for $0 \leq \tau \leq 5$

In order to be able to observe iso-vorticity surfaces of both rings at once, a cut has been performed in the plane with its normal direction being $[0,\ 1,\ 1]$, as described in Fig. 2.2.

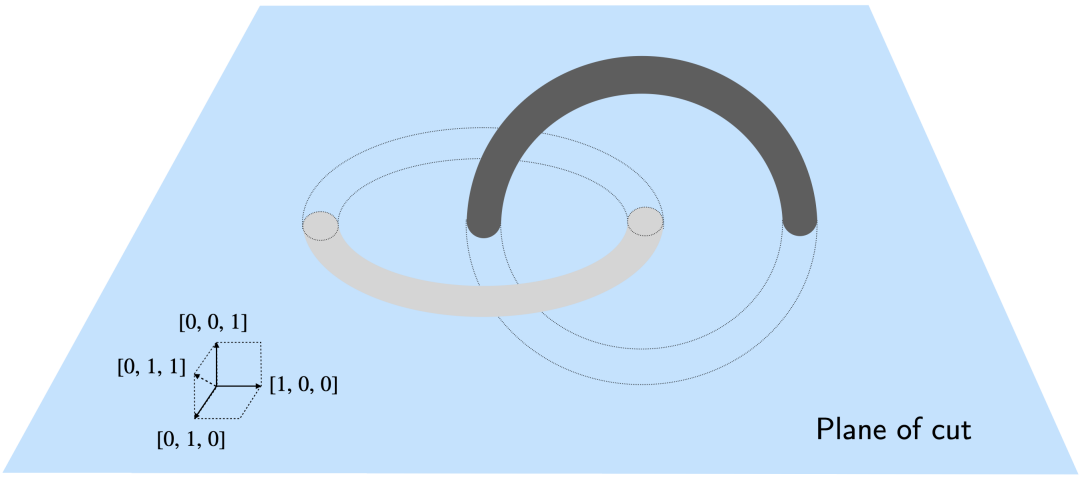

Figure 2.2: Description of the plane of cut for the iso-vorticity surfaces

The evolution of the vorticity iso-surfaces in that latter plane is described in Fig. 2.3, for $0 \leq \tau \leq 4$. This time window is first studied as being the one in which most interactions occur between both rings. It is observed that, after entering contact and creating highly turbulent structures, the initially knotted rings operate a reconnection, resulting in the formation of a larger ring and an auxiliary structure. That complex interaction is also depicted by the evolution of the enstrophy, in Fig. 2.9a, which is defined in Section 2.1.2.

Figure 2.3: Evolution of the iso-vorticity surfaces with normal [0, 1, 1]

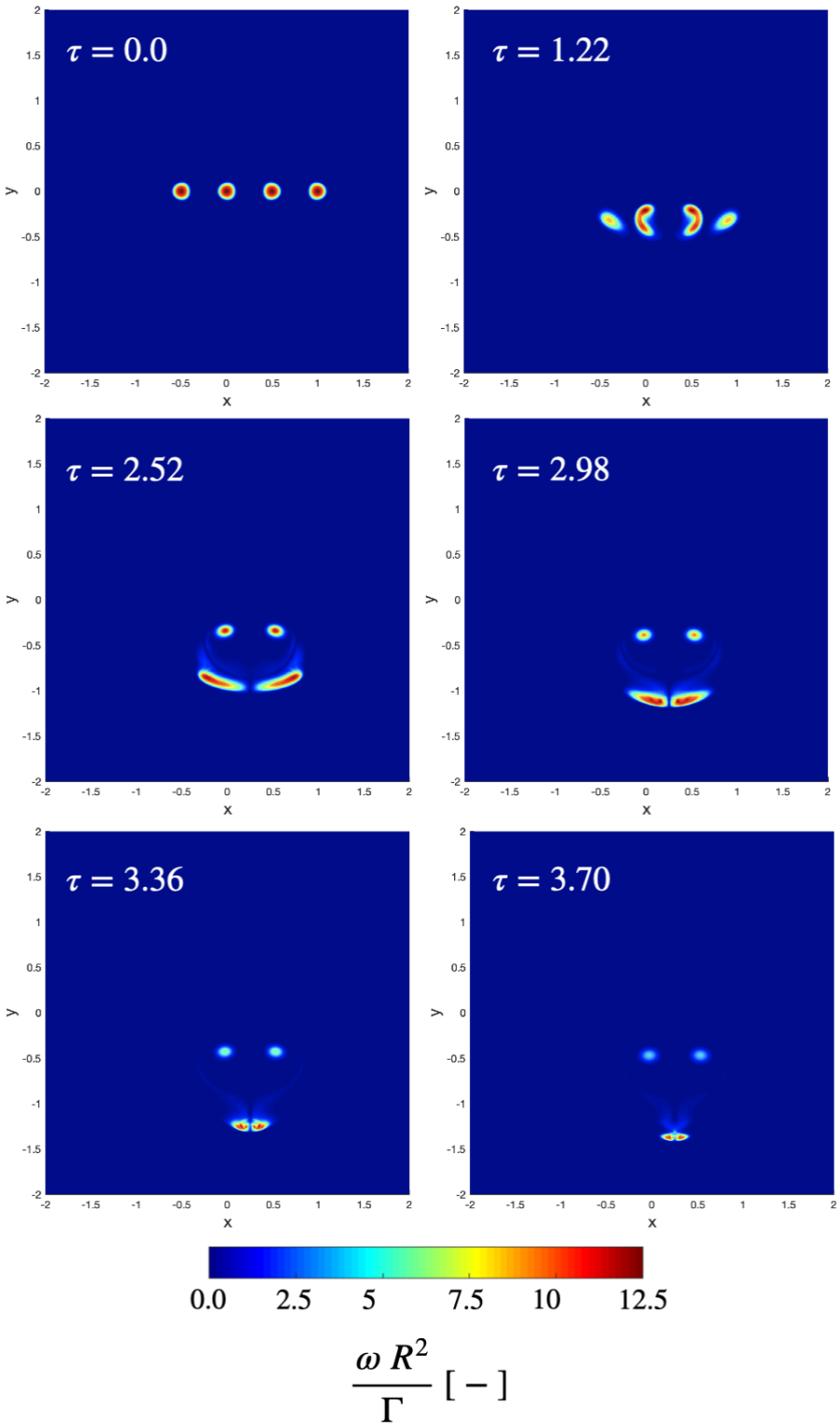

The evolution of the 3D renderings of the vorticity field is presented in Fig. 2.4, until the reconnection of both rings. Vorticity threads of high circulation make the junction between both separating structures until they eventually disconnect. Further details of the zones of interaction are provided in Appendix C, with adaptative cuts.

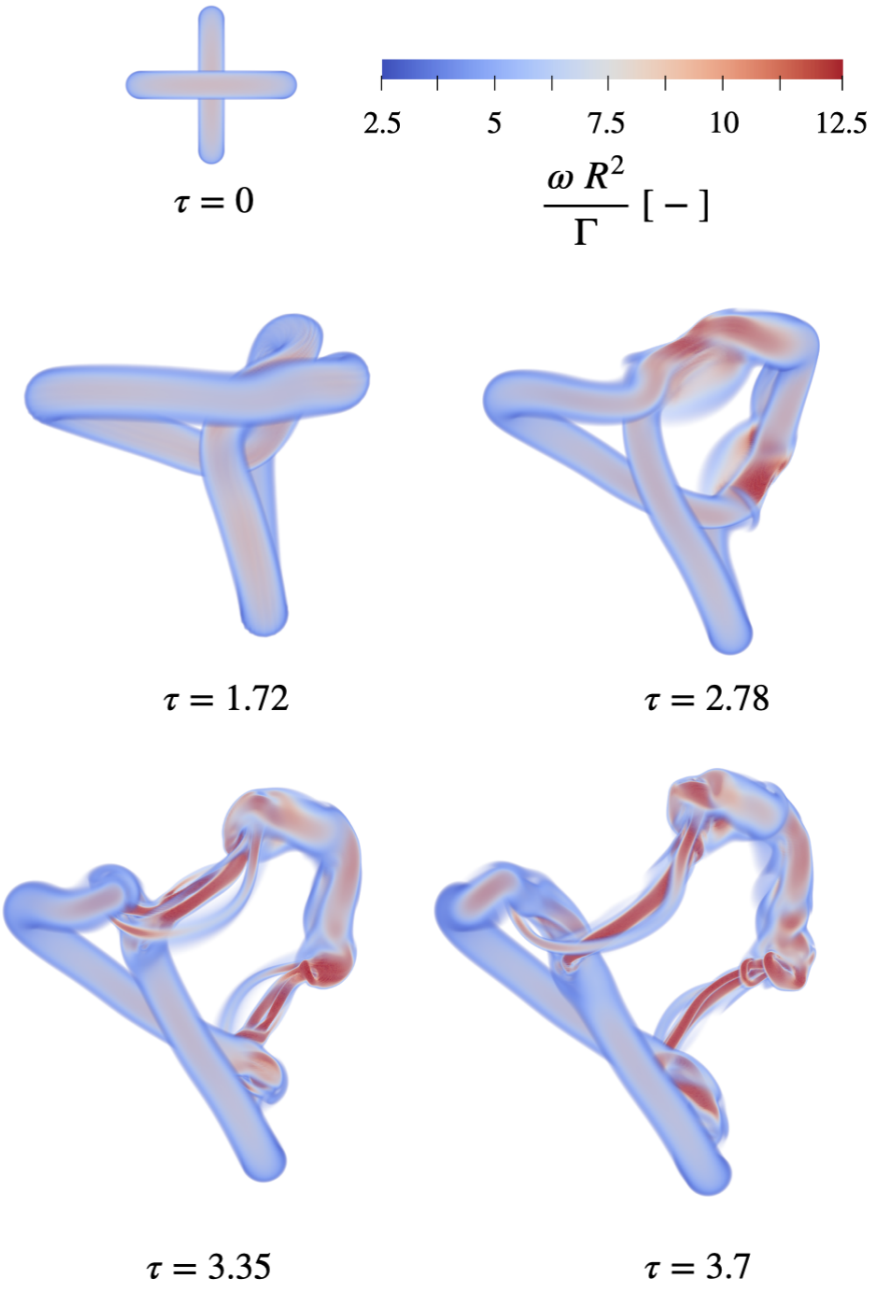

Figure 2.4: Evolution of the interaction between both rings involved in the knot-type configuration thanks to volume rendering of the vorticity

Helicity study

The helicity evolution of the knot configuration is presented in Fig. 2.6, for $0 \leq \tau \leq 5$.

It is first verified that the initial helicity content is indeed completely due to linking. For two linked lines of circulations Γ_1 and Γ_2, helicity is given by [7]

$$H_{link} = 2n\ \Gamma_1\Gamma_2 \tag{2.2}$$

With n being the *Gauss linking number*, here $= -1$. Its value depends on whether the configuration is right-handed or left-handed, as shown in Fig. 2.5.

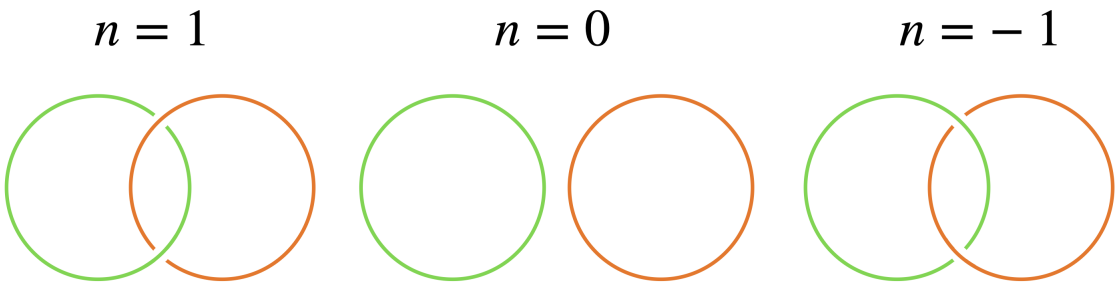

Figure 2.5: Right and left handed knotted configurations

This should lead to an initial helicity content $H/(\Gamma_1\Gamma_2) = -2$, which is the case, as seen in Fig. 2.6.

A first tendency of helicity dissipation is observed for $0 \leq \tau \leq 2$, until the interaction between both rings occurs. Then, from $\tau \sim 2.5$ to $\tau \sim 3.7$, an helicity content is created by the entering into contact of both vortex tubes. After that complex interaction, helicity tends to dissipate again, at a more important rate. That faster dissipation directly follows the time when enstrophy has reached its maximal value, as observed in Fig. 2.9a.

Nonetheless, this picture alone does not provide many insights of the mechanisms responsible for the creation/destruction of the helicity and of the potential transfer from one mode to another.

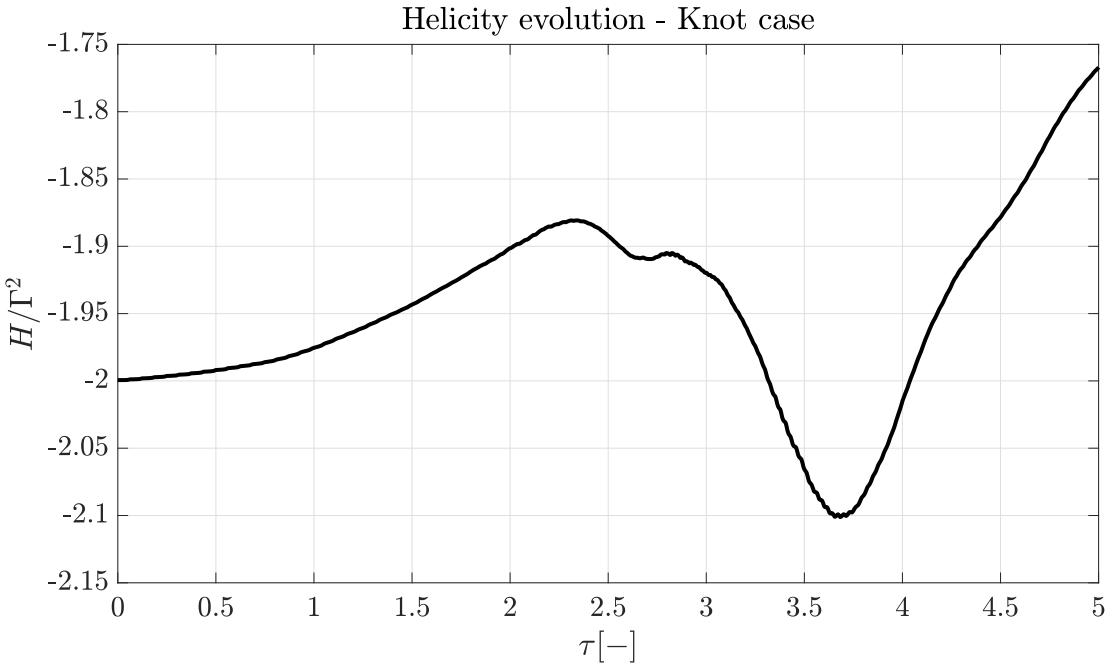

Figure 2.6: Helicity evolution of the knot-type configuration

This interaction is to be put in relation with the evolution of several dynamic quantities, detailed below, in Section 2.1.2.

In order to study the eventual transfer of helicity from one mode to another, a mask function has been implemented in `VPM` and applied on the vorticity field. The latter tool eventually provides the isolation of both $\overrightarrow{\omega}_1$ and $\overrightarrow{\omega}_2$ fields. Based on them, $\overrightarrow{u}_1$ and $\overrightarrow{u}_2$ have been extracted using the Biot-Savart law applied on the isolated vorticity fields. The complete description of this methodology is presented in Appendix A. This has thus allowed the separation between the mutual and the individual helicity components, whose evolutions are depicted in Fig. 2.7:

The term *total helicity* has been obtained as $H = \int_V \overrightarrow{u} \cdot \overrightarrow{\omega}\ dV$.

The term *linking* has been obtained as $H_{link} = \int_V \overrightarrow{u}_1 \cdot \overrightarrow{\omega}_2\ dV + \int_V \overrightarrow{u}_2 \cdot \overrightarrow{\omega}_1\ dV$.

The term *writhing + twisting* has been obtained as $H_{remain} = \int_V \overrightarrow{u}_1 \cdot \overrightarrow{\omega}_1\ dV + \int_V \overrightarrow{u}_2 \cdot \overrightarrow{\omega}_2\ dV$,

It is to be mentioned that all 3 components have been computed separately. The summation *linking + writhing + twisting* yields quite precisely the same curve as *total helicity* (as shown by the red solid line), within a maximal relative error of $< 1\%$. This proves the right implementation of the mask as well as the complete capture of the total helicity content inside those 3 modes.

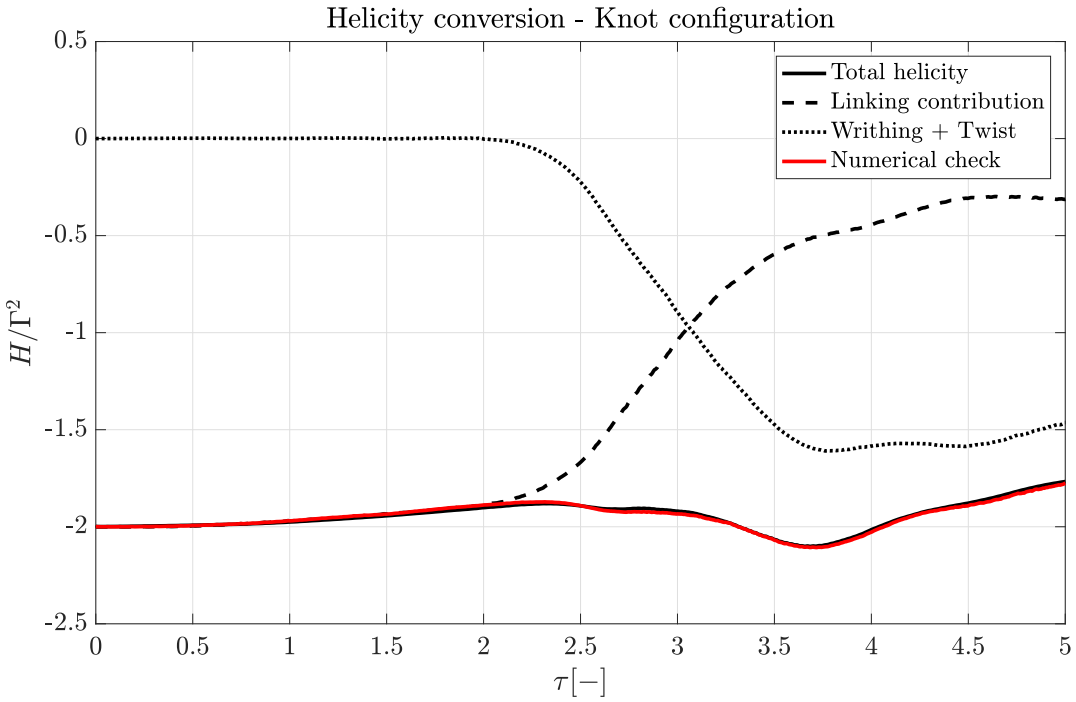

Figure 2.7: Evolution of the separated helicity contributions for the knot-type configuration

Based on Fig. 2.7, it is identified that the system seems to tend towards the storage of helicity into the writhing and the twisting modes, as dynamics become more complex due to the interactions between both rings.
It is also once again verified that the initial content is only due to interaction between the velocity field of $ring_1$ and the vorticity field of $ring_2$ and vice versa, as none of the writhing and the twisting modes have values initially. From $\tau = 2$, the linking content drastically dissipates: this occurs as soon as both rings start to interact, i.e. when both vortex tubes enter contact. At the same time, the writhing and twisting components take values: a redistribution from the linking mode towards the remaining modes operates.

This section has thus enabled to observe that, through the reconnection step, the initial linking mode tends to confer its content towards other, apparently more stable, helicity components. It is also stressed that, through that series of interactions, the total helicity content remains roughly conserved, demonstrating the efficiency of the mechanisms responsible for the redistribution.

Intrisic quantities characterisation

The present subsection presents the evolution of characterising quantities depicting the effects of the interactions between both rings on the properties of the flow.
It is first verified that the configuration may be considered as being sufficiently resolved. The evolution of the mesh Reynolds based on the vorticity is shown in Fig. 2.8a. The maximal value of it is reached in the middle of the reconnection event and does not exceed $Re_{h,\omega} = 33$. This may be seen as satisfyingly resolved to trust the obtained conclusions.

Figure 2.8

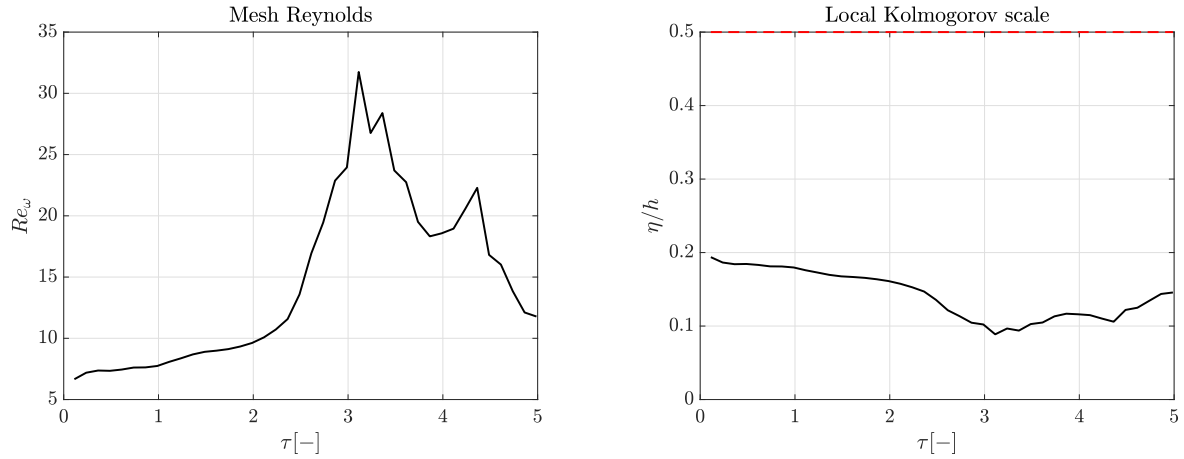

(a) Evolution of the mesh Reynolds $Re_{h,\omega}$ - Knot-type configuration

(b) Evolution of the Kolmogorov scale η/h - Knot-type configuration

Fig. 2.9b details the different contributions to the dissipation of the TKE, in a dimensionless way (thanks to the ring radius R and the circulation Γ): as was described in Section 1.3.2, in a perfectly resolved flow, it is entirely due to the enstrophy (whose evolution is shown in Fig. 2.9a, dimensionless as well). That way, the measured dissipation rate is compared to the physical contribution of it, $2\nu\ \mathcal{E}$, and the numerical dissipation is isolated. The latter is due to the subgrid-scale modeling and the reprojection steps.

Figure 2.9

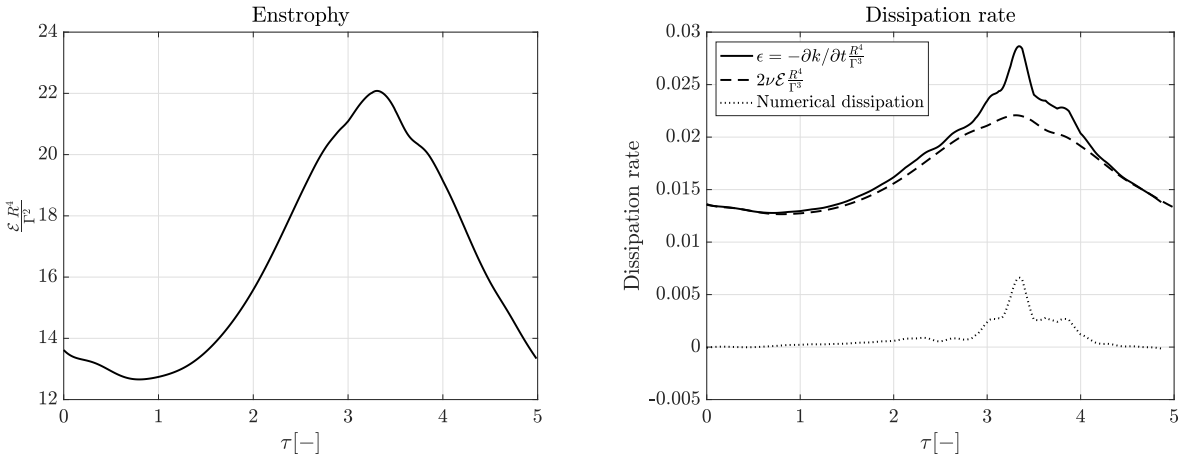

(a) Evolution of the enstrophy - Knot-type configuration

(b) Evolution of the dissipation rate contributions - Knot-type configuration

Finally, Fig. 2.8b depicts the evolution of the local Kolmogorov scale, as was derived in Eq. (1.24). As the configuration complexifies, those dissipative scales become smaller and smaller, making it

more and more complex for the grid to capture their dynamics. The criterion of fully resolved DNS for a spectral code is shown in red. It is observed that this criterion is never fulfilled in that case. However, and as already discussed before, the values of the mesh Reynolds are low enough to have a satisfyingly resolved flow.

2.2 Interaction of rings of different circulation

As was concluded in Section 2.1, the reconnection event, leading the initially knotted configuration to a final state composed of a large ring and an auxiliary one, was responsible for the transfer of helicity from the linking component to the other ones. The present section has the goal to further investigate that knotted structure, by trying to prevent both rings to reconnect.

2.2.1 Configuration

The geometrical implementation of this configuration is completely identical to the one described in Section 2.1. The only difference in the initial conditions (yet being determinant) is the fact that, with the subscript i referring to the $ring_i$

$$\Gamma_2 = 0.5\,\Gamma_1$$

Resulting in

$$Re_{\Gamma_1} = 2000 \qquad \text{and} \qquad Re_{\Gamma_2} = 1000$$

2.2.2 Helicity study

The fact that the circulation of both rings is not the same will induce the impossibility for the latters to reconnect. The evolution of the configuration is presented in Fig. 2.10, by volume rendering of the vorticity.

As expected, it is readily observed that both rings do not perform any transition from a tied to an untied structure. A complex interaction happens, with each ring rolling itself around the other one. The evolution of the helicity content of that configuration has been studied in the same way as was performed for the original knot configuration. Thus, the linking component, relative to the interaction between both rings, is separated from the remaining part of the total helicity content: writhing and twisting. Besides, the numerical summation of the isolated components (red line) obtained thanks to the implementation of the mask function is compared to the total content computed as $H_{tot} = \int_V \overrightarrow{u} \cdot \overrightarrow{\omega}\, dV$. This evolution is presented in Fig. 2.11.

It is first important to notice the limitations of the mask-function-method implemented in the context of this work. Indeed, as the topology of the configuration becomes highly complex for large times, the numerical summation of *linking* (dash) and *writhing + twisting* (dot), yielding the red curve, is not very close to the calculation of H_{tot} (solid, black). The structure of both rings may not be completely differentiated anymore after a certain time. However, the conclusions stated in Section 2.3 may be drawn.
It is observed that the linking completely diffuses, as almost no writhing content is created. This result is to be put in parallel with the one obtained for the case with $\Gamma_1 = \Gamma_2$ (Fig. 2.12).

Figure 2.10: Evolution of the vorticity volume rendering of the knot configuration for $\Gamma_2 = 0.5\,\Gamma_1$

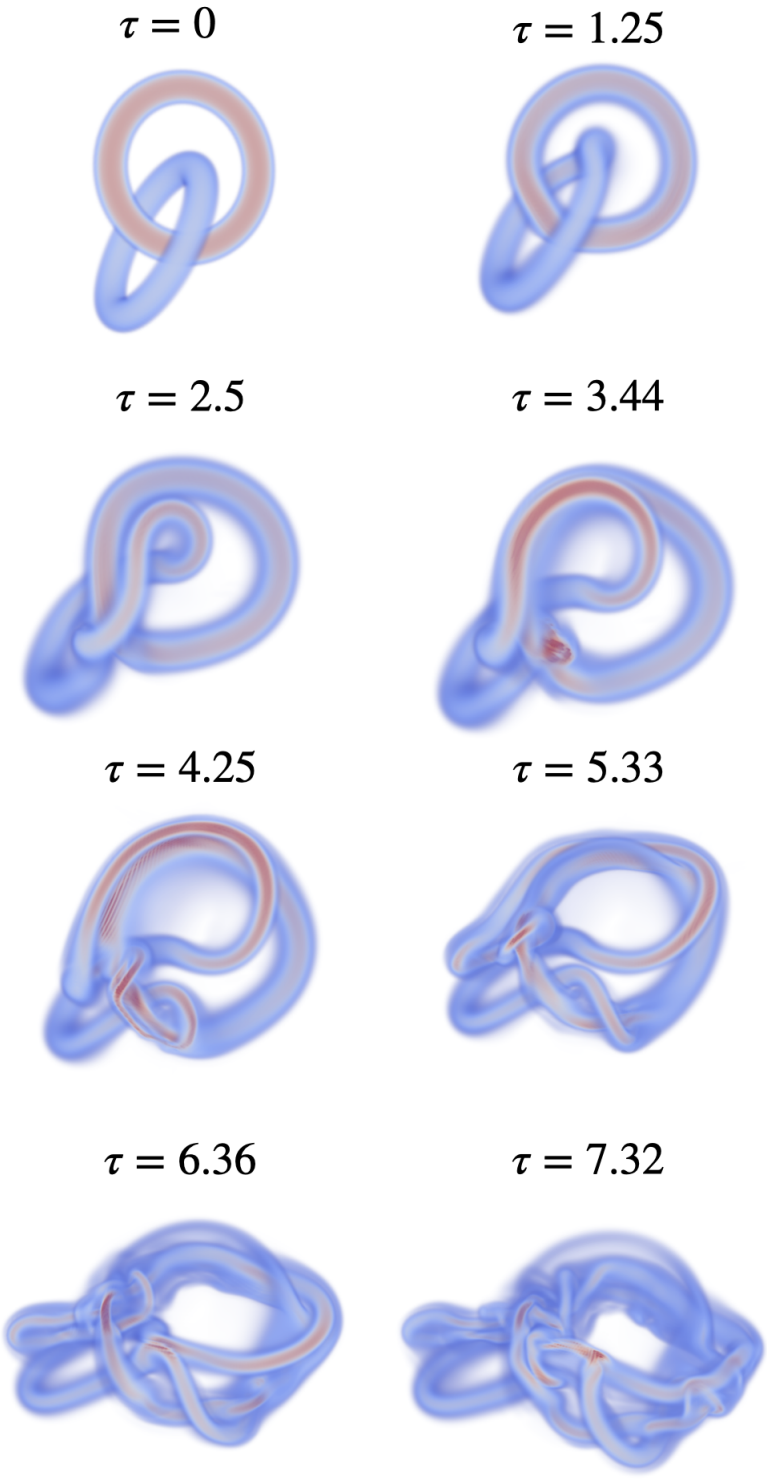

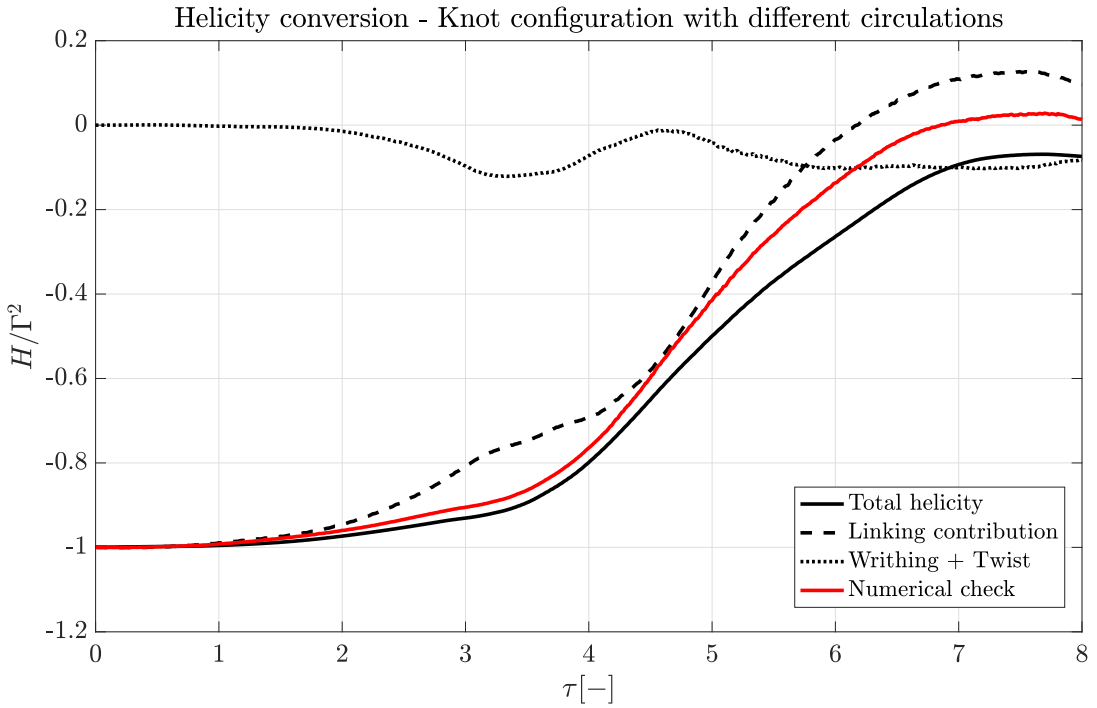

Figure 2.11: Evolution of the helicity content of the knot configuration with $\Gamma_2 = 0.5\,\Gamma_1$

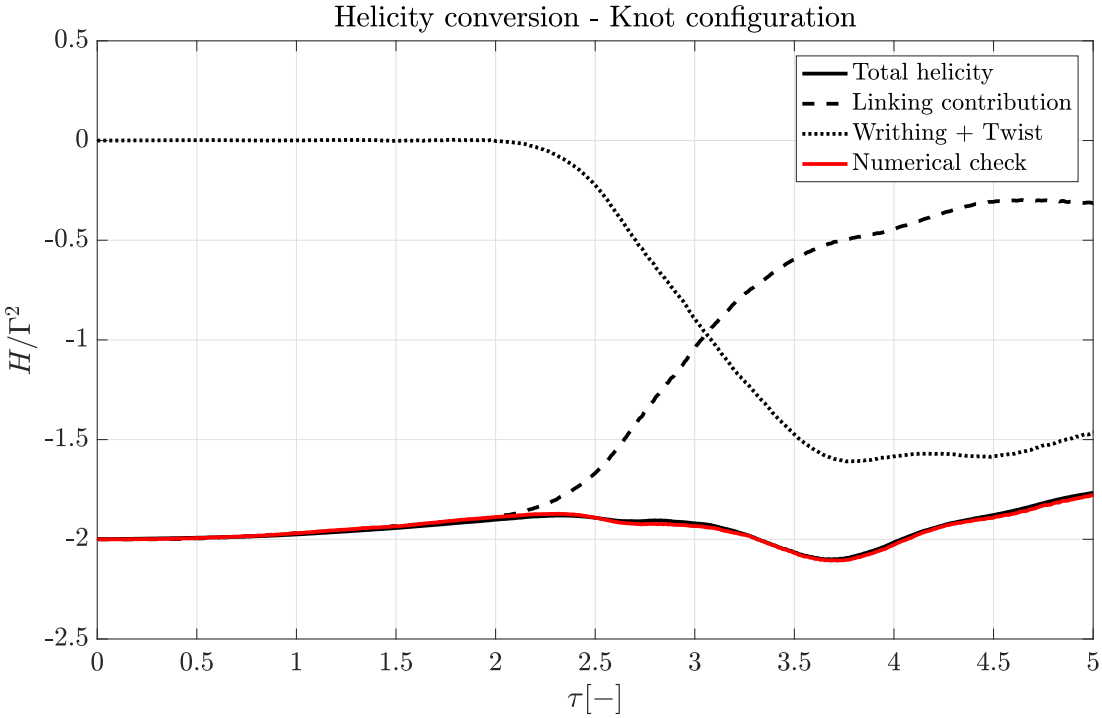

Figure 2.12: Evolution of the helicity content of the knot configuration with $\Gamma_2 = \Gamma_1$

2.3 Comparison of the cases with same and different circulations

For comparison purposes, the evolution of the helicity of the situation with similar circulations is reminded in Fig. 2.12.

It is observed that in the case where a reconnection process is made possible ($\Gamma_1 = \Gamma_2$), the initial linking mode is able to transfer most of its helicity content into another one, writhing and twisting. With regard to further studied configurations, about the transfer from twisting to writhing, it is concluded that, in the case of the knot evolution, the storage mode solicited to gather the helicity coming from **linking** is **writhing**.
Yet, when considering the impossibility for the rings to reconnect ($\Gamma_1 \neq \Gamma_2$), it is seen that no other helicity storage mode is activatable. As the rings stay, in some sort, in a knotted situation, the linking content has no loophole, and is inevitably brought to dissipate. Indeed, (almost) no writhing nor twisting are created.

The latter results enable to state that **linking does not constitue a stable storage mode for helicity content**, when put under the effect of viscosity.

Chapter 3

The writhing content

As was presented in Section 1.3.1, when considering vortex tubes, writhing constitutes, with linking, an helicity storage mode which may only be considered based on the centerline(s) of the ring(s). The present chapter aims at the characterisation of writhing, and of the eventual helicity flows coming from or towards that mode. The study of it is obviously not made possible when considering a vortex ring whose vortex centerline is planar. This chapter thus first presents the implementation and evolution of a writhing containing "vortex ring", as well as other closed vortex tubes, containing helicity. Finally, leapfrogging configurations are presented in order to identify the potential transfer from ring to ring, and mode to mode.

3.1 Writhing containing configuration

Scheeler and van Rees [5] performed experimental measurements of the dynamics of vortex rings generated with moving hydrofoils. By inducing a structure initially provided with writhing and twisting, they identified that **twisting naturally dissipates under the action of viscosity** as **writhing seems to be a stable storage of helicity**. Thereby, the following explorations have the goal to confirm or complete those assumptions.

3.1.1 Ring initiation

First, a simulation with a lonely ring has been performed, and its helicity evolution is presented in Fig. 3.1, for $0 \leq \tau \leq 10$.

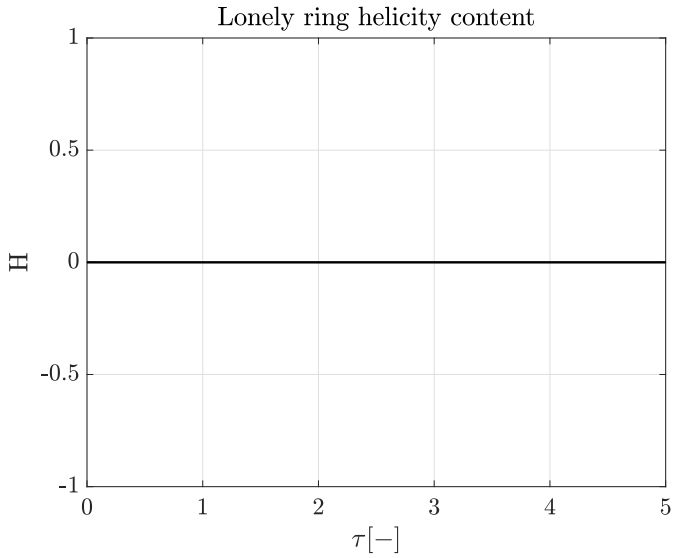

Figure 3.1: Lonely ring helicity evolution

The initial velocity field being at each location normal to the vorticity of the whole cross section of the tube, and in the absence of interaction able to create some helicity, the initial null content remains so for the whole evolution.

In order to induce writhe content in a lonely ring, and furthermore to study its evolution, an helicoidal structure is to be initiated. That structure may be identified to a circularly-closed corkscrew.

For simplicity reasons in the following developments, the principal axis of the writhing containing ring will be fixed as being $\hat{\mathbf{e}}_z$. Considering an initial ring of radius R and a centerline lying in the $z - plane$, geometrical modifications had to be implemented in order to obtain the geometry described in Fig. 3.2.

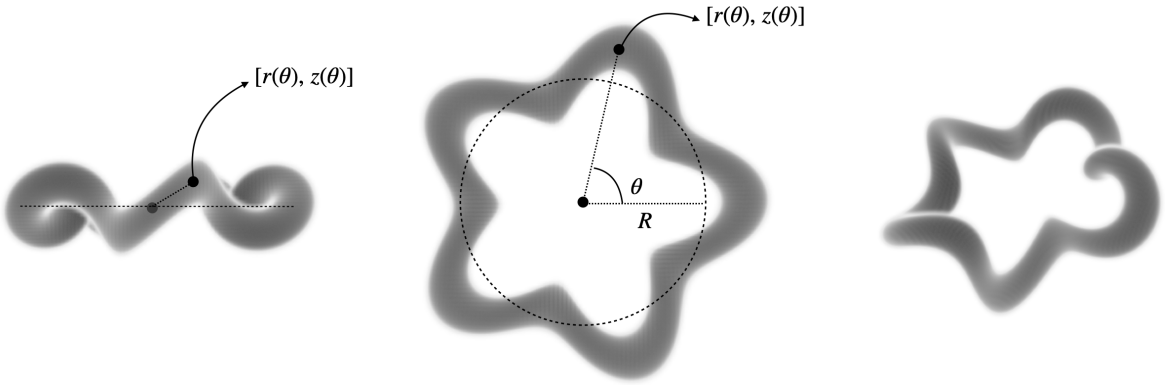

Figure 3.2: Initial geometry of the writhing containing ring with 5 cycles

A sinusoidal shape has been conferred in the z direction:

$$z(\theta) = \sigma_0 \cdot \sin(2\pi\ f\ R\ \theta) \tag{3.1}$$

With

$$f = \frac{1}{P} \qquad P = \frac{L}{n_{cycles}} \qquad L = 2\pi R \qquad n_{cycles} = 5$$

And $0 \leq \theta \leq 2\pi$ describes the angular position of the particle with respect to the center of the ring, so that the product $R\theta$ sweeps all the points along the "ring" and that the condition $\mathbf{x}_0 = \mathbf{x}_{2\pi}$ is satisfied (i.e. the tube closes on itself).

The same reasoning is applied in the radial direction, but ensuring that the sinusoïdal behaviour in that direction is in opposite phase with respect to the one in the z-direction:

$$r(\theta) = R + \sigma_0 \cdot \sin(2\pi\ f\ R\ \theta\ +\ \pi/2) \tag{3.2}$$

The term n_{cycles} is a geometrical parameter fixing the number of oscillations performed by the tube before its closure.

Each cross section of the writhed ring is circular, and the vorticity strength of a particle in it is determined in the same way as was done for the original vortex ring:

$$\omega_\theta(s) = \frac{\Gamma}{\pi\sigma^2} C(\beta^2) \exp\left(-\frac{(s/\sigma_0)^2}{\left(1-\beta^2\,(s/\sigma_0)^2\right)}\right)$$

Yet, while the vorticity did not have a z-component in the case of the vortex ring, it of course does along the writhed geometry. The determination of the x, y and z components of the $\vec{\omega}$ vector must therefore, for each particle, be tangent to the local vortex streamline direction (denoted by the triplets $[x, y, z]$) (see Fig. 3.3):

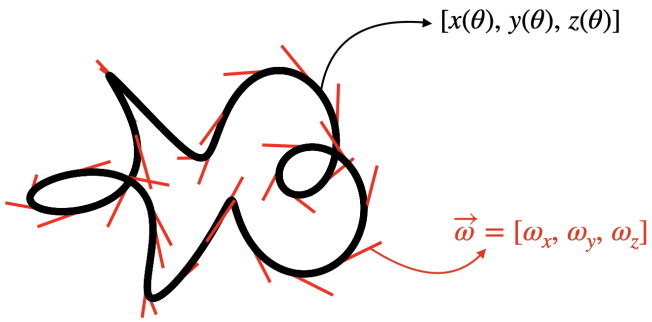

Figure 3.3: Tangent $\vec{\omega}$ vectors (red) along the writhed centerline geometry (black)

$$\omega_x(\theta) = \frac{dx(\theta)/d\theta}{\sqrt{(dx(\theta)/d\theta)^2 + (dy(\theta)/d\theta)^2 + (dz(\theta)/d\theta)^2}}\,|\vec{\omega}|$$

$$\omega_y(\theta) = \frac{dy(\theta)/d\theta}{\sqrt{(dx(\theta)/d\theta)^2 + (dy(\theta)/d\theta)^2 + (dz(\theta)/d\theta)^2}} |\overrightarrow{\omega}|$$

$$\omega_z(\theta) = \frac{dz(\theta)/d\theta}{\sqrt{(dx(\theta)/d\theta)^2 + (dy(\theta)/d\theta)^2 + (dz(\theta)/d\theta)^2}} |\overrightarrow{\omega}|$$

Thus,

$$\sqrt{\omega_x(\theta)^2 + \omega_y(\theta)^2 + \omega_z(\theta)^2} = |\overrightarrow{\omega}|$$

3.1.2 Study of the dynamics

The Reynolds number based on the circulation has been set to the same value as the one used when studying the knot configuration. That way

$$Re_\Gamma = 2000 \qquad \text{and} \qquad \tau = \frac{\Gamma\ t}{R^2}$$

The evolution of the topology of the initially writhed ring is presented in Figs. (3.4) and (3.5). It is quite easily noticed that the initial writhed topology seems to be conserved in a certain way. This is a first hint in the confirmation of the assumption that writhing helicity content may partially be protected from viscosity (note that being at $Re_\Gamma = 2000$, the present configuration is considered highly viscous). This topology conservation may be demonstrated by only looking at the vortex centerline of the structure. A tool for that extraction has been developed and used, and is presented in Appendix B. This evolution is depicted in Fig. 3.6. This indeed confirms that the initial geometry responsible for the apparition of a writhing helicity content is able to remain present in the ring as time evolves. This topological point of view will be largely further developed in Chapter 6, relative to the knot theory.

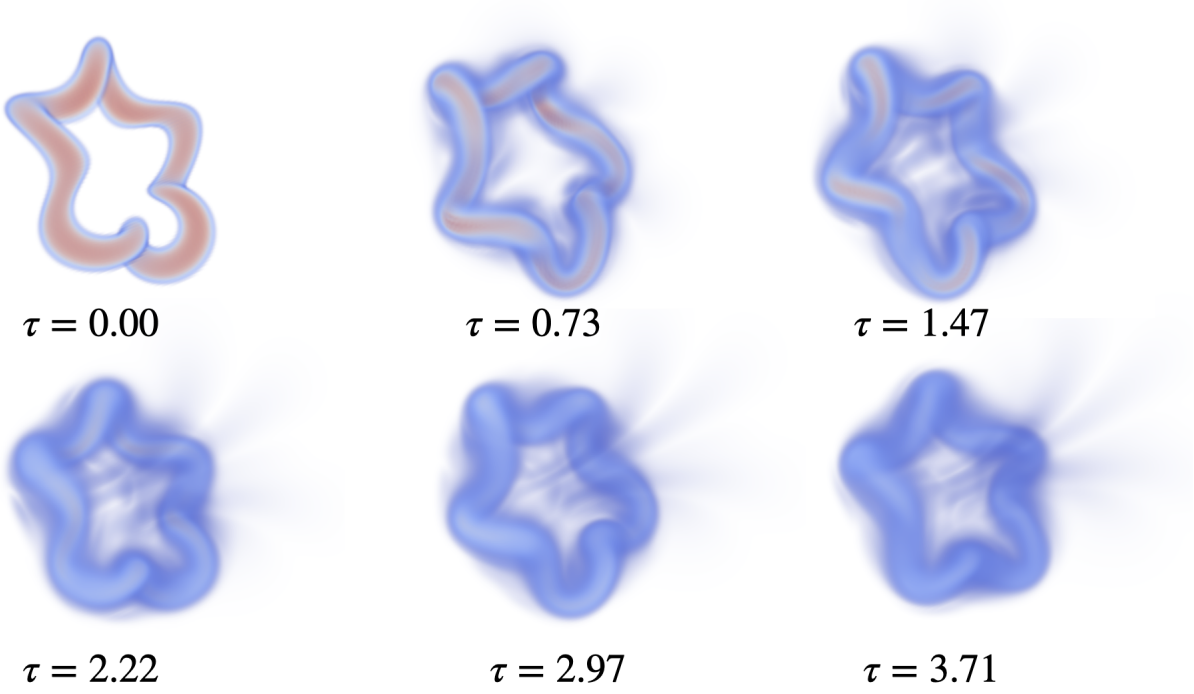

Figure 3.4: Evolution of the vorticity 3D rendering of the writhed ring

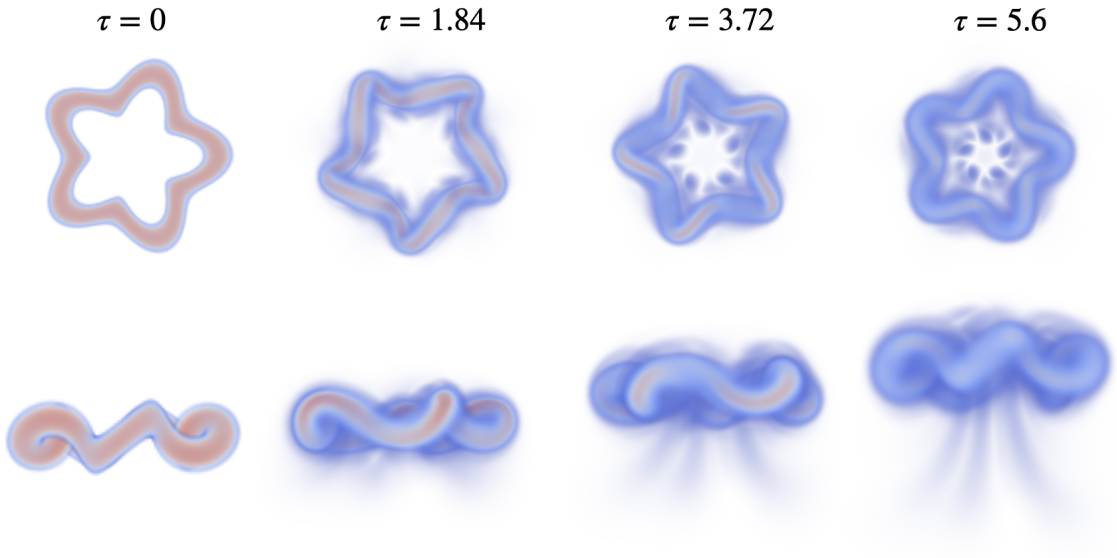

Figure 3.5: Evolution of the writhing containing ring - top and side views

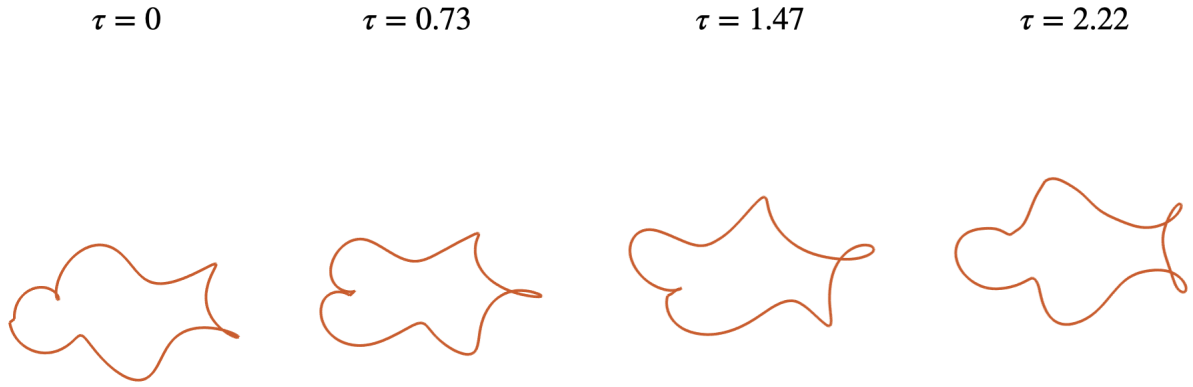

Figure 3.6: Evolution of the vortex centerline of the writhing containing ring

3.1.3 Helicity study

The evolution of the total helicity content of the writhed ring is depicted in Fig. 3.7 for $0 \leq \tau \leq 10$.

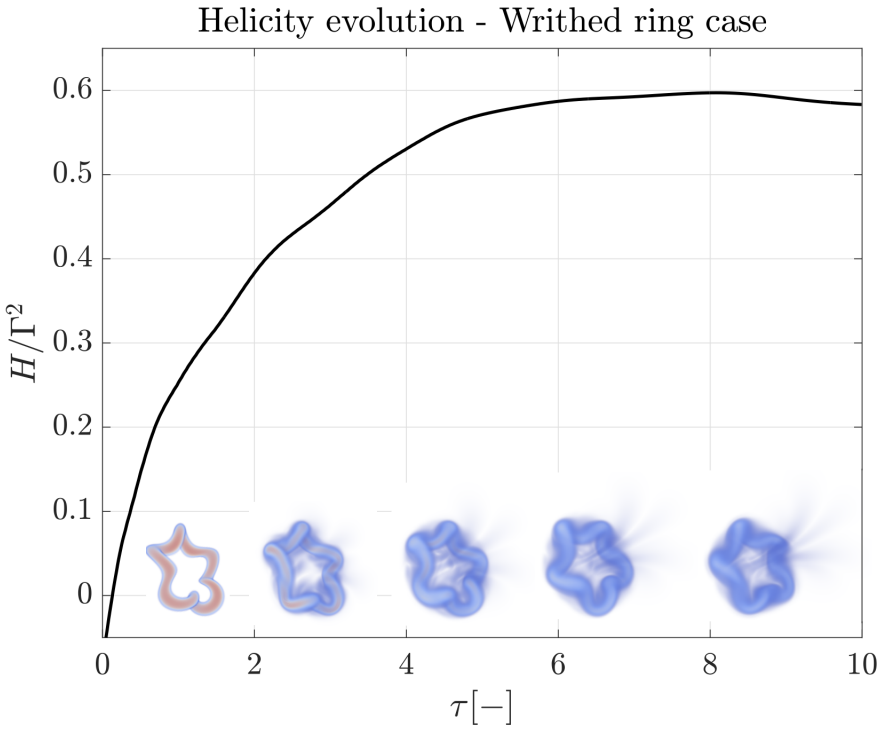

Figure 3.7: Helicity evolution of the writhing containing ring for $0 \leq \tau \leq 10$

As was highlighted by Scheeler and van Rees in [5], this initial helicity content is close to 0. This is most probably due to the fact that both twisting and writhing components are of opposite signs and hardly compensate each others, as developed in Chapter 6. But as the configuration here studied is highly viscous, not much time is needed for the twisting component (suspected of being highly

unstable under viscosity) to be dissipated.
It is thus observed that, as time evolves, the helicity content tends to the value of the writhing component. Indeed, for quite large τ, the helicoidal geometry responsible for the inducing of writhing is still present, and the total helicity content tends to a writhe content plateau. The latter conserves helicity on a time window of $\Delta\tau \sim 6$, after which it slowly dissipates, as will be further described later on.

The evolution of the iso-surfaces of vorticity for the writhed ring is presented in Fig. 3.8.

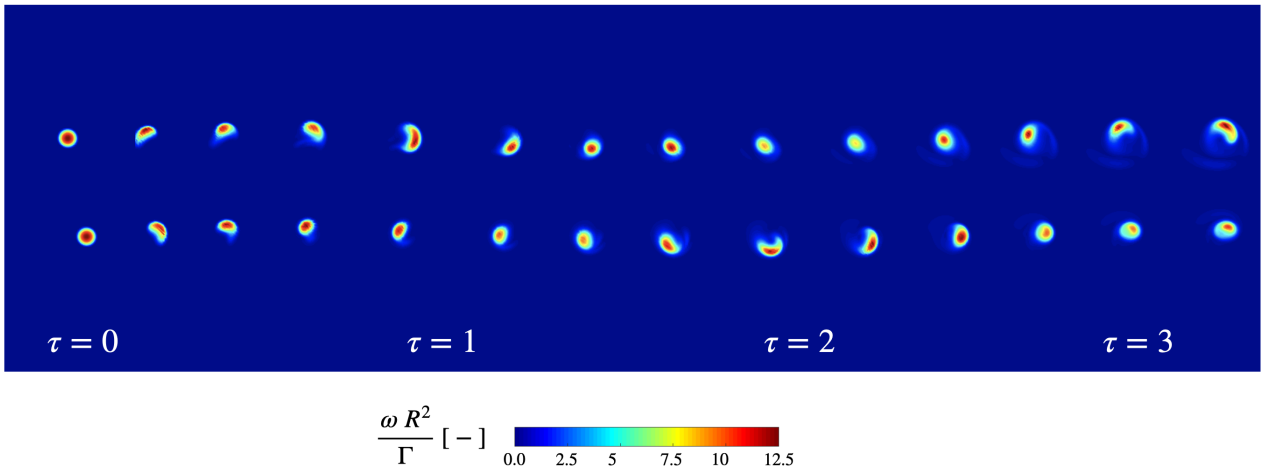

Figure 3.8: Evolution of the iso-vorticity slices of the writhing containing ring

Besides, the helicity evolution has been computed for different writhing containing geometries, represented in Fig. 3.9.

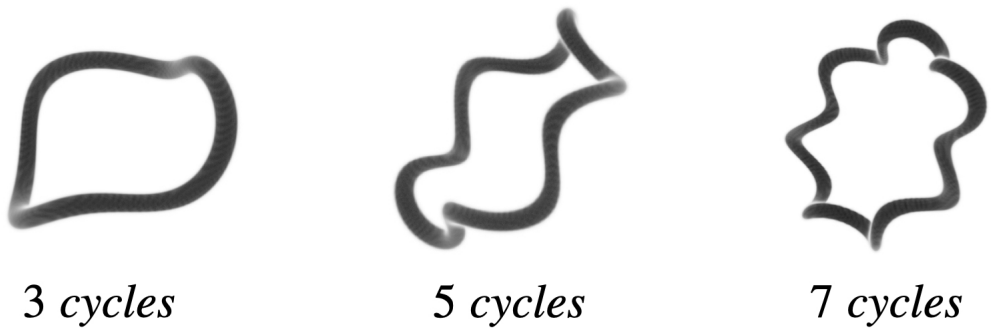

Figure 3.9: Topology of the 3 studied writhed geometries

The evolution of the helicity of the three situations is depicted in Fig. 3.10.

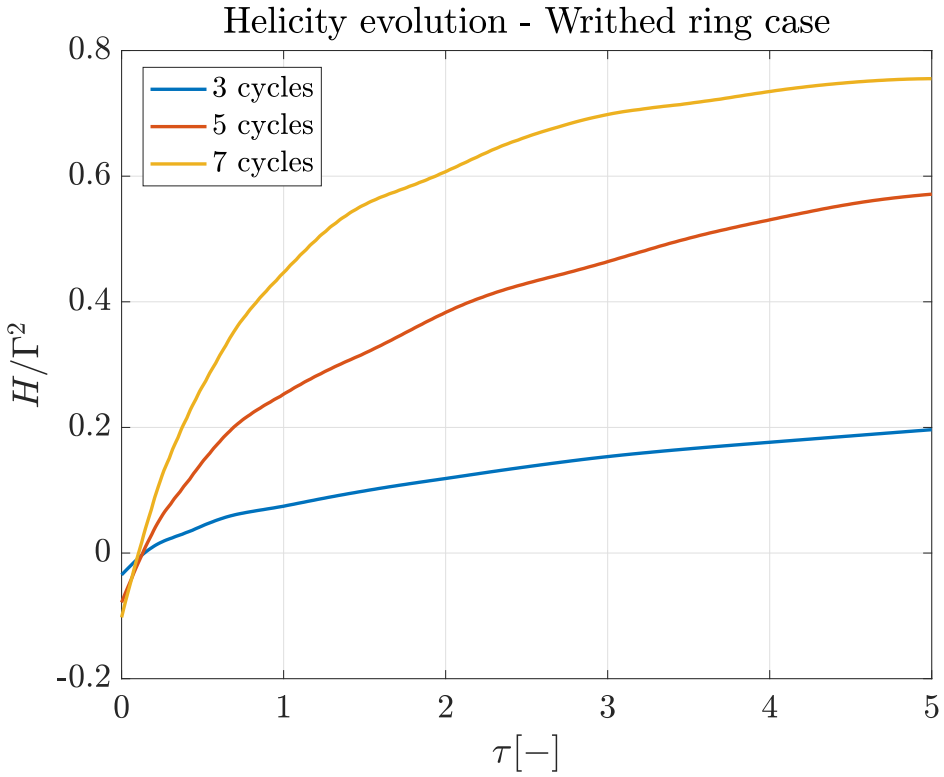

Figure 3.10: Helicity evolution - comparison between the 3 writhed geometries

Fig. 3.7 enables to suppose that, compared to twisting, writhing appears as a **stable storage mode**.
Moreover, Fig. 3.10 allows to deduce that the more the vortex centerline winds around itself, the more writhing helicity content is produced.

More advanced investigations about the potential protection of helicity by topological means are undertaken hereafter.

3.2 Closed vortex tubes with helicity content

3.2.1 The trefoil knot

Definition and initiation

The trefoil knot, when studying entanglement of vortex lines or simple contours, is a quite regularly studied case. This is a manner to analyse the evolution of a knotted configuration but with one and only vortex tube. Its mathematical expression is a parametric system of equations according to θ:

$$\begin{cases} x(\theta) = \sin(\theta) + 2\sin(2\theta) \\ y(\theta) = \cos(\theta) - 2\cos(2\theta) \\ z(\theta) = -\sin(3\theta) \end{cases}$$

This discretised geometry is represented in Fig. 3.11. It corresponds to an oscillating curve, closing after a period of 4π.

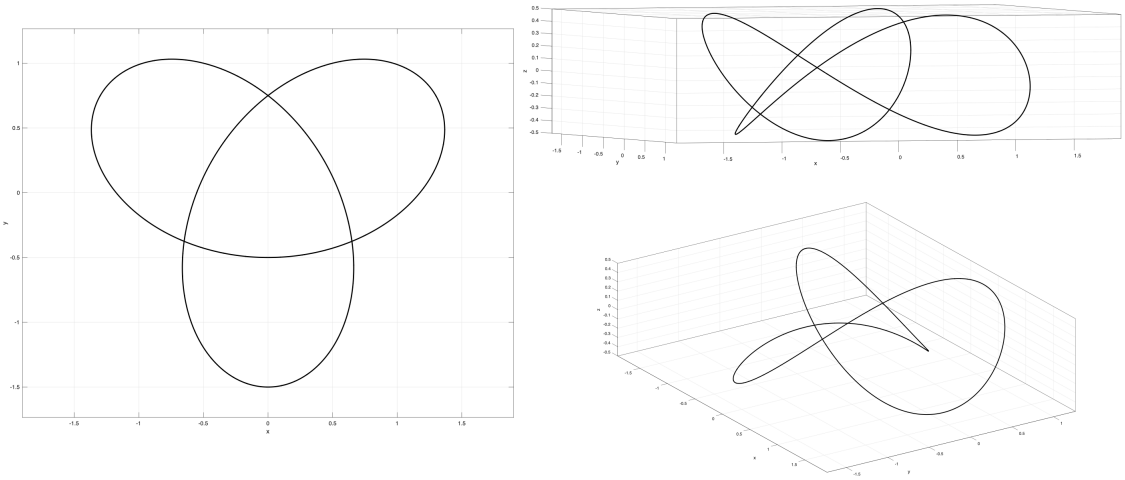

Figure 3.11: Representation of the discretised geometry for the trefoil knot

The latter geometry has served as the centerline for a vortex tube discretised in `VPM`, by comparing the distance of each point of the domain (d_{min}) to a certain threshold (the radius of the tube, σ_0) and associating those points a vorticity strength according to that minimal distance. That way, on each section of the vortex tube, vorticity is distributed following a compact Gaussian distribution, as the one presented earlier:

$$\text{For each node:} \qquad \omega(x,y,z) = \frac{\Gamma}{\pi\sigma_0^2} C(\beta^2) \exp\left(-\frac{(d_{min}/\sigma_0)^2}{(1-\beta^2(d_{min}/\sigma_0)^2)}\right) \tag{3.3}$$

Besides ω_x, ω_y and ω_z have been distributed such that the vorticity field is at each point tangent to the trefoil geometry and that $\sqrt{\omega_x^2 + \omega_y^2 + \omega_z^2} = |\omega|$.

Study of the dynamics

The evolution of the vorticity volume rendering is presented in Fig. 3.12 up to the separation of the trefoil into two structures (at $\tau \sim 4$), and compared to the density isosurfaces of the trefoil knot studied by Scheeler, 2014 [4].

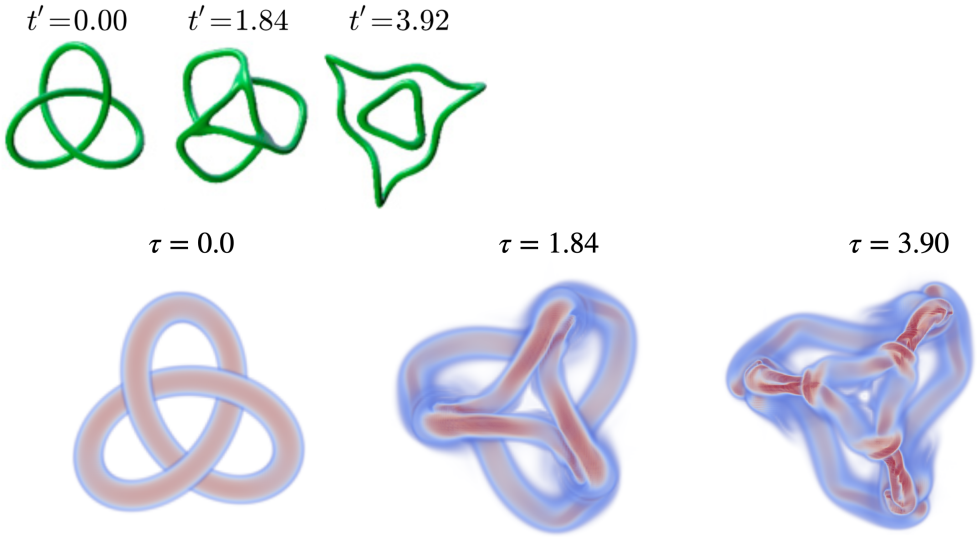

Figure 3.12: Volume vorticity rendering of the trefoil configuration for $0 \leq \tau \leq 4$

Furthermore, the evolution of the helicity of that trefoil configuration is presented in Fig. 3.13.

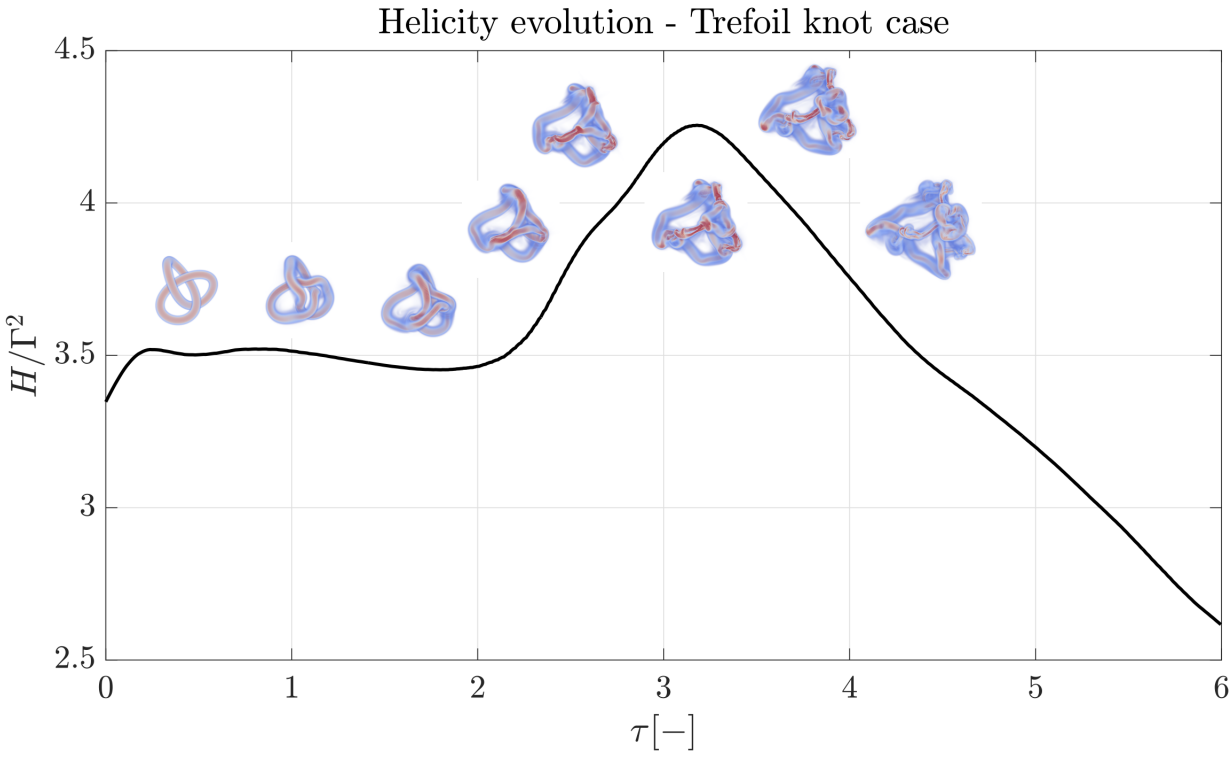

Figure 3.13: Evolution of the helicity content of the trefoil configuration with $Re_\Gamma = 2000$

The different stages of the evolution of the knotted vortex tube are quite readily identified:

- A first plateau of helicity content is observed, showing the ability of the topology to maintain its content as the vortex lines are still entangled.
- When the different portions of the vortex tube start to interact, the complexity of the flow raises, as some helicity content is created.
- Once the initial vortex knot has separated between two structures, the helicity content dissipates under the action of viscosity.

3.2.2 The periodic knots

After the study of the trefoil knot, presented in Section 3.2.1, the idea has merged to replicate the same methodology of initiation to implement a configuration where a single vortex tube would wind around itself and close after a certain number of periods, n_{period}. During those n_{period} rotations, the centerline would oscillate in both radial and tangential ($\hat{\mathbf{e}}_\mathbf{z}$) directions n_{cycles} times. That way, helicity content and topological evolution could be studied depending on the number of times the vortex lines of the tube would oscillate before closing the field.

Definition and initiation

The vortex centerline is, as was done for the trefoil knot, initiated based on a discretised geometry. The latter is described by the following parametric equations, depending on θ

$$\theta \in [0\ ;\ n_{period} \cdot 2\pi] \qquad L = 2\pi \cdot R \cdot n_{period} \qquad P = L/n_{cycles} \qquad f = 1/P$$

$$\begin{cases} r(\theta) = R + \sigma_0 \cdot \sin(2\pi\ f\ R\ \theta) \\ z(\theta) = \sigma_0 \cdot \sin(2\pi\ f\ R\ \theta\ +\ \pi/2) \end{cases}$$

The two determining parameters are thus n_{period}, the number of rotations performed by the tube before closing, and n_{cycles}, the number of oscillations performed by that tube during its n_{period} rotations, conferring writhing content. n_{cycles} has been fixed to 5, while the variation of n_{period} will be here studied. The different discretised geometries are described in Fig. 3.14.

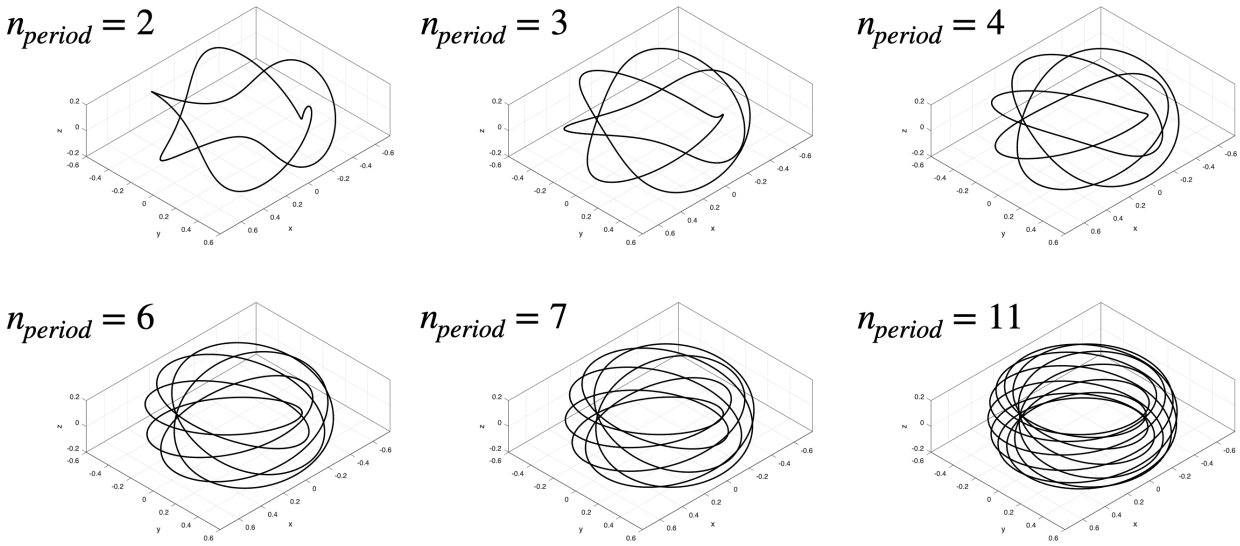

Figure 3.14: Description of the discretised geometry for the different periodic knots - $n_{cycles} = 5$

The criterion of vorticity initiation is the same as for the trefoil knot in Section 3.2.1: if the distance between the node and the discretised curve is lower than σ_0, vorticity is given following the well-known compact Gaussian distribution. The volume vorticity renderings of the curves in Fig. 3.14 are depicted in Fig. 3.15.

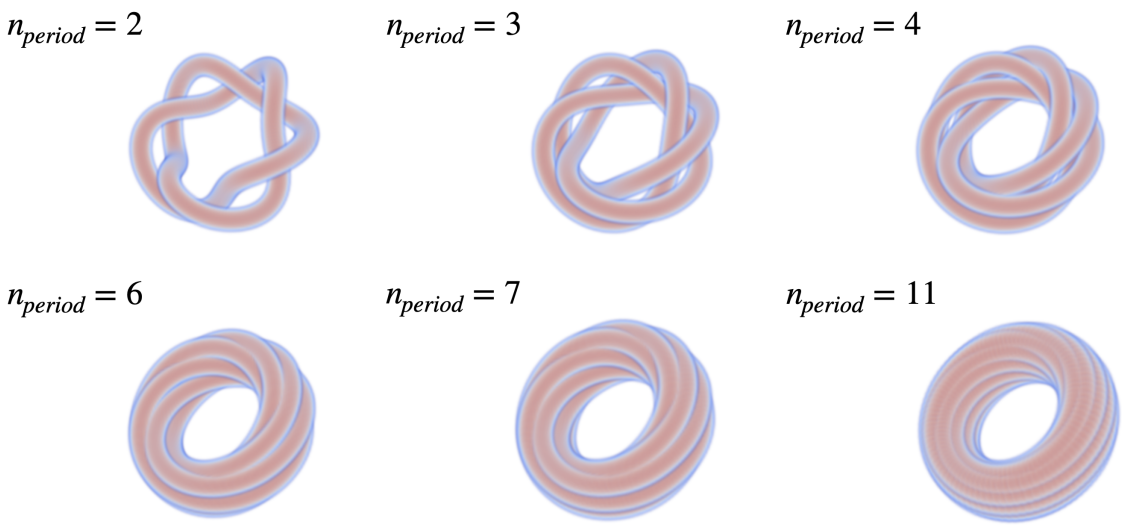

Figure 3.15: Volume rendering of the vorticity fields for the different periodic knots - $n_{cycles} = 5$

Helicity study

The evolutions of the helicity content of the previously presented configurations are presented in Fig. 3.16. For each of the structures, the helicity content is normalised by the circulation of a cross section, i.e. the circulation of the knotted vortex tube, multiplied by the n_{period} passages.

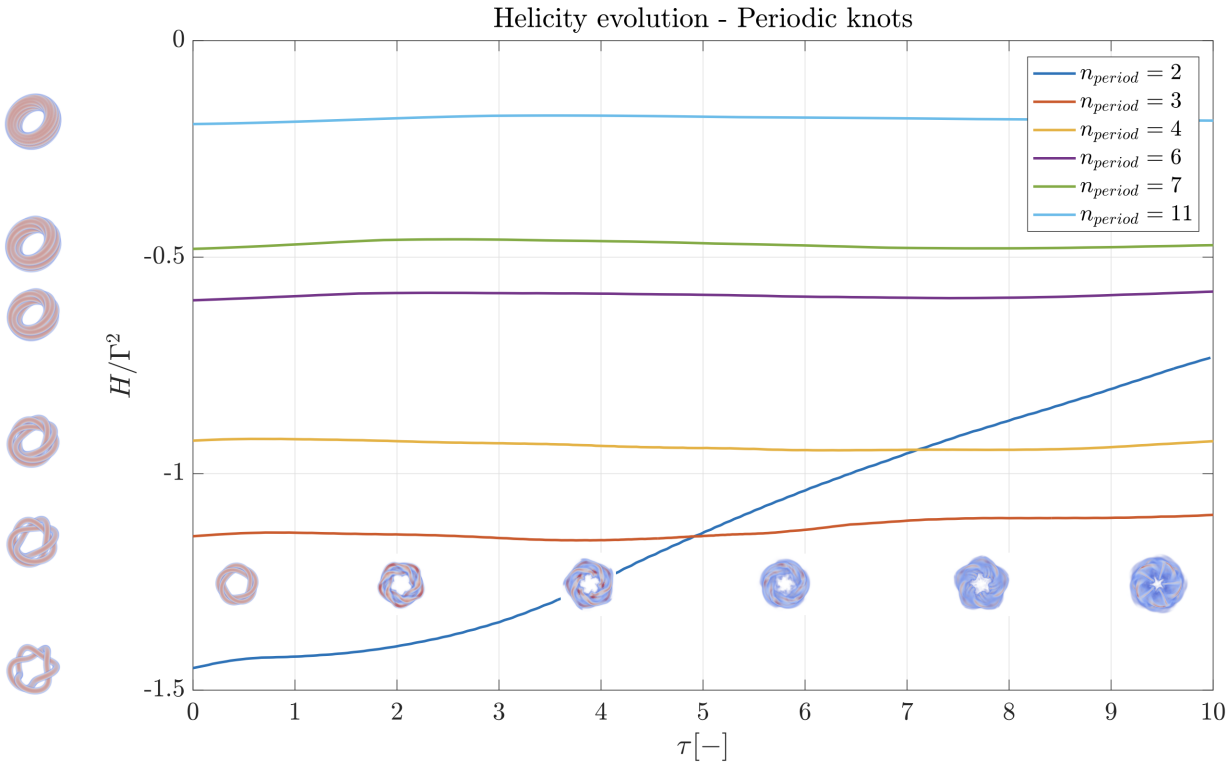

Figure 3.16: Evolution of the helicity content of the different vortex knots

Finally, the evolution of the iso-vorticity surfaces is described in Fig. 3.17, for $n_{period} = 3$ and $n_{cycles} = 5$.

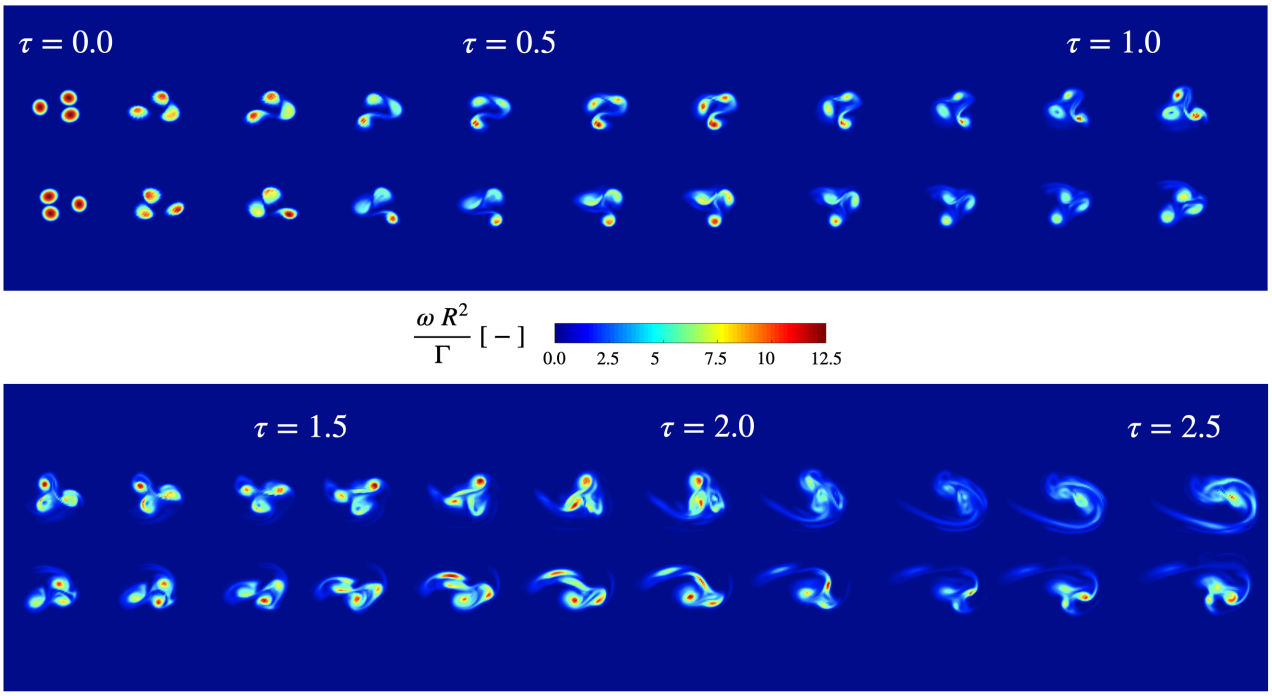

Figure 3.17: Evolution of the iso-vorticity surfaces of the periodic knot, $n_{period} = 3$ and $n_{cycles} = 5$

Based on Figs. 3.16 and 3.17, the conclusion is drawn that the conservation observed in the helicity content of the periodic knots is highly due to topological reasons, as is also discussed in Chapter 6. Besides, the more the tube is winded around itself, the more the helicity content is conserved, and protected from viscous effects. It is also important to note that the global helicity content of the case with $n_{period} = 11$ is way larger (in absolute value) than the one of the case with $n_{period} = 3$, in opposition with what could be understood by looking at the dimensionless helicity quantities.

3.3 Leapfrogging between two vortex rings

The leapfrogging phenomenon between two vortex rings is a recurrent subject in the study of the dynamics of interacting vortical structures. Most of the time, two planar rings are considered, but this case may also be applied to more than two rings, as well as to writhed ones.

The leapfrogging effect is due to the induced velocity field of the first (front) ring, forcing the second one to enter its structure and become the new front ring, as illustrated in Fig. 3.18.

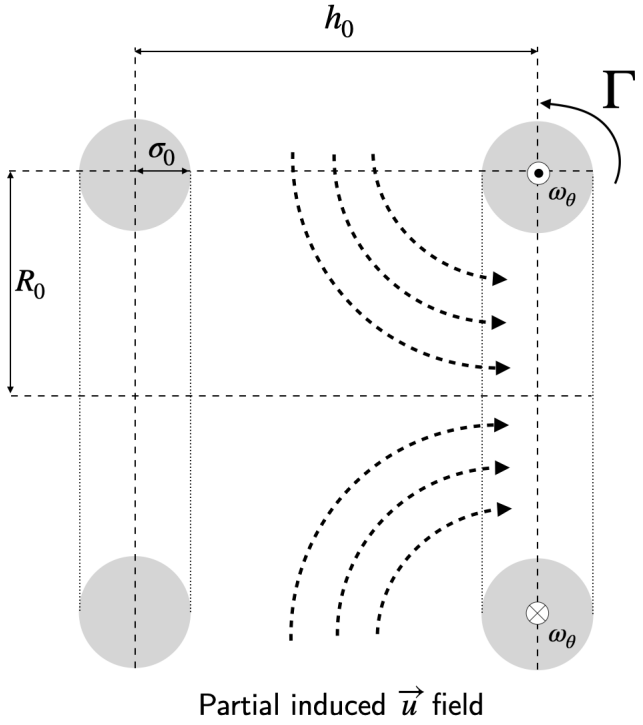

Figure 3.18: Schematic representation of the leapfrogging phenomenon between two planar rings

The previously evoked case with the interaction between one writhed ring and a planar one is an opportunity to study the helicity evolution of a new configuration as well as to confirm results and conclusions obtained with the other configurations.

First, a simulation with two planar rings is performed, in order to correctly initiate the configuration. Then, the setup is adapted to two different configurations implying one writhed ring and one planar one.

Leapfrogging between two planar rings

The leapfrogging dynamic and the success of it highly depends on the geometry of both rings, as well as the Reynolds number of the configuration. This dependance has been studied in [10]. This

has enabled to select the different parameters:

$$\frac{\sigma_0}{R_0} = 0.1 \qquad \frac{h_0}{R_0} = 1 \qquad Re_\Gamma = \frac{\Gamma}{\nu} = 2000$$

The evolution of the topology of both rings is illustrated in Fig. 3.19, for half a leapfrog period (i.e. the rear ring becomes the front one and vice versa).

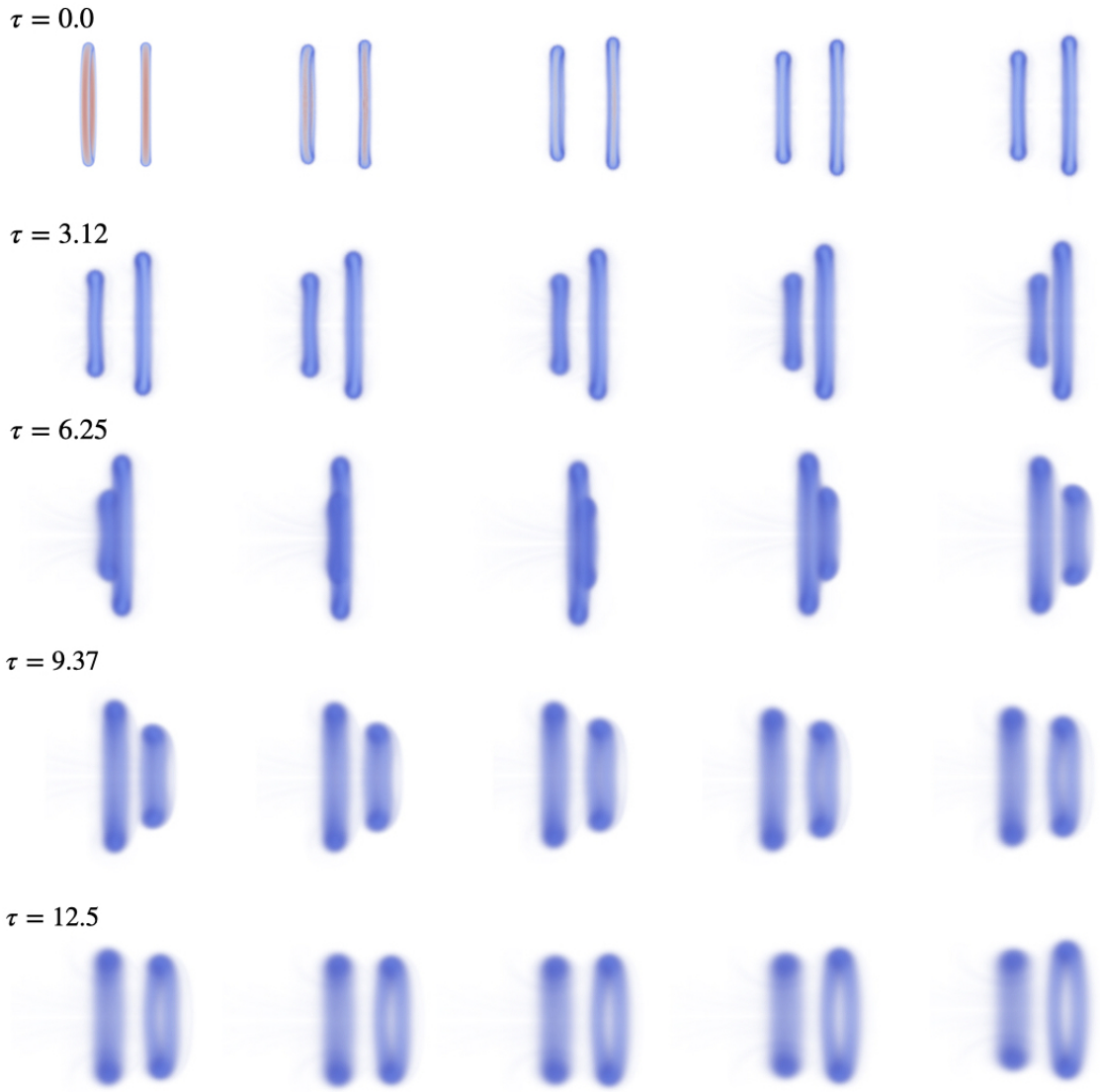

Figure 3.19: Leapfrogging phenomenon between two planar rings - volume vorticity rendering

The slices of the iso-vorticity are depicted in Fig. 3.20 for $10 \leq \tau \leq 20$, thus describing the interaction between both structures when one passes through the other.

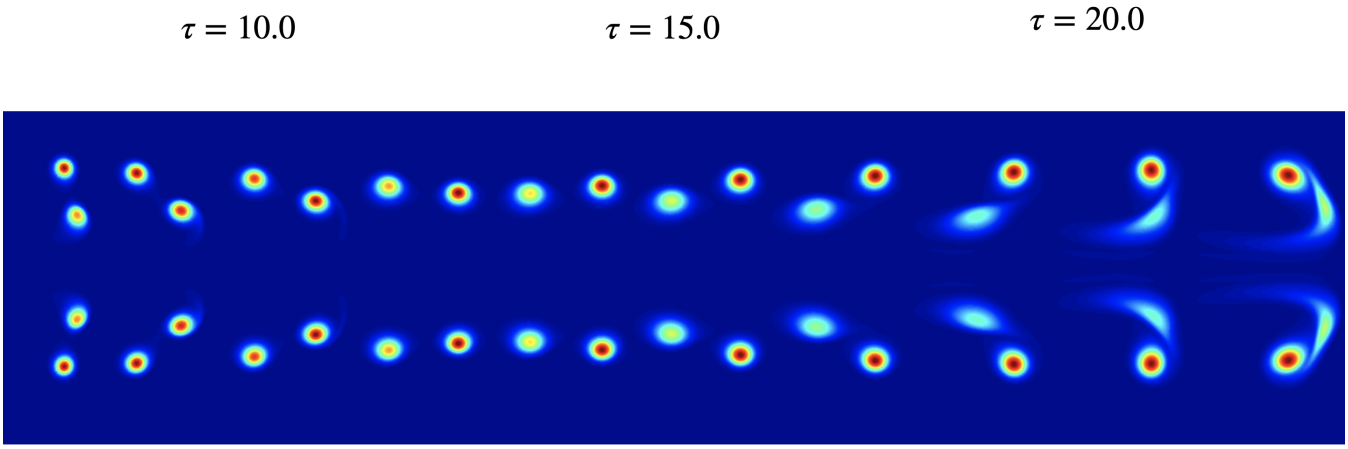

Figure 3.20: Iso-vorticity slices of the leapfrogging phenomenon for two planar rings - $10 \leq \tau \leq 20$

The initial condition is deprived from helicity, as each ring is planar. As shown in Fig. 3.21, no helicity content is created when both rings leapfrog. The following configuration will study the evolution of the helicity content of a writhed ring leapfrogging with a planar one, thus with variation of the initial helicity content.

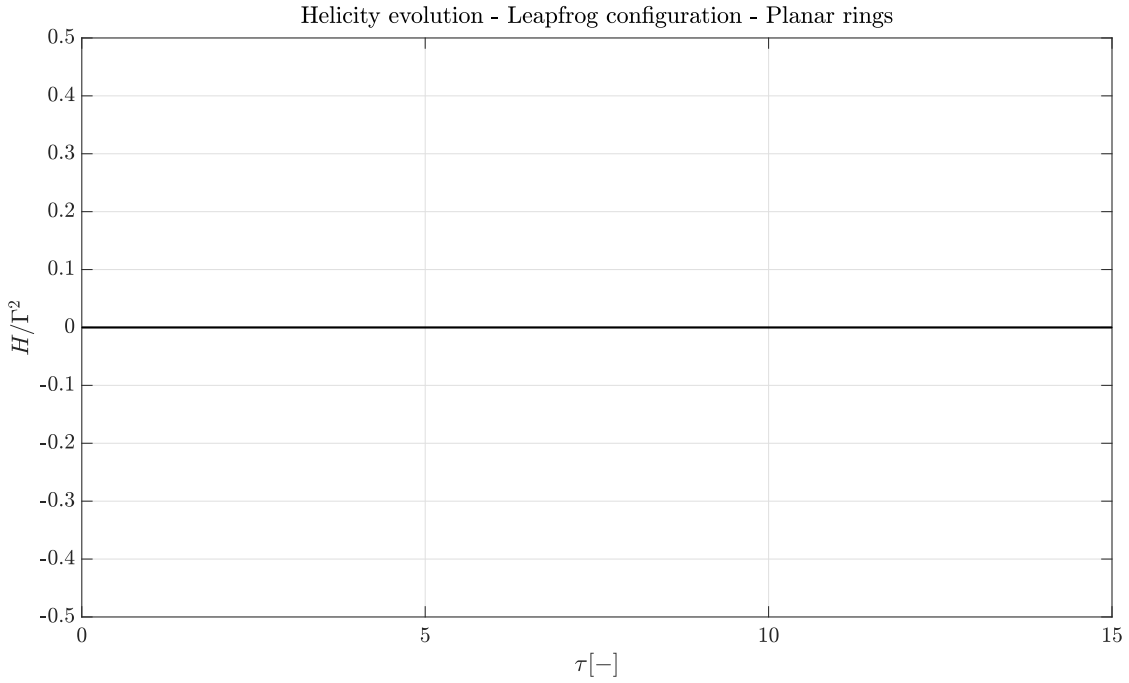

Figure 3.21: Helicity evolution of the leapfrog configuration between two planar rings

Leapfrogging between a writhed ring and a planar ring

Using the same geometrical parameters and Reynolds number as in the previous subsection, one of the ring has been replaced by a writhed one, as the one studied solely in Section 3.1.

Two configurations are to be considered: the first one where the writhed ring first enters into the planar one's structure, and the second one where the planar ring first enters into the writhed one's structure, as shown in Fig. 3.22.

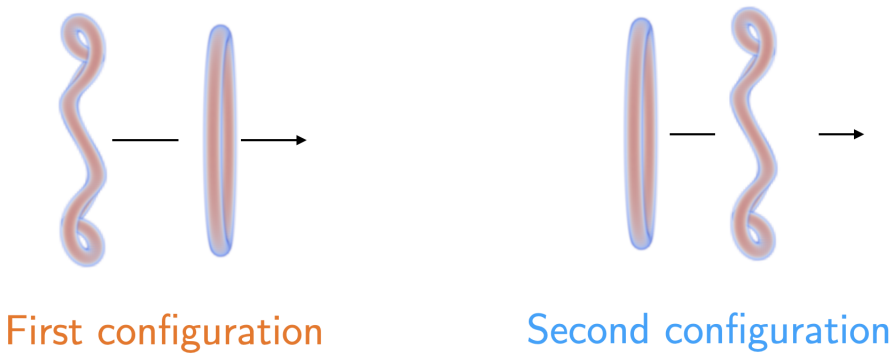

Figure 3.22: Initial condition of both studied configurations

First configuration

First of all, it is of particular interest to present which behaviour is expected, if any viscous dissipation should be omitted. In the case of a completely inviscid evolution, and with vortex lines evolving as material ones, the helicity content would be identically conserved. This would result in a constant compensation of the twisting component with the writhing one. This is illustrated in Fig. 3.23, for one leapfrog period. Loci of maximal writhe correspond to a situation where the writhed ring is maximally compressed inside the planar one, minimising that way his twisting content. On the opposite, loci of maximal twisting correspond to a situation where the writhed ring is maximally extended, i.e. where the planar one is compressed inside of its topology. This redistribution of the total (and here constant) helicity content is illustrated in Fig. 3.24, from [5], and in Fig. 3.25 in the case of rings.

It is to be mentioned that, most of the time, when such configurations are studied in the literature, the following hypotheses are made, but will not apply in the hereunder highly viscous studied case:

- The helicity of the planar ring may be omitted all along the evolution.

  This is not possible here because, as will be observed later on, the interaction between both rings is quite important, which induces a transfer of helicity from the writhed ring to the planar one.

- The linking component of the system is identically null.

  Indeed, geometrically speaking, both rings are not linked. However, as both structures will act on each others, the velocity/vorticity fields of $ring_1$ will have an impact on the fields of $ring_2$, mathematically creating a linking content in the global helicity.

The reason why those hypotheses are of use in the literature is that studied configurations (see [5]) are often of the order of $Re_\Gamma \sim 12\,000 - 20\,000$. For those cases, only measuring the helicity of the writhed ring is sufficient to fully characterise the configuration.

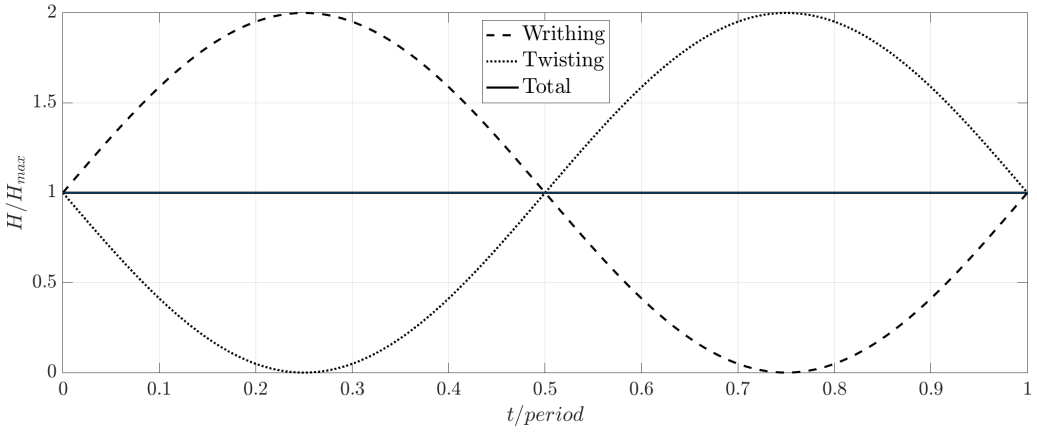

Figure 3.23: Evolution of the helicity components for the leapfrogging between a writhed and a planar ring, in an inviscid configuration

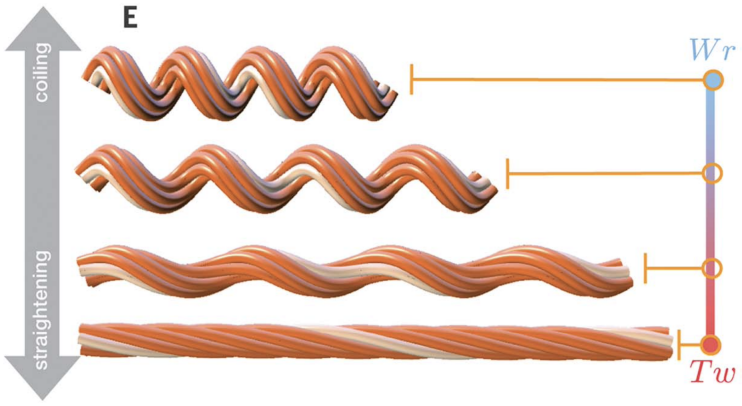

Figure 3.24: Redistribution of the helicity content from writhe to twist and vice versa - Scheeler 2017

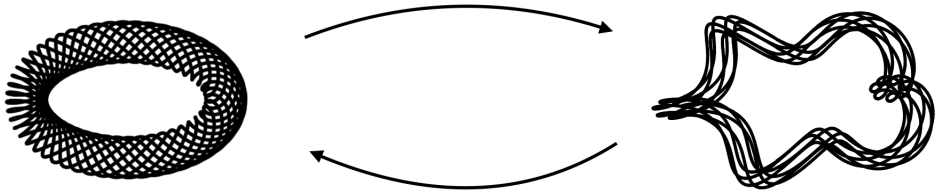

Figure 3.25: Redistribution of the helicity content from writhe to twist and vice versa - Vortex rings schematic

The evolution of the configuration is presented in Fig. 3.27, for half a leapfrog period. The helicity evolution of that first configuration is illustrated in Fig. 3.28. From it, the following steps are identified. Fig. 3.26 refers to those steps.

1. As was observed in Section 3.1, the initial rough compensation between the writhing and the twisting components quickly disappears: the twisting, non-stable, directly dissipates making the global content tend towards the writhing one. The first helicity raise for $0 \leq \tau \leq 4$ is a result of that presumed twisting dissipation.

2. Then, the writhed ring compresses, forced to enter the planar one's structure. This has the effect of increasing the total helicity content, from $\tau = 4$ to $\tau = 7$.

3. After his passage through the planar ring, the writhed one exits it and both structures strongly interact. This has the effect of destroying some helicity content, but also and mainly to confer a writhed topology to the initially planar ring.

4. As the previously planar ring has become writhed, it is his turn to enter the other ring's structure. This compression has the effect of increasing again the total helicity content, reaching the second local maximum at $\tau = 15$.

5. From this time on, both writhed rings go on interacting, dissipating and finally merge into one bigger structure.

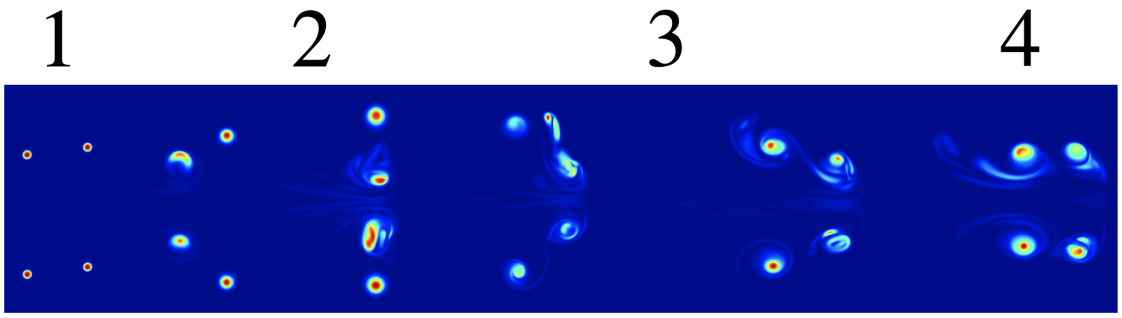

Figure 3.26: Iso-vorticity slices of the leapfrogging configuration for one writhed ring

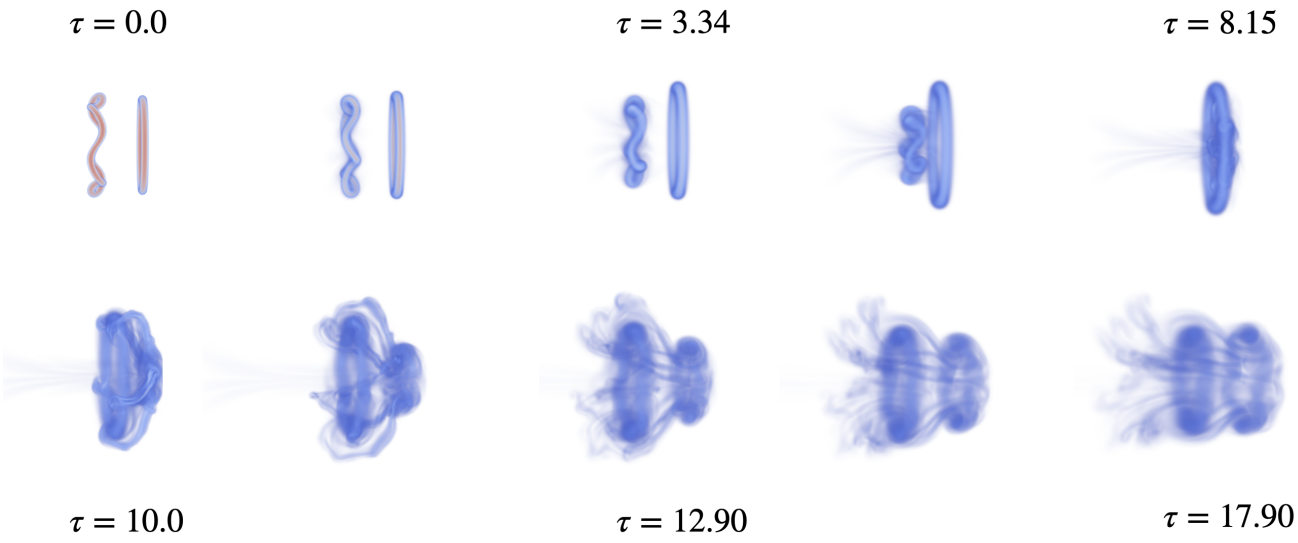

Figure 3.27: Leapfrogging phenomenon for a writhed and a planar ring - Configuration 1

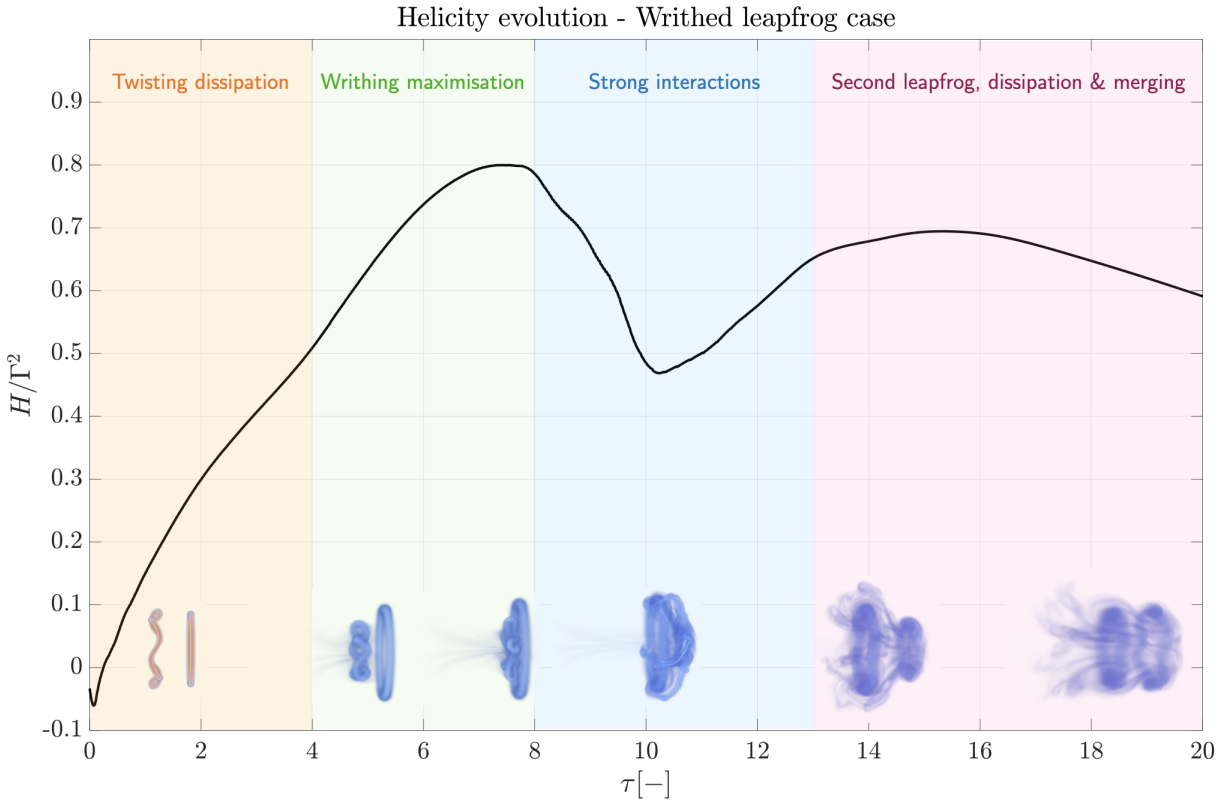

Figure 3.28: Evolution of the helicity content of the writhed leapfrogging - Configuration 1

The mask function implementation described in Appendix A has been here used to study the transfer of helicity from one ring to another. It is to be mentioned that its use is not perfect here, as the masks do not diffuse sufficiently compared to the vorticity field they intercept. However, the following conclusions can safely be drawn from the analysis of those separated fields:

- The initial helicity content is only due to the writhed ring and the tendency to its writhing content, while dissipating its twisting component.
- The first decrease of helicity, from $\tau = 7$ to $\tau = 10$ is associated with an increase of the linking component: both rings interact, so do the velocity and vorticity fields.
- Immediately after that linking increase, the latter decreases to the benefit of the second (planar) ring content: the first (writhed) ring has transferred some helicity content to the second one, and this is visibly associated to a transformation of topology of the initially planar ring, as depicted in Fig. 3.29.

Fig. 3.29 puts in parallel the interaction between both rings with the evolution of the total enstrophy of the configuration. Enstrophy reflects the complexity of a turbulent flow, and locally increases as both rings interact, transferring helicity from one to another.

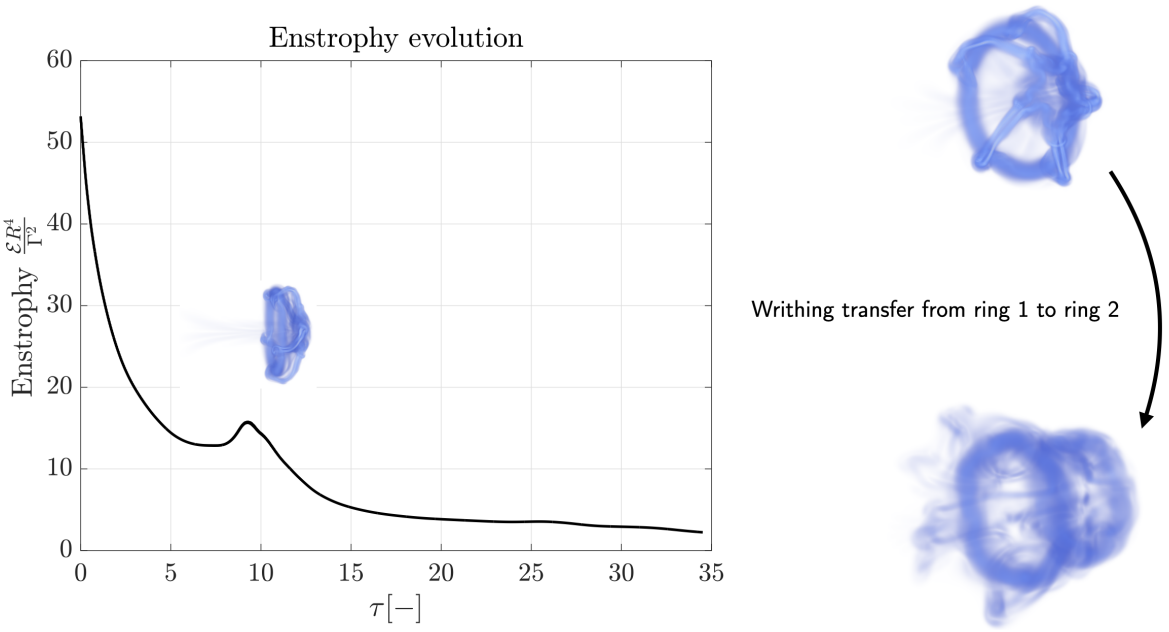

Figure 3.29: Illustration of the change in topology of the initially planar ring, in parallel with the change in enstrophy associated with that interaction

Second configuration

A second configuration, where the planar ring first enters the writhed one, thus expanding it, has been studied.

In a global way, the evolution of that configuration may be seen as the same as the first one, but simply shifted of half a leapfrog period. Indeed, after the planar ring has entered and exited the writhed one, the configuration thus obtained corresponds to the first one. However, further conclusions may be drawn as well.

The evolution of the configuration on the first half period is presented in Fig. 3.30.

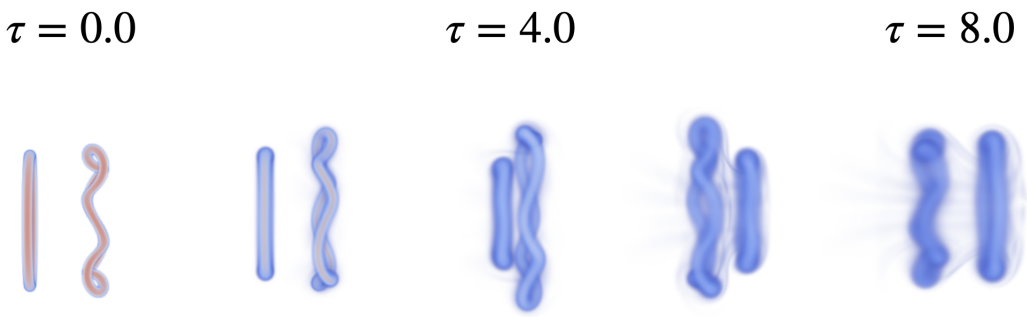

Figure 3.30: Evolution of the second configuration for the first half-period of leapfrogging

The helicity evolution of that second configuration is depicted in Fig. 3.31.

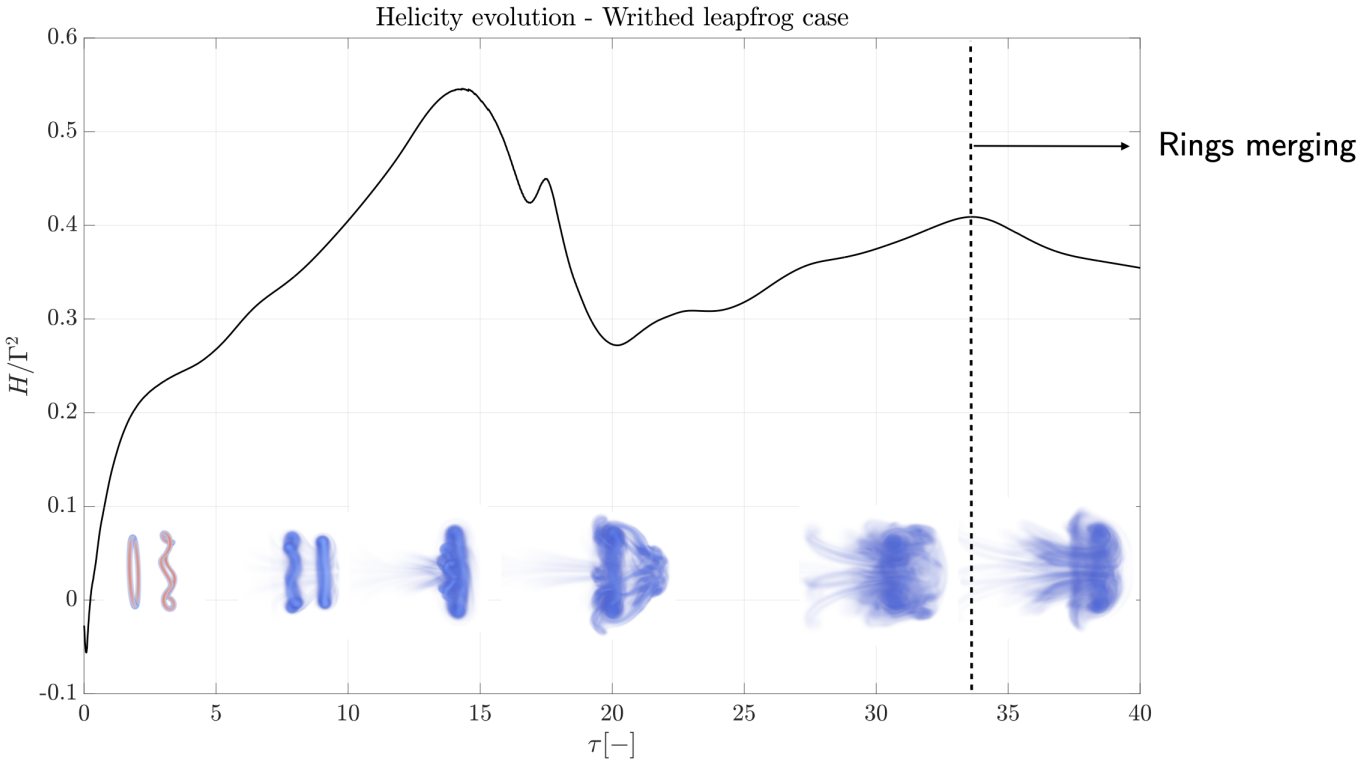

Figure 3.31: Evolution of the helicity content of the writhed leapfrogging - Configuration 2

From Fig. 3.31, the following steps are identified:

1. The first raise in helicity is due to the same phenomenon as described for the previous configuration and in the lonely writhed ring case: the dissipation of the twisting component.
2. This first raise is carried while the writhed ring is expanded due to the passage of the planar one inside its structure. The compression of the writhed ring then leads to the first local maximum at $\tau = 14$.
3. The next steps are the same as the one described for the first configuration. However, as everything has been delayed by half a leapfrogging period, the dissipation has acted more on the fields before the rings reach the second local maximum. That way, from $\tau = 33$, both structures have merged.

The merging of both rings is illustrated in Fig. 3.32. The resulting ring is a writhed one, evolving on its own.

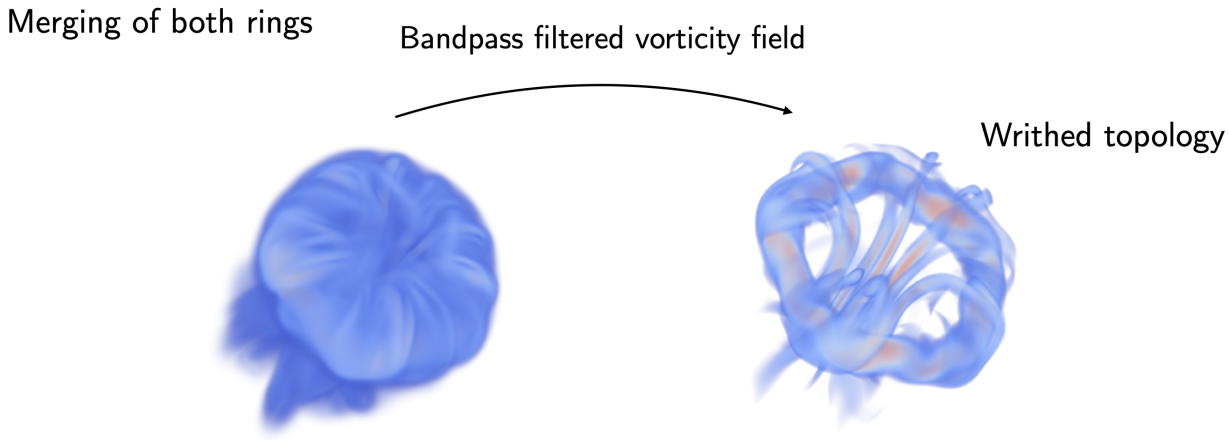

Figure 3.32: Volume rendering of the vorticity of the merged rings resulting into one writhed ring

The evolution of the latter merged structure is highly comparable to the one of the lonely writhed ring studied in Section 3.1: it rolls on itself, while conserving a writhed topology.

The fact that the leapfrogging configuration ends on a single writhed ring, dissipating, tends to confirm the previously established conclusions: a vortex ring configuration, if the latter allows it, will tend to transfer its helicity content to the writhed component, appearing as the most stable storage mode for helicity. The latter then dissipates under the effect of viscosity.

A last mode has however still not been investigated yet, which is twisting.

Chapter 4

The twisting content

The nature itself of the twisting helicity component makes it quite challenging to study. It is reminded that it constitutes the only storage mode which requires the consideration of the whole vortex tube, i.e. the action of each vortex line on its own. Indeed, as the study of the vortex centerline on its own was theoretically sufficient to characterise both the linking and the writhing mode, that is no longer the case for twisting. In other words, twisting is qualified as an intrinsic helicity storage mode: the centerline of the tube may be completely deprived from helicity content, it would although be possible for the tube to rotate on itself as to create some twisting.

In Chapter 2, using a separation between the fields of both rings, it has been identified that, through a reconnection event, linking had transferred its contribution to what has been calculated to be "writhing + twisting". By studying a writhing containing ring in Chapter 3, the assumption has been raised that it was actually the writhing content that could collect the presumably unstable twisting content.

This chapter, dedicated to the twisting mode, has the goal to isolate the latter component in order to confirm the previously evoked suspicions: is twisting considered as an unstable helicity component, to what extend, and may writhing be seen as a shelter for the helicity content?

Two approaches have been followed in order to characterise twisting: a discrete one and a continuous one. The first approach aims at dealing with bundles of vorticity filaments whereas the second one aspires to implement a continuous (yet of course limited by the grid resolution) twisted field.

4.1 Discrete approach - Twisted bundle of filaments

4.1.1 Ring initiation

When only considering twisting, the combination of the winding of each vortex line along the center one contributes to the twisting helicity, while the vortex centerline is purely circular (or planar), i.e. not winding on itself. In order to characterise this mode, it is of use to talk about a **bundle of vortex filaments**: the agglomeration of many filaments of different circulation creates a pack (bundle), forming the macro-vortex ring. For a regular vortex ring (not twisted, nor containing any sort of helicity), this is schematically depicted in Fig. 4.1.

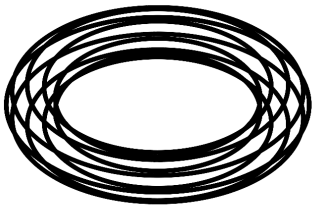

Figure 4.1: Schematic representation of a bundle of aligned vortex filaments to create a vortex ring

Thereby, by considering the same geometry as described in the writhed case, a bundle of writhed filaments could be formed, producing a twisted ring. Fig. 4.2 depicts the completion of the outer layer of a twisted ring with 1, 10 and 50 writhed filaments.

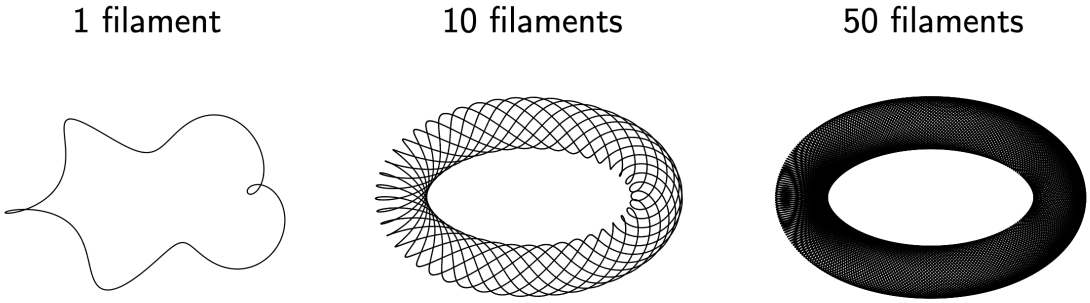

Figure 4.2: Outer layer of a twisted ring with $n = 1$, 10 and 50 filaments

In order to obtain a filled cross section, the geometry represented in Fig. 4.3 is considered (from the PhD thesis of Pr. Grégoire Winckelmans). The twisted ring is made of n_{lay} layers in addition to the centerline, and where the n^{th} layer contains $(4 \cdot 2n)$ filaments, so that each filament lies in a 2D cell of surface $S_f = \pi r_l^2$.

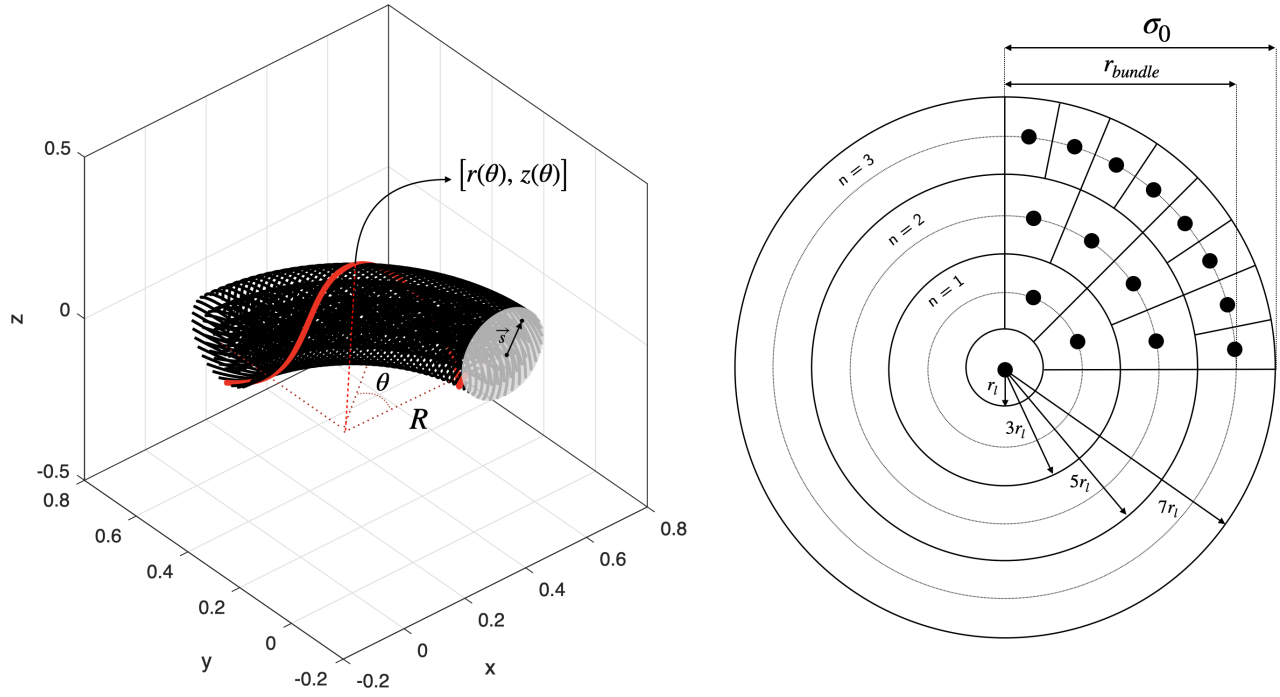

Figure 4.3: Configuration of the cross section of the discretised twisted ring using layers of vortex filaments

The discrete ring presented in this section contains $n_{lay} = 3$ layers, which results in 49 filaments.

The initiation of the centerline geometry of each filament is performed in the same way as was done for a single writhed ring (Section 3.1), with additional geometrical factors.

One filament is highlighted in red in Fig. 4.3. For the n^{th} layer of the ring:

$$\begin{cases} r(\theta) = R \ + \ 2n \ r_l \ \sin\left(2\pi \ f \ R \, \theta + \theta_{offset}\right) \\ z(\theta) = 2n \ r_l \ \sin\left(2\pi \ f \ R \, \theta + \pi/2 + \theta_{offset}\right) \end{cases}$$

With

$$f = \frac{1}{P} \qquad P = \frac{L}{n_{cycles}} \qquad L = 2\pi R \qquad n_{cycles} = 5$$

θ_{offset} ensures that, in a certain layer, the m_{fil} filaments are distributed uniformly on the outer surface of the layer.
Concerning the vorticity distribution across the section of the ring, each of the filament is characterised by a circulation. The latter depends on the layer in which it lays. For the layer n:

$$\Gamma_n = 2\pi \int_{(2n-1)\ r_l}^{(2n+1)\ r_l} \omega_\theta(s) \ s \ ds \tag{4.1}$$

Thus also, for the centerline

$$\Gamma_0 = 2\pi \int_0^{r_l} \omega_\theta(s)\ s\ ds \tag{4.2}$$

Ensuring well that $\sum_{i=0}^{n} \Gamma_n = \Gamma$.

This is represented in Fig. 4.4. The circulation of each layer is divided by the number of filaments in the layer, and plotted against the layer number n.

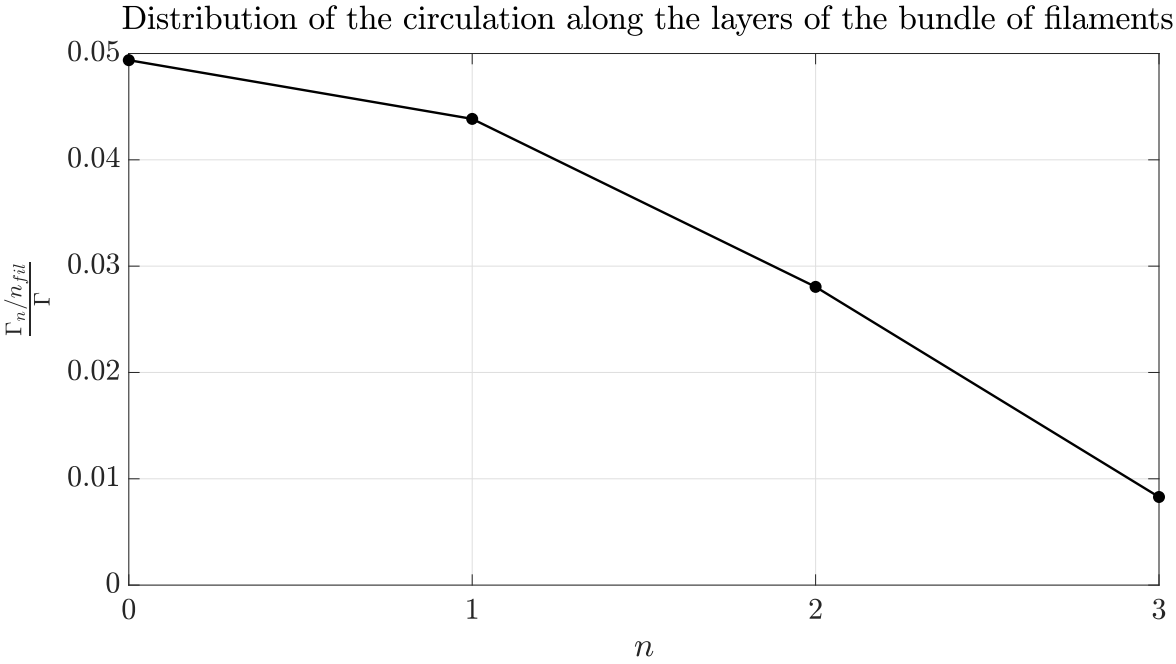

Figure 4.4: Distribution of the total circulation among the layers of filaments constituting the discretised ring

That way, each filament belonging to a same layer has the same circulation, as the latter only depends on the distance from the centerline.

4.1.2 Study of the dynamics

The ring has been discretised on a 513^3 periodic grid, and the simulation is run at $Re_\Gamma = 2000$.

The initiated ring and its cross section (displaying the iso-vorticity surfaces) are represented in Fig. 4.5.

The evolution of his topology is presented in Fig. 4.6, with a schematical representation of the evolution of the bundle of filaments. The topological analysis of this evolution seems to unveil the fact that the helicity initially present in the form of twisting will transfer into the form of writhing.

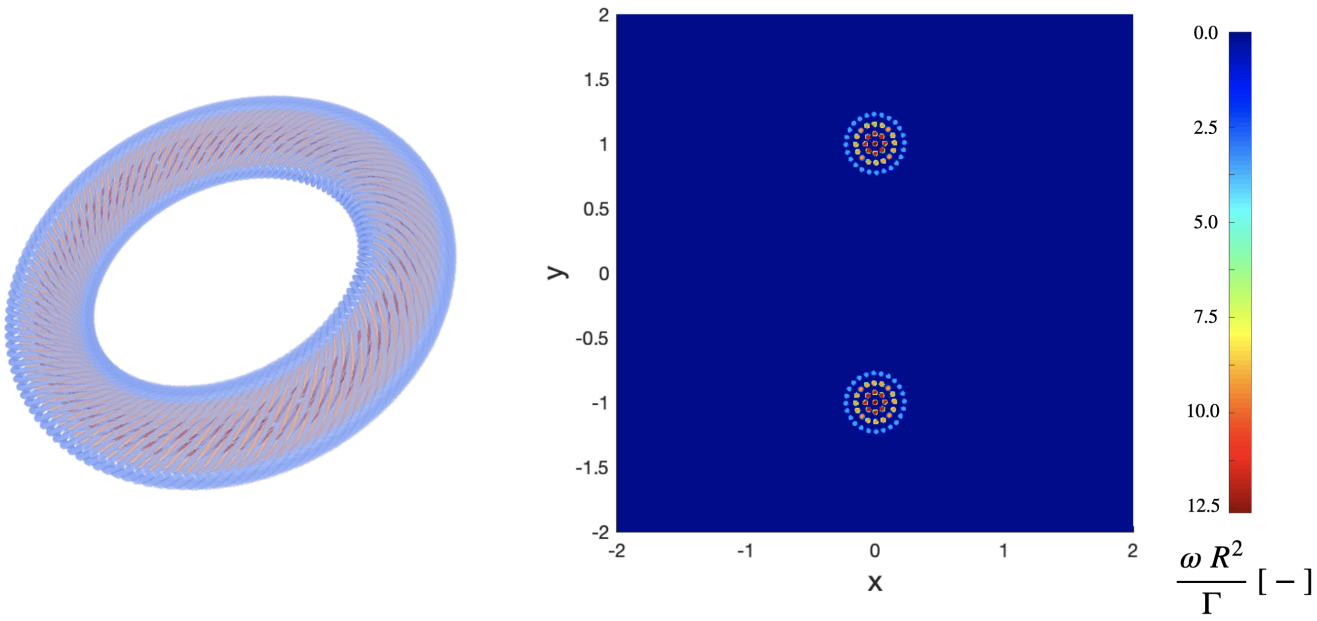

Figure 4.5: Initial geometry and cross section of the twisted ring

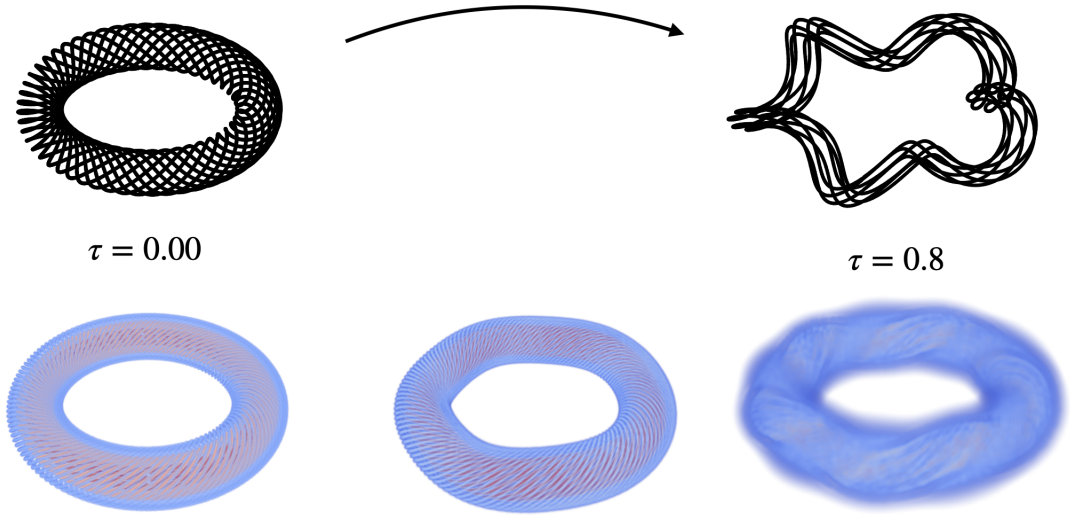

Figure 4.6: Evolution of the topology of the discretised twisted configuration

The evolution of the helicity is presented in Fig. 4.7.

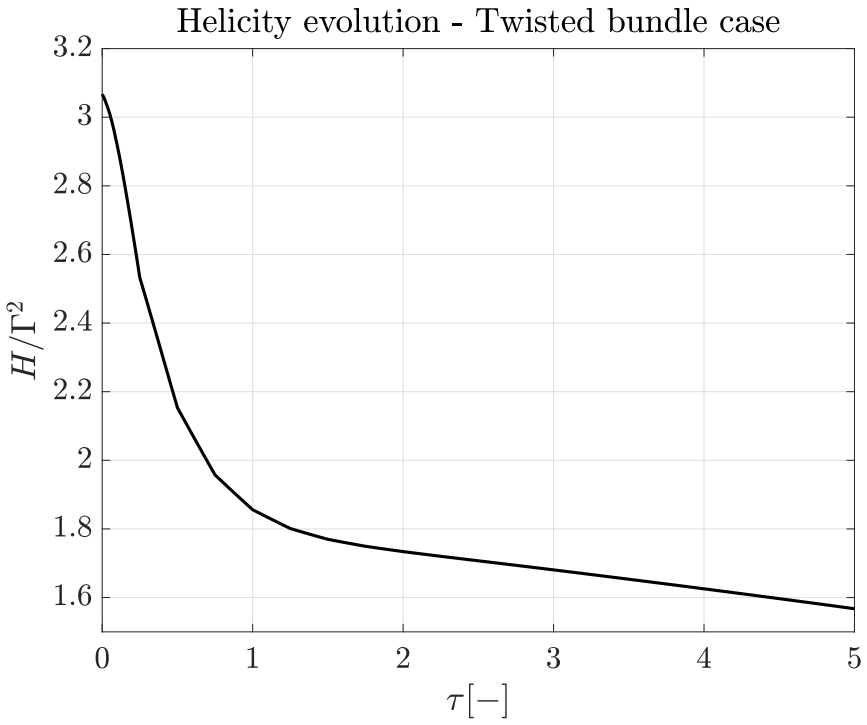

Figure 4.7: Evolution of the helicity of the twisted configuration

The first fast drop of the helicity corresponds quite surely to the dissipation of the twisting content, which confirms that the latter diffuses naturally under the effect of viscosity. Past $\tau = 1$, the dissipation rate decreases. This means that the helicity which was able to transfer to the writhing storage mode is stored in a quite stable way.

4.1.3 Comparison with the writhed case

In order to confirm the fact that the final helicity content indeed corresponds to a writhing content, the comparison is performed between both the writhed and the twisted configurations. Both helicity evolutions are depicted in Fig. 4.8.

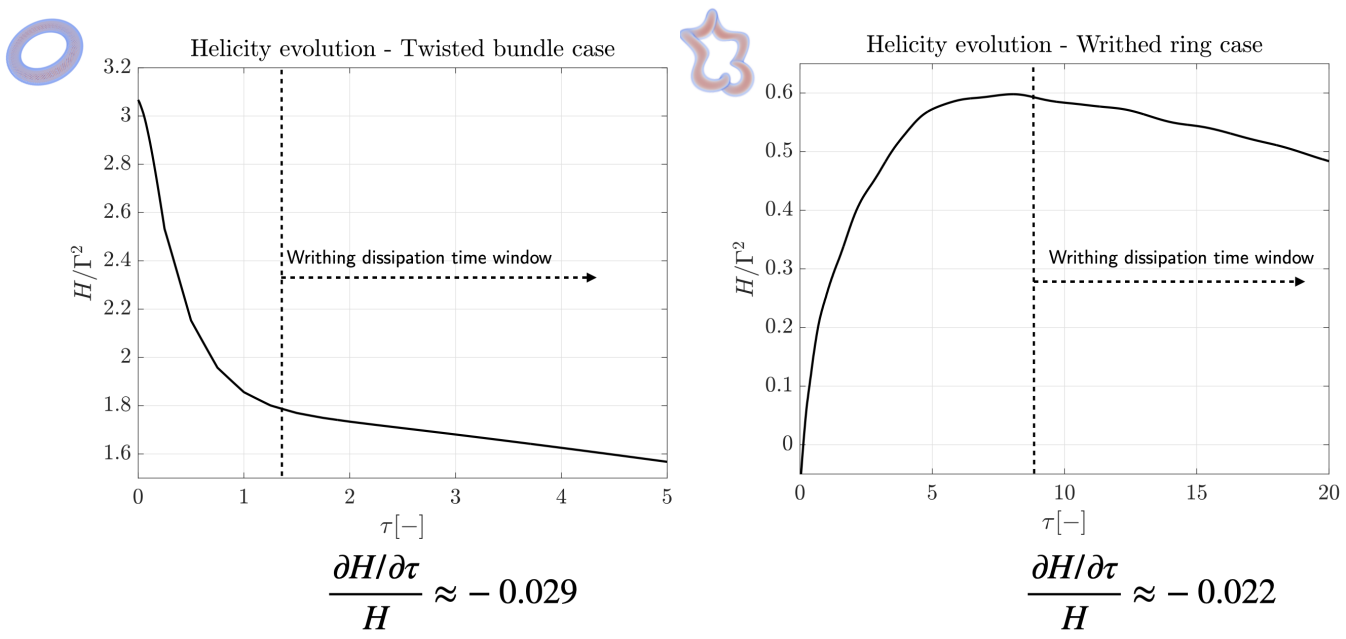

Figure 4.8: Comparison of the dissipation rate of the writhing content for both the twisting and the writhing configurations

The comparison between both dissipation rates reinforces the idea that, in both situations, the preferred helicity storage mode is the same, **writhing**, and that it would then be characterised by a particular dissipation rate. The latter assumption will be further verified in Chapter 5.

4.2 Continuous approach - Twisted fields

It is first mentioned that the reasonings and conclusions presented in this section have followed the investigation of another, more mathematical, approach of the helicity mystery, which is developed in Chapter 6 and is related to the knot theory.

The problem of an initially twisted field has already been studied in Section 4.1, and using a set of 49 vortex filaments to discretise the initial vorticity field. The present section uses a different initialisation. The goal here is to study the evolution of a continuously twisted ring, with its $\overrightarrow{\omega}$ field rotating on itself, as will be explained below. That way, an *intrinsic twist* will truly be put in the vortex tube as initial condition.

4.2.1 Case with planar centerline

Field initialisation

The first studied case of twisted field consists of a vortex ring, with a planar centerline, whose vorticity tube twists around the centerline n_{cycle} times, as would a twisted ribbon do (as described in Chapter 6). In that matter, and for each node of the vortex tube, the expression of a writhed

streamline is searched for, and the local vorticity vector is made tangent to it. This is depicted in Fig. 4.9, for three nodes belonging to the outer layer of the tube.

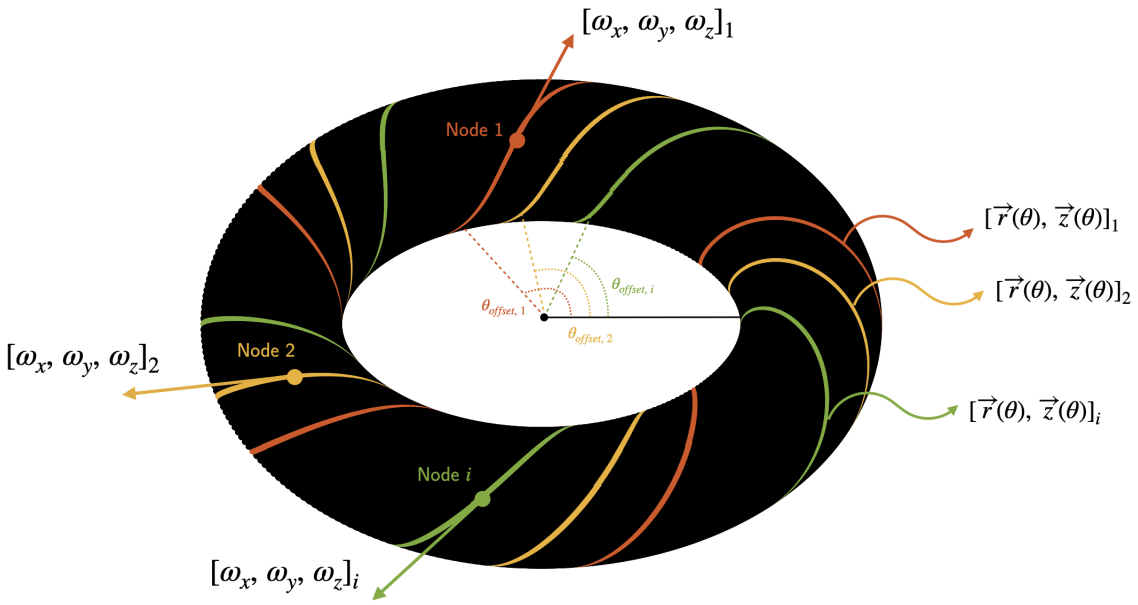

Figure 4.9: Initialisation of the local vorticity vector for three nodes belonging to the outer surface of the twisted ring. Nodes inside the tube (whose distance from the centerline is lower than σ_0) are initiated in the same way.

The main initialisation steps are described:

1. Choice of the number of cycles before field closure, n_{cycle}
2. Creation of the corresponding writhed streamline

   Then, **for each node belonging to the tube**

   (a) Adaptation of the amplitude of the writhed streamline to the distance of the node from the centerline, d_{CL}

   (b) Determination of the phase shift such that the writhed streamline intersects the node localisation

   (c) Determination of the direction of $\vec{\omega}$, tangent to the local writhed streamline, and such that $\sqrt{\omega_x^2 + \omega_y^2 + \omega_z^2} = |\vec{\omega}|$

In this regard, each of the writhed line determining the local orientation of the vorticity vector has the following mathematical description, for $\boldsymbol{\theta} = [0,\ 2\pi]$:

$$\begin{cases} \vec{r}(\boldsymbol{\theta}) = R + d_{CL} \cdot \sin(2\pi\ f\ R\,\boldsymbol{\theta}\ +\ \theta_{offset}) \\ \vec{z}(\boldsymbol{\theta}) = d_{CL} \cdot \sin(2\pi\ f\ R\,\boldsymbol{\theta}\ +\ \pi/2\ +\ \theta_{offset}) \end{cases}$$

With d_{CL} the distance between the considered node and the tube centerline ($0 \leq d_{CL} \leq \sigma_0$), f the frequency of field rotation, obtained as $f = \frac{n_{cycle}}{2\pi R}$ and θ_{offset} being the phase shift (obtained iteratively) applied to the writhed line in order for it to intersect the node location.

The obtained field for $n_{cycle} = 3$ is presented in Fig. 4.10, with, for each grid point, the plot of the direction of the $\overrightarrow{\omega}$ field. In Fig. 4.10, a double-cut is also shown displaying the local orientation of the field, and illustrating the rotation of it on itself. Furthermore, Fig. 4.11 compares the latter double-cut for $n_{cycle} = 1,\ 3$ and 5. All the configurations studied in this section are also run at $Re_\Gamma = 2000$.
It is finally pointed out that, in the context of the present chapter, the intensity of the twist of the tube will be described by the parameter n_{cycle}, whereas, in Chapter 6, this quantity is referred to as $\mathcal{N}$. Indeed, it will be explained that the twisting component of helicity, in the context of the knot theory, is an integer ($\mathcal{N}$) determined by the number of rotations that a structure operates around its centerline.

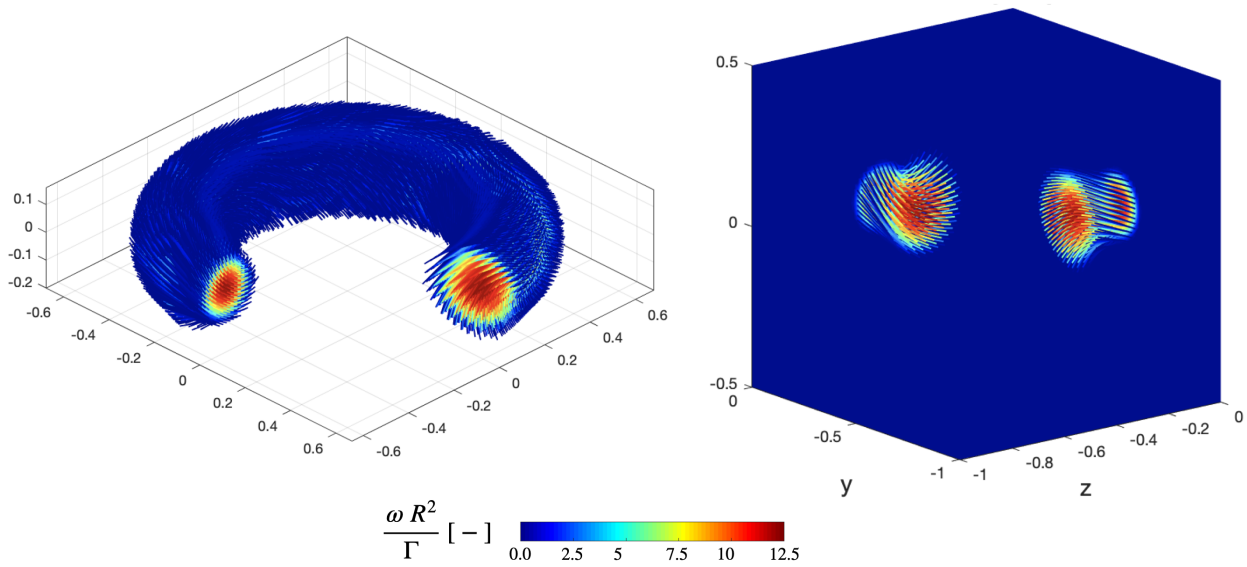

Figure 4.10: $\vec{\omega}$ field display with vorticity intensity and local field orientation, for $n_{cycle} = 3$

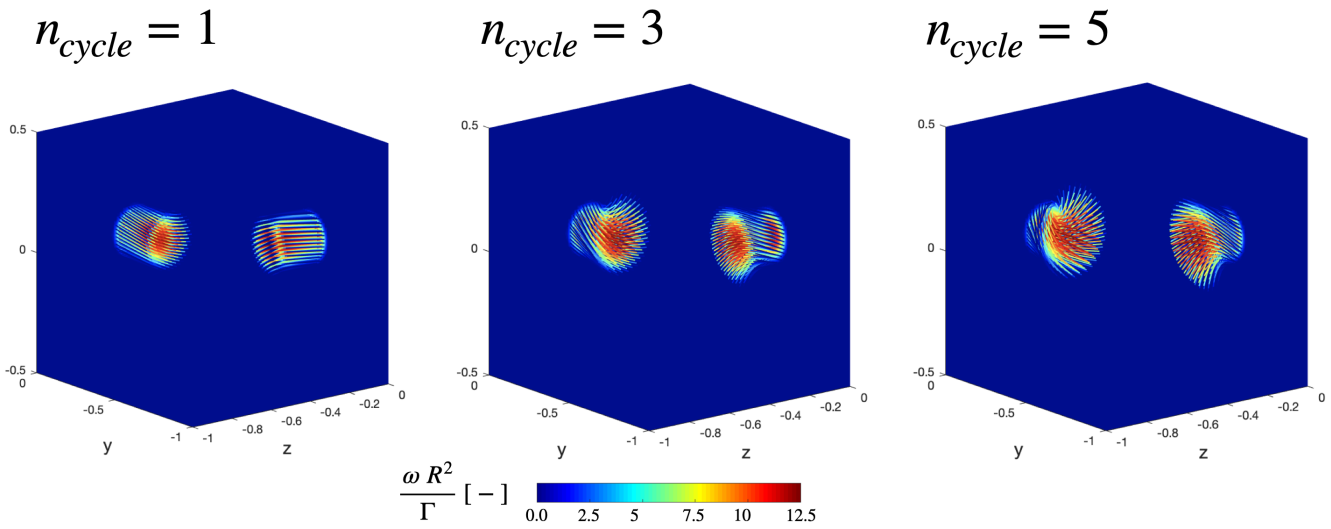

Figure 4.11: Comparison of the initialisation of the twisted fields for $n_{cycle} = 1,\ 3$ and 5

Study of the dynamics

The evolution of the double cut, displaying the intensity of the twist of each configuration, is depicted in Fig. 4.12, for $n_{cycle} = 5$ and has to be put in parallel with the evolution of the helicity content of the three configurations.

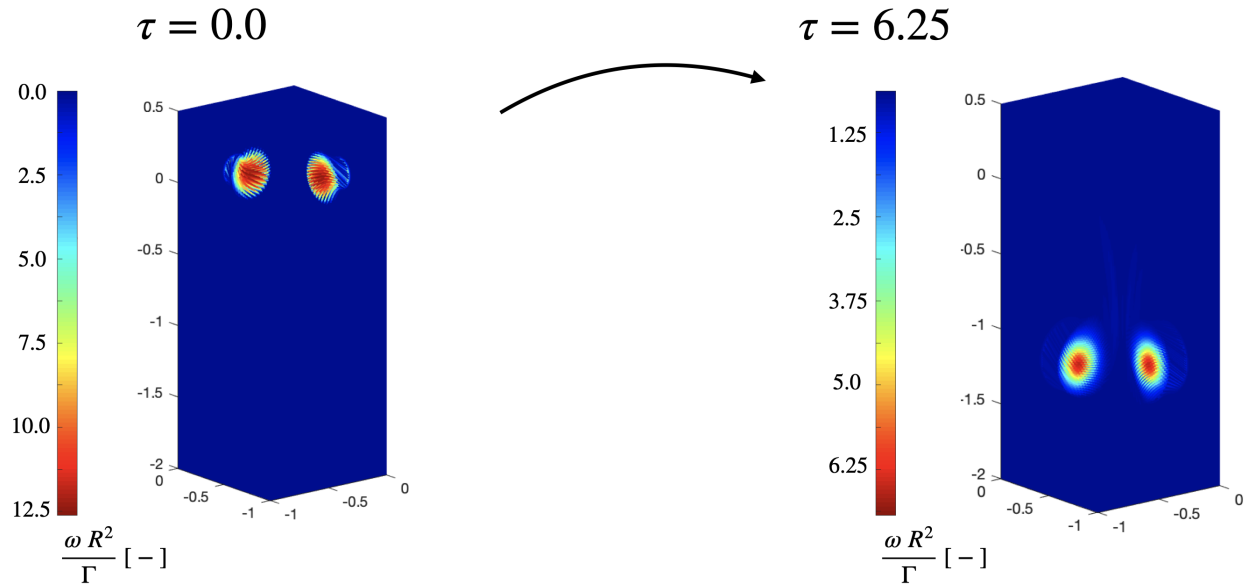

Figure 4.12: Evolution of the orientation of the vorticity field for the twisted ring, with planar centerline and with $n_{cycle} = 5$

From that picture, it may clearly be identified that the field undergoes a *detwisting* of its initially fully twisted structure. That topological change is identified to be one reason for the decrease in

helicity depicted in Fig. 4.13.

The initial helicity content is strictly due to the twisting of the $\overrightarrow{\omega}$ field, since, with a planar centerline, the latter may not confer any $\overrightarrow{u} \cdot \overrightarrow{\omega}$ value. Then, as was previously established and thus verified here, the twisting content quickly dissipates under the action of viscosity. This evolution is presented for n_{cycle} (or $\mathcal{N}$ when referring to Chapter 6) $= 1,\ 3$ and 5.

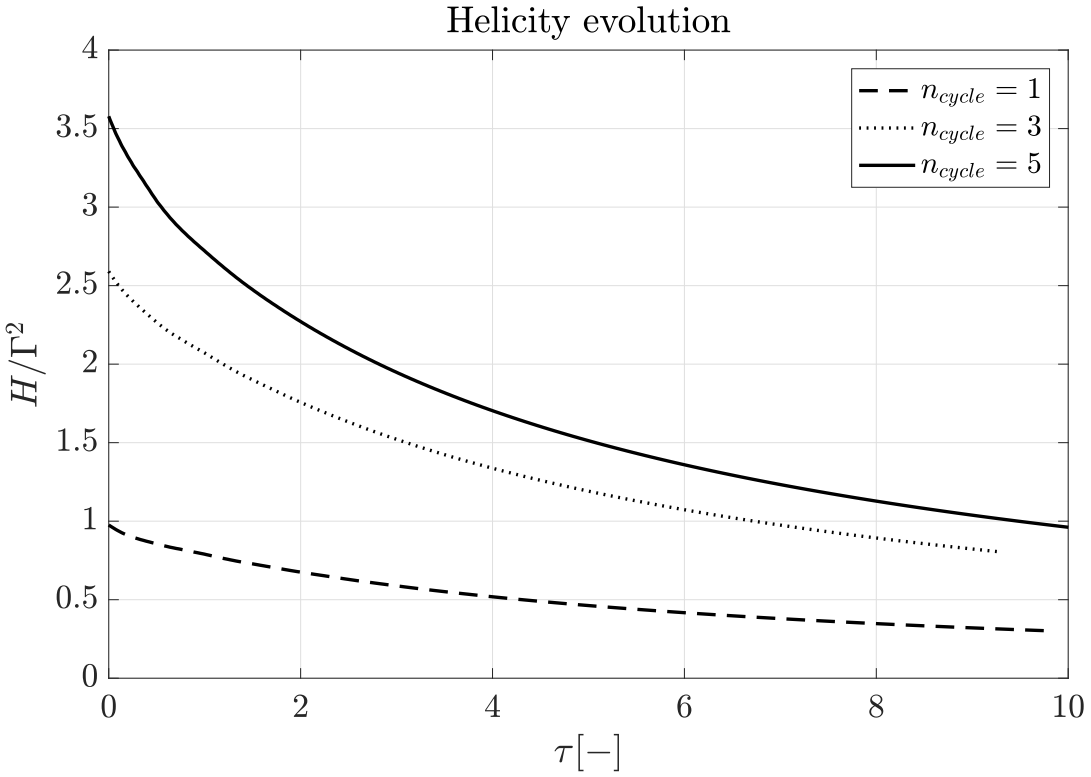

Figure 4.13: Evolution of the helicity content for the twisted configuration with planar centerline and with $n_{cycle} = 1,\ 3$ and 5

Finally, it is known ([4]) that the dissipation rate of the twist component of a twisted tube is given by

$$\frac{1}{Tw}\frac{\partial\, Tw}{\partial\, t} = -\frac{8\pi\ \nu}{A_{eff}} \tag{4.3}$$

Eq. (4.3) has enabled the determination of the evolution of the (effective) radius of the twisted tube. This is depicted in Fig. 4.14. It indeed confirms the double observation made here-above: the detwisting of the tube is accompanied by an enlargement of its cross section. The decay of the twisting helicity is due to both the detwisting of its structure and the growth of its vorticity support.

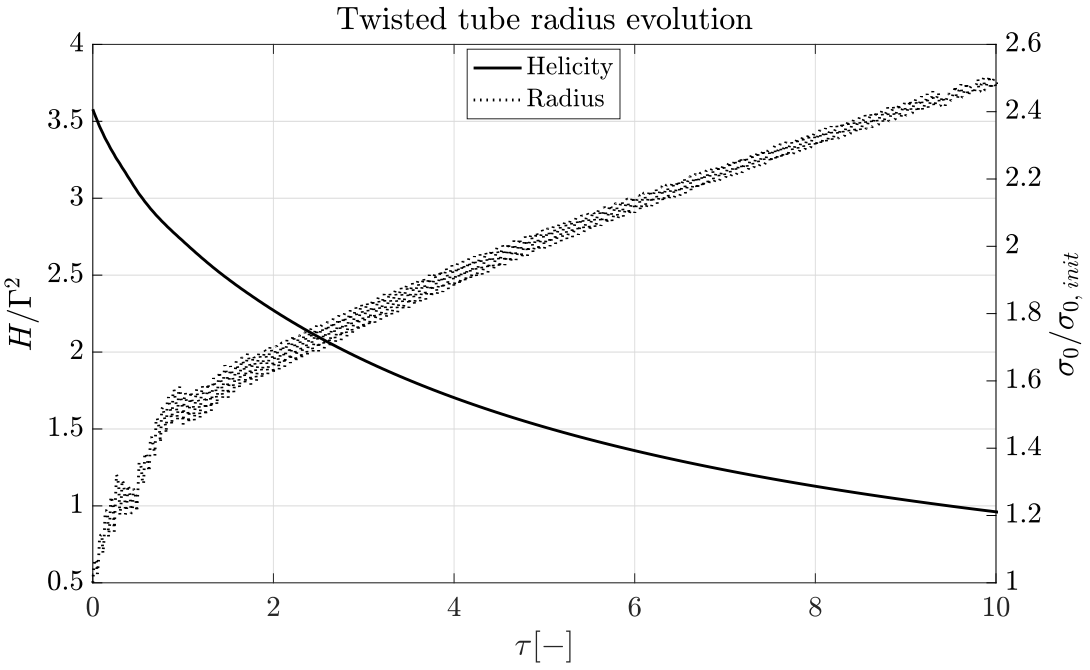

Figure 4.14: Evolution of the (effective) radius of the twisted tube, in parallel with the decay of its twisting helicity

Naturally, the question is raised whether the vortex tube had managed to operate a transfer from twisting to writhing, in that case. The centerline extraction tool has been used, in parallel with the knot theory formulas (see Chapter 6) to evaluate the amount of knottedness which appeared in that centerline. The latter remains planar during the whole evolution and no writhing content is created. This suggests that, in the absence of initial exploitable topology, no transfer is made possible towards a stable writhing content. This is further investigated in the following section, tackling the case of a twisted tube around a writhed centerline.

4.2.2 Case with writhed centerline

In order to carry on the study on the transfer between writhing and twisting, the implementation of a twisted tube with a writhed centerline has been performed. This follows the reflexion led in the chapter related to the knot theory (Chapter 6) and about the contributions within a ribbon. The present section thus aims at the initialisation of a vorticity field rotating on itself, thus with an intrinsic twist Tw and a writhed centerline, thus also a Wr initial contribution to its helicity content.

Field initialisation

Essentially the same methodology as for the case of the planar centerline is followed, i.e. **1)** the adaption of the amplitude of an oscillating geometry, both in radial and tangential directions, to the distance from the node to the centerline (for $0 \leq d_{CL} \leq \sigma_0$), **2)** the search for the phase shift of that oscillating line such that it intercepts the location of the node. However, now the centerline is also an oscillating line (or writhed line), around which the actual field is twisted. The initialisation

is depicted in Fig. 4.15 for 2 nodes (intercepted by the colored lines) rotating around the centerline (dashed black line).

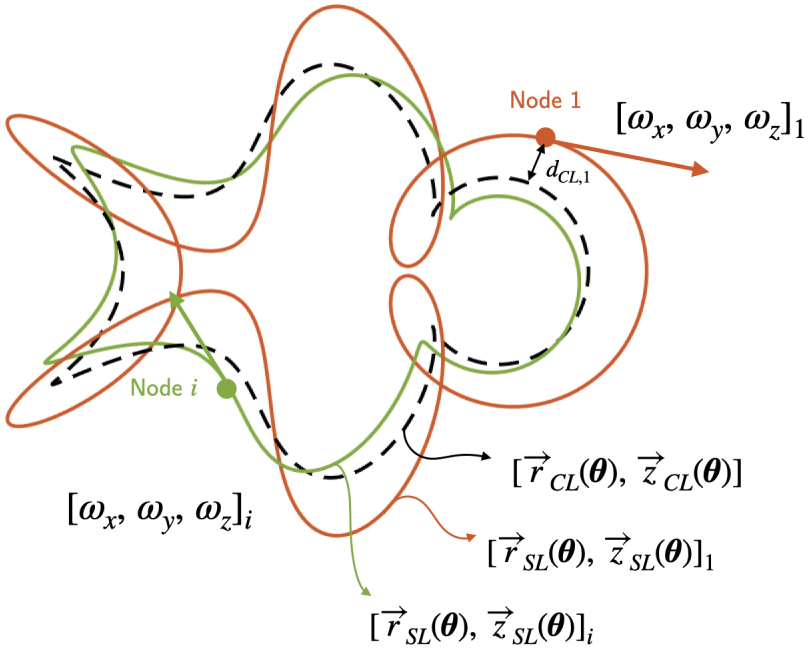

Figure 4.15: Initialisation of the local vorticity vector for two nodes of the writhed and twisted vortex ring thanks to tangent streamlines (colored lines) twisted around a writhed centerline (dashed, black)

Two frequencies of oscillations may thus now be chosen to determine the geometry: that of the centerline and that of the field around it. The centerline is described by the couple $[\vec{r}_{CL}(\boldsymbol{\theta}),\ \vec{z}_{CL}(\boldsymbol{\theta})]$, and the streamline tangent to the local vorticity vector is described by the couple $[\vec{r}_{SL}(\boldsymbol{\theta}),\ \vec{z}_{SL}(\boldsymbol{\theta})]$, for $\boldsymbol{\theta} = [0,\ 2\pi]$.

$$\begin{cases} \vec{r}_{CL}(\boldsymbol{\theta}) = R + \sigma_0 \cdot \sin(2\pi\ f_{CL}\ R\ \boldsymbol{\theta}) \\ \vec{z}_{CL}(\boldsymbol{\theta}) = \sigma_0 \cdot \sin(2\pi\ f_{CL}\ R\ \boldsymbol{\theta}\ +\ \pi/2) \end{cases}$$

$$\begin{cases} \vec{r}_{SL}(\boldsymbol{\theta}) = \vec{r}_{CL} + d_{CL} \cdot \sin(2\pi\ f_{SL}\ R\ \boldsymbol{\theta}\ +\ \theta_{offset}) \\ \vec{z}_{SL}(\boldsymbol{\theta}) = \vec{z}_{CL} + d_{CL} \cdot \sin(2\pi\ f_{SL}\ R\ \boldsymbol{\theta}\ +\ \pi/2\ +\ \theta_{offset}) \end{cases}$$

With $f_{CL} = \frac{n_{cycles,CL}}{2\pi R}$, $f_{SL} = \frac{n_{cycles,SL}}{2\pi R}$, $n_{cycles,CL}$ the number of oscillations of the centerline and $n_{cycles,SL}$ the number of times a line off the centerline rotates around it.

For the further investigations, $n_{cycles,CL}$ is fixed at 5, and $n_{cycles,SL}$ will be set at 1, 3 and 5. This is illustrated in Fig. 4.16 with a vortex line on the outer layer of the ring ($d_{CL} = \sigma_0$) highlighted in red.

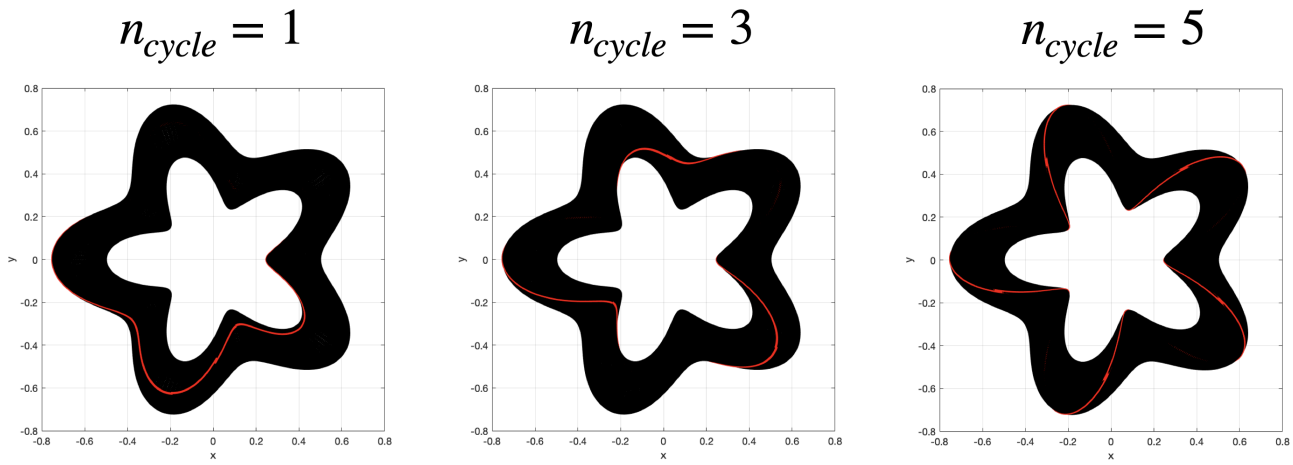

Figure 4.16: Three twisted fields around a writhed centerline, for $n_{cycles,SL} = 1,\ 3$ and 5

The initiation of the fields is shown in Fig. 4.17 with, for each node, the plot of the direction of the local vorticity vector.

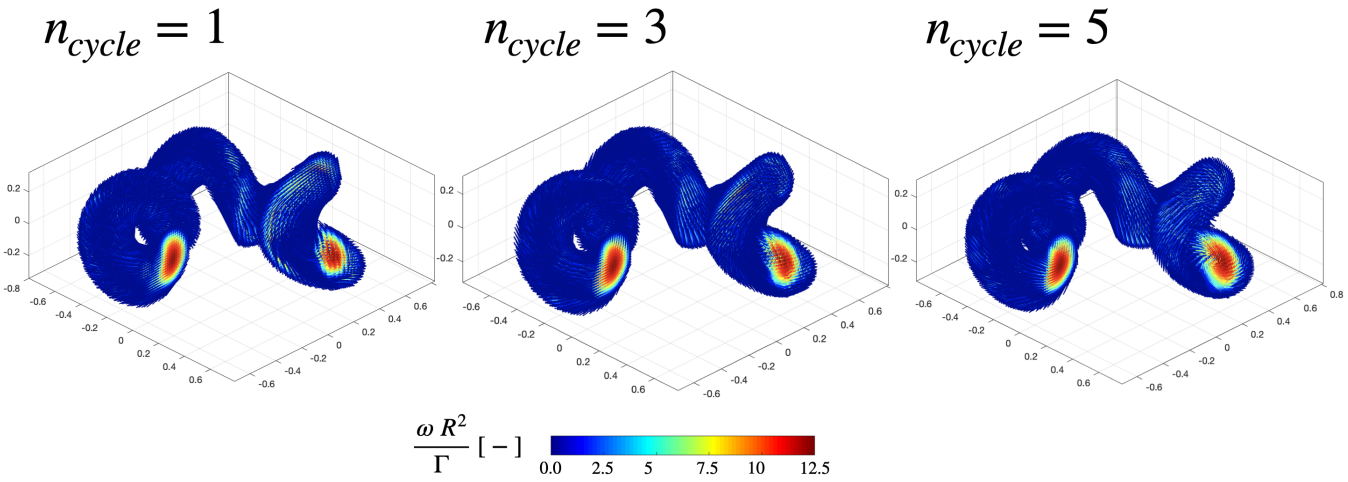

Figure 4.17: Fields for the twisted and writhed vortex ring

Study of the dynamics

The same phenomenon of field detwisting is expected to happen here, with the difference that the writhed topology may be conserved. This is indeed what occurs, as may be concluded by examining the helicity evolution depicted in Fig. 4.18.

The initial helicity content is due to both the fact that the centerline is writhed, and that the field is twisted around it, with a given intensity. That way, H_0 is different for each case, but it is observed that all three configurations tend to the same helicity decay, which is inevitably that of the writhing content, being the only common point between the three configurations. This once again confirms the hypothesis evoked in the other chapters: the twist component of the helicity decays rapidly, and the helicity content of a configuration tends to the writhing content.

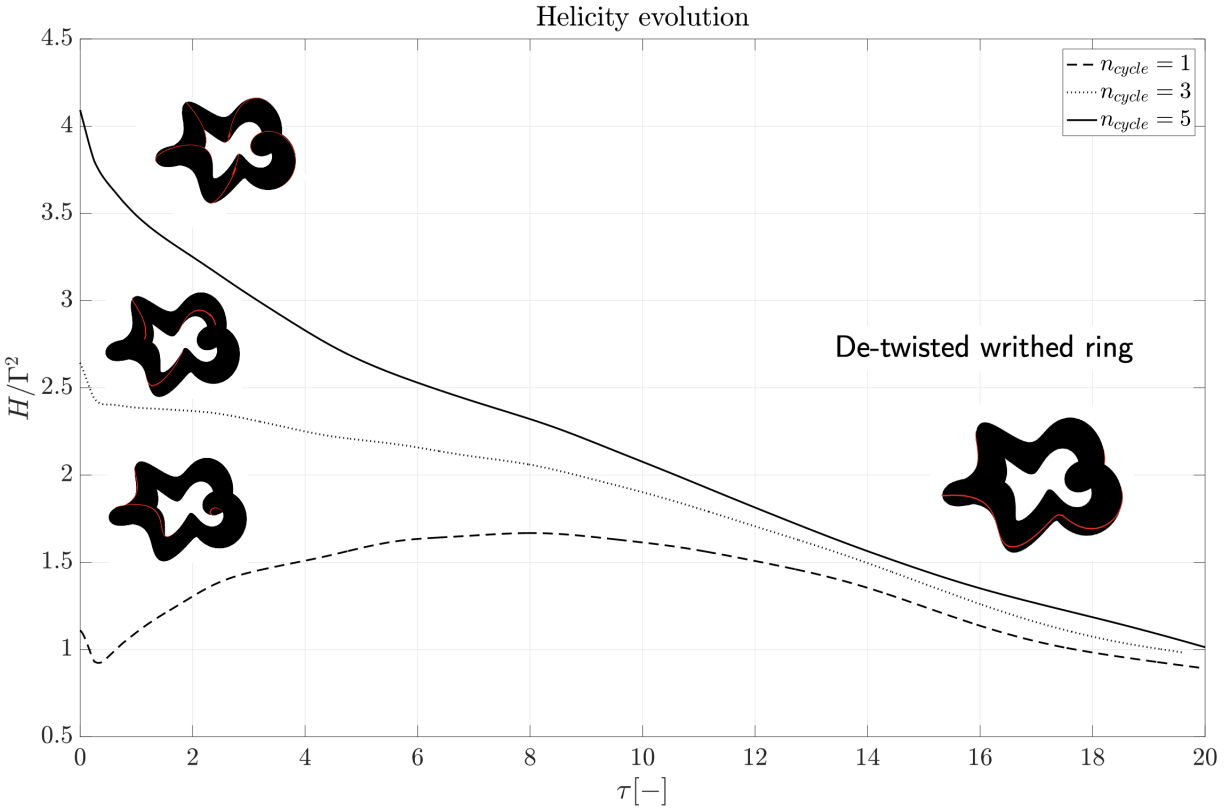

Figure 4.18: Evolution of the helicity content of the twisted field around a writhed centerline, for $n_{cycle} = 1,\ 3$ and 5

In view of the results presented in Fig. 4.18, the assumptions drawn in Section 4.2.1 may now be confirmed; for the case of the planar centerline, no topological mode where exploitable in order for the twisting to transfer its helicity content, whereas it is indeed the case for a writhed centerline. This is observed in Fig. 4.18: twisting does not only dissipates, making the global helicity content tend towards the writhing one. In fact, and thanks to the initially writhed centerline, twisting is able to **partially convert its content, creating that way some writhing**. Indeed, all three configurations only differ from their n_{cycle} number, and end up, when detwisted, on the same structure: that is a detwisted writhed ring.

Chapter 5

Characterisation of the transfer between helicity components

The present chapter aims to summarise and gather the conclusions obtained through the study of all helicity storage modes.

5.1 Helicity transfer

It has been observed that the helicity content of a configuration undergoes multiple transfer, with a general tendency to convert any form of *unstable* content into *stable* one. This has firstly been suspected based on purely topological observations, with the analysis of the evolution of centerlines, and further confirmed by analysing the helicity dissipation rates and comparing them. Indeed, the dissipation rates have been calculated for each of the following configurations: the twisted ring, the writhed ring, the knotted rings and the leapfrogging rings. The results are presented in Fig. 5.1. The rates have been computed on the time ranges where the configurations have already evolved until the presumed "writhing dissipation time range", i.e. the last decrease in helicity (yellow shaded area in Fig. 5.1). Each of those cases have run at $Re_\Gamma = 2000$.

As observed and predicted, those rates quite satisfyingly coincide:

$$\left.\frac{1}{H}\frac{\partial H}{\partial \tau}\right|_{writhed} = -0.022 \qquad \left.\frac{1}{H}\frac{\partial H}{\partial \tau}\right|_{twisted} = -0.029$$

$$\left.\frac{1}{H}\frac{\partial H}{\partial \tau}\right|_{leapfrog} = -0.020 \qquad \left.\frac{1}{H}\frac{\partial H}{\partial \tau}\right|_{knotted} = -0.027$$

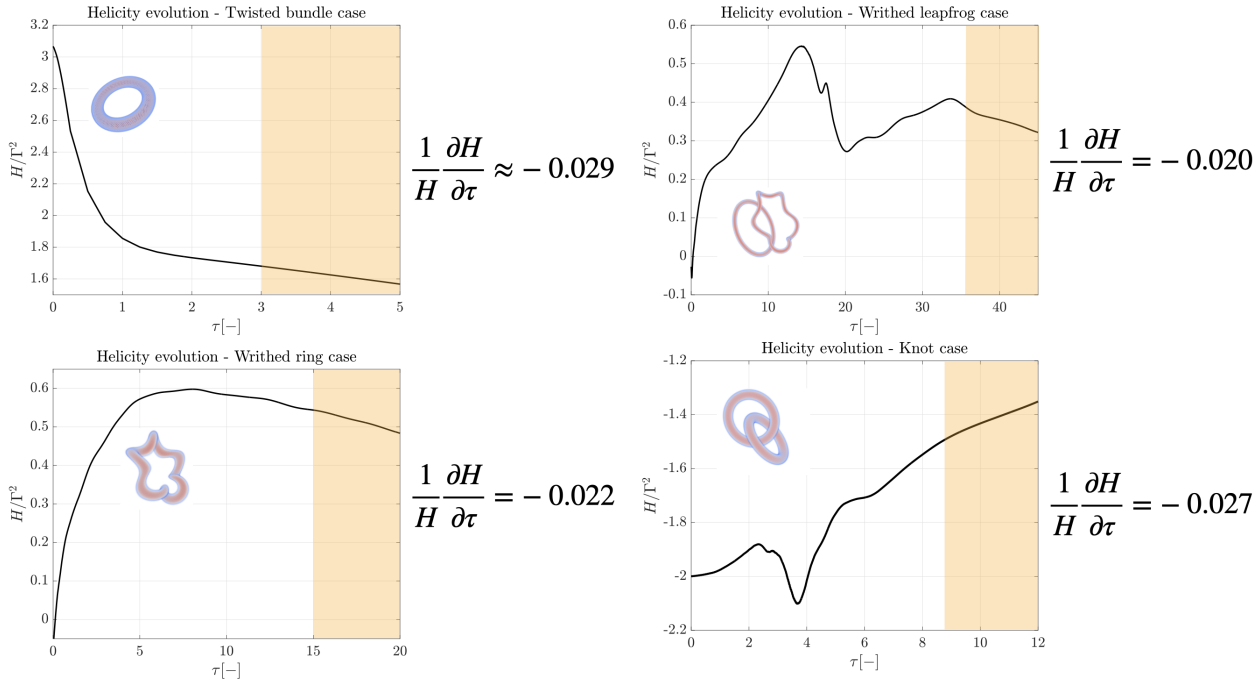

Figure 5.1: Comparison between the writhing dissipation rates for different ring configurations, at $Re_\Gamma = 2000$

That last dissipation have been identified to correspond to the one of the **writhing** storage mode. This helicity component has been studied on its own in Section 3.1, and suspected to protect helicity content from viscosity thanks to conservation of helical topology, which has been analysed with a centerline extraction method, developped in Appendix B, and mathematically characterised with tools from the knot theory, presented in Chapter 6. Besides, Scheeler and van Rees [4] [5] already emitted the idea that helicity could possibly be preserved thanks to the storage of it into writhing. This is thus partly verified here.

Furthermore, the flow of helicity content towards writhing is the result of multiple conversions of other modes. The linked configuration studied in Section 2.1 has unveiled the capacity of a pair of planar vortex rings to convert the biggest part of an initial **linking** content to a final writhing one, through some reconnection events. Section 4.1 also showed the instability of the intrinsic helicity content, making the global content tend towards the writhing one. That unstable mode has also been studied on its own in the case of a fully twisted field, in Section 4.2. The fast decay of that **twisting** component has here also been observed, at a rate of

$$\frac{1}{Tw}\frac{\partial Tw}{\partial t} = -\frac{8\pi\nu}{A_{eff}} \tag{5.1}$$

Yet, and contrarily to the writhed ring case, no conversion has been made possible in the purely twisted case. It is thus understood that, in order for the twisting component to transfer its content towards another mode, topological content must be available, as was the case for a writhed ring. In fact, as the purely twisted ring was provided with a planar centerline, the twisting component

had no other issue than dissipation. It is also observed that the decay of twisting depends on the global geometry of the tube (A_{eff} in Eq. (5.1)) and that the one of writhing does not. This is quite logical and coherent with the idea that the writhing content is only due to the vortex centerline topology, whereas twisting involves the whole tube.

The leapfrogging phenomenon described in Section 3.3 has enabled to further investigate the mechanisms of rings interactions responsible for the evolution of some helicity content. By allowing the interplay between a writhed ring and a planar one, a final reconnection has been obCălugăreanuserved. That resulted into a large writhed structure, whose helicity dissipation was once again found to be the one of the writhing helicity component.

However, such interaction or reconnection is not always made possible. Section 2.2 has had the goal to study the evolution of a knotted pair of rings, with different circulations. That difference in circulation was the reason for the inability for both rings to reconnect, making it impossible for the initial **linking** component to convert into any other helicity storage mode. A fast decay has thus been observed as soon as both rings interacted. Linking is thus identified to be an unstable helicity storage mode, on the same manner as **twisting**.

Yet, the question has also been raised whether helicity could be preserved in a viscous configuration or not. The answer seems to be nuanced, as viscosity always ends up destroying information, through the transfer of the TKE from scales to scales, up to the Kolmogorov one. For quite low Re_Γ configurations, it is thus stated that the helicity may be *badly* or *well* protected, and that some configurations are more eager to tend towards a *well-protected* configuration, transferring, when possible, initial helicity content to the **writhing helicity component**.

5.2 Helicity creation

Those different cases having been explored, the question has emerged whether or not this was possible to create some helicity content from an initially helicity-deprived configuration, through various interactions between rings and vorticity structures.

Indeed, all the previously analysed cases were concerning situations where an initial helicity content was already present, then made evolving. To further explore that idea of helicity creation, the following configurations have been implemented and observed:

- leapfrogging between two planar rings with different circulations
- collision between two planar rings with the same circulation
- collision between two planar rings with different circulations
- angular collision between two rings of same/different circulation and same/different size

Those trials all failed at producing any content of helicity through some interaction. Further research however explained the reason why such creation would not have been possible. Indeed, when considering the Călugăreanu theorem presented in Chapter 6, it is understood that, without the intervention of an external flow or structure, a field, divergence-free, with an initial Călugăreanu

number $n = 0$ (and not due to the compensation of two different helicity contributions) may not create some net helicity content. In fact, in any configuration where a creation of topological centerline helicity has been observed, this was caused by the decay of another present component. In the case where every component is initially set to zero, no source may thus feed the potential centerline contribution.

It is thus concluded that, in the absence of external forcing, it is not possible to create helicity from an helicity-deprived configuration.

Chapter 6

Helicity from the point of view of the knot theory

6.1 Introduction

Knot theory has been a playground for mathematicians for decades now, and is quite often used by fluid mechanicians, mostly when speaking about vortex lines, in order to purely describe the topology of a configuration.
Although the complexity of most developments found in the literature are clearly out of scope for the present work, many mathematical descriptions have been useful in order to understand the phenomena involved in the (partial) conservation of the helicity content of some configurations.

Thus, in the present chapter, several results from the knot theory are presented and linked with previously drawn conclusions. It is to be noticed that, when speaking about the knottedness of a vortex line, all fluid mechanic aspects are put aside, as the presented formulas strictly concern the topology of a curve, completely ignoring the fact that it is based on vorticity and velocity fields.

6.2 The Frenet-Serret equations

In order to describe a curve, its space characteristics and its degree of knottedness, the Frenet-Serret equations are of use.

A closed curve is considered, on which the curvature no where vanishes. For this curve C, the vector $\mathbf{s}$ describes the position of a point on C, and ξ corresponds to the arc-length. Based on Fig. 6.1, the following vectors are defined:

$$\frac{\partial \mathbf{s}}{\partial \xi} = \mathbf{t} \qquad \text{where } \mathbf{t} \text{ is the local tangent unit vector} \tag{6.1}$$

$$\frac{\partial \mathbf{t}}{\partial \xi} = c\mathbf{n} \qquad \text{where } \mathbf{n} \text{ is the local normal unit vector} \tag{6.2}$$

$$\frac{\partial \mathbf{n}}{\partial \xi} = -c\mathbf{t} + \tau\mathbf{b} \qquad \text{where } \mathbf{b} \text{ is the local binormal unit vector} \qquad \mathbf{b} = \mathbf{t} \times \mathbf{n} \tag{6.3}$$

$$\frac{\partial \mathbf{b}}{\partial \xi} = -\tau\mathbf{n} \qquad \text{where } c \text{ and } \tau \text{ are the local curvature and torsion of } C\text{, respectively} \tag{6.4}$$

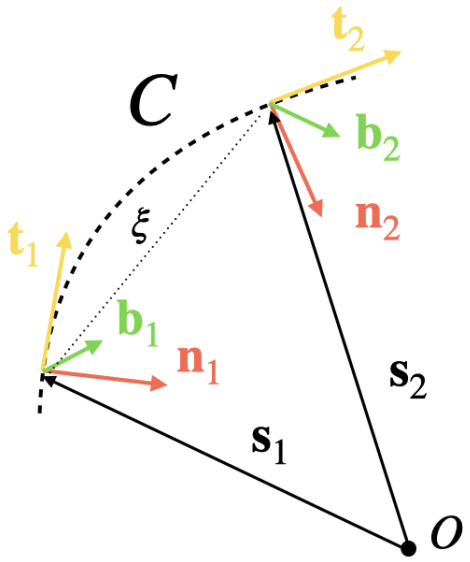

Figure 6.1: Vectors of interest for the Frenet-Serret equations

Those equations allow the definition of the **spanwise** vector $\mathbf{N}$

$$\mathbf{N} = \mathbf{n}\cos\theta + \mathbf{b}\sin\theta \tag{6.5}$$

Where θ is the local twist angle. The spanwise vector is a *twist describing* vector and may be associated to a twisted ribbon. It always points to the direction normal to the latter, as illustrated in Fig. 6.2 (for a particular ribbon, the Moebius one, closing after θ has gone from 0 to π).

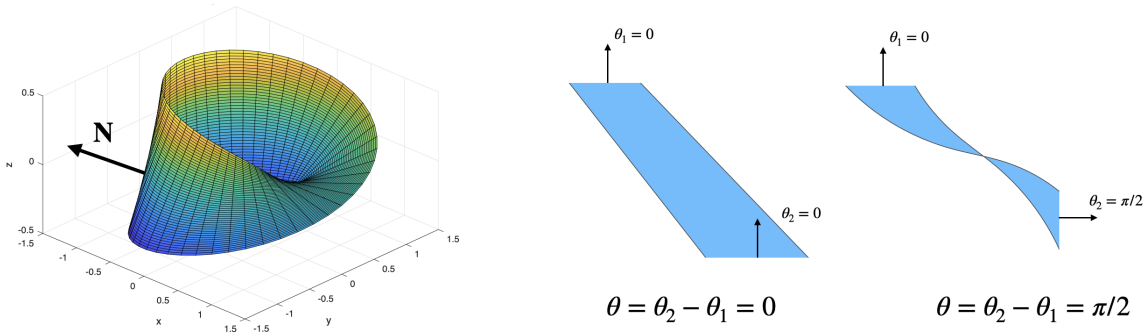

Figure 6.2: Local spanwise vector **N** on the Moebius ribbon, along with the illustration of the twist angle θ

It is thus furthermore possible to isolate the local curvature and torsion based on the Frenet-Serret equations

$$\tau = -\frac{\partial \mathbf{b}/\partial \xi}{\mathbf{n}} \qquad \text{and} \qquad c = -\frac{(\partial \mathbf{n}/\partial \xi - \tau \mathbf{b})}{\mathbf{t}} \tag{6.6}$$

Those local quantities are represented in Fig. 6.3 for the centerline of an already studied geometry.

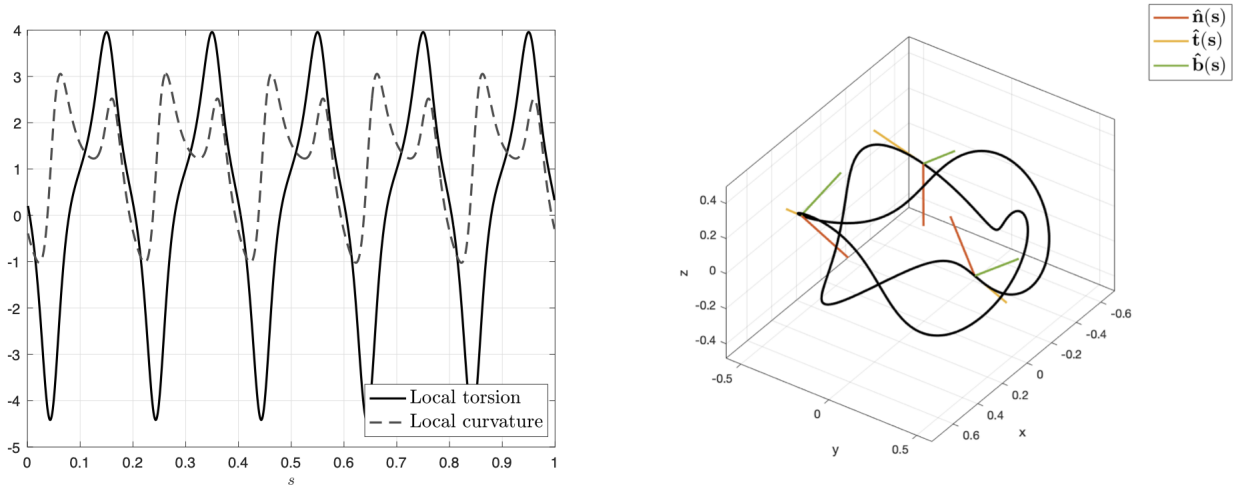

Figure 6.3: Local torsion and curvature evolutions along the s coordinate for the periodic knot with 2 turns

6.3 Mathematical descriptions

The same three contributions to the helicity as previously evoked are considered, i.e. linking, writhing and twisting. The purely topological description of them is here put in equations.

Linking

For contours put in a knot configuration, the helicity is expressed as [3]

$$Lk = \prod_{i \neq j} \Gamma_i \Gamma_j \frac{1}{4\pi} \sum_{i \neq j} \oint_{C_i} \oint_{C_j} \frac{(\mathbf{s}_i - \mathbf{s}_j) \cdot (\mathbf{ds}_i \times \mathbf{ds}_j)}{|\mathbf{s}_i - \mathbf{s}_j|^3} \tag{6.7}$$

Where the summation is performed on the different closed contours. Helmholtz [7] also described this contribution as being

$$Lk = 2n\Gamma_1\Gamma_2 \tag{6.8}$$

With Γ_i being the intensity of contour C_i and n the Gauss linking number. The latter has already been discussed in Section 2.1.

It is thus seen that Lk may only be an integer multiple of the product of the intensities. When talking about vortex rings and their vortex centerlines, the intensity is obviously the circulation of the ring.

Writhing

Considering a contour C, its writhing content is given by the following double contour integral ([1], [3], [11])

$$Wr = \Gamma^2 \frac{1}{4\pi} \oint_C \oint_C \frac{(\mathbf{s} - \mathbf{s}') \cdot (\mathbf{ds} \times \mathbf{ds}')}{|\mathbf{s} - \mathbf{s}'|^3} \tag{6.9}$$

In order to compare this purely topological point of view with the helicity values computed based on both $\overrightarrow{u}$ and $\overrightarrow{\omega}$ fields, the following method has been followed

1. Dump of the vorticity fields from `VPM`
2. Extraction of the vorticity centerline thanks to the tool presented in Appendix B
3. Creation of a *contour* object
4. Application of the knot theory formulas on that extracted contour, and comparison of both *fluid mechanics* and *topological* helicities

The results are quite satisfyingly close for most of the configurations, as shown in Tab. 6.1, except for one configuration, the writhed ring, which will be discussed later on. The *discrete geometry* cell refers to the input discrete geometry provided to `VPM` in order to initiate the vorticity of the particules at $\tau = 0$. The *centerline* cell corresponds to the extracted contour based on the $\overrightarrow{\omega}$ field.

Table 6.1: Comparison of the helicity contents from both topological and fluid mechanics points of view

	Planar ring	Writhed ring	Trefoil knot	Periodic knot, 2 cycles	Periodic knot, 3 cycles
$\frac{1}{\Gamma^2}\int_V \overrightarrow{u}\cdot\overrightarrow{\omega}\ dV$, on the computed fields	0.0	?	3.34	-5.79	-10.29
$\frac{1}{4\pi}\oint_C\oint_C \frac{(\mathbf{s}-\mathbf{s}')\cdot(\mathbf{ds}\times\mathbf{ds}')}{\lvert\mathbf{s}-\mathbf{s}'\rvert^3}$, on the discrete geometry	0.0	1.45	3.01	-5.69	-10.01
$\frac{1}{4\pi}\oint_C\oint_C \frac{(\mathbf{s}-\mathbf{s}')\cdot(\mathbf{ds}\times\mathbf{ds}')}{\lvert\mathbf{s}-\mathbf{s}'\rvert^3}$, on the extracted centerline	0.0	1.39	3.35	-5.81	-10.34

As was explained by Moffat and Ricca [9], "*if [...] the field is confined to a single knotted flux tube with intensity* Γ*, then the helicity is related to the topology of the knot [...]*":

$$H = \Gamma^2(Lk + Wr + Tw) \tag{6.10}$$

That way, the evolution of the helicity content based on a topological point of view has been compared to the one based on the velocity and vorticity fields, for the periodic knot configuration. At each timestep for which the fields have been dumped, the centerline has been extracted and the writhing content has been computed based on Eq. (6.9). This is represented in Fig. 6.4 for $0 \leq \tau \leq 2.5$.

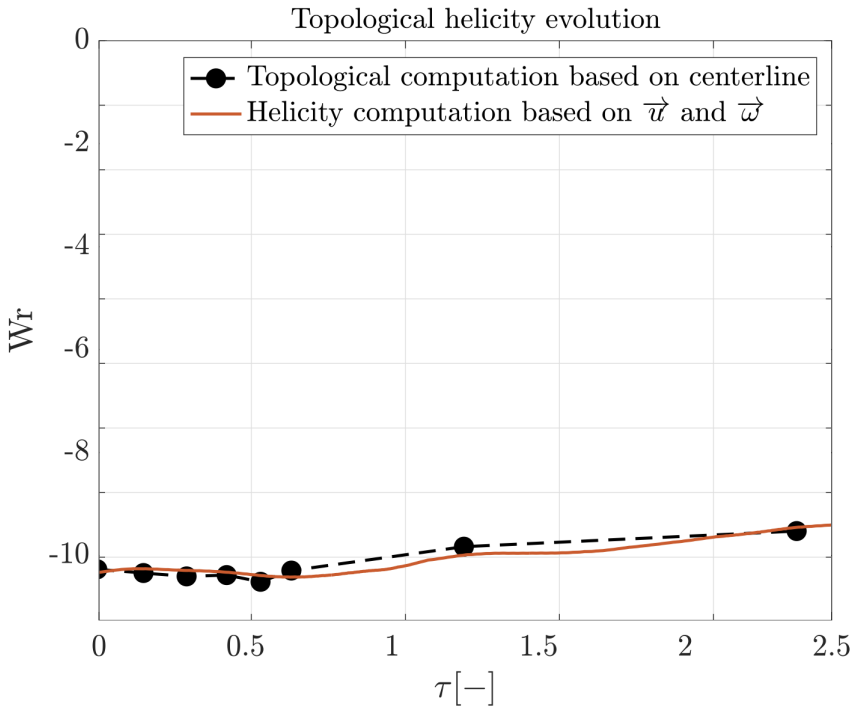

Figure 6.4: Comparison of both helicity contents (*fields* point of view and *topological* point of view) for the periodic knot ring with 2 cycles

The quite remarkable agreement between both computations enables to state that for such structures where the helicity is maintained for long time windows, this is due to a conservation of the topology of the knot, preventing viscosity from dissipating it. This picture agrees with the evolution of the geometry depicted in Fig. 6.5.

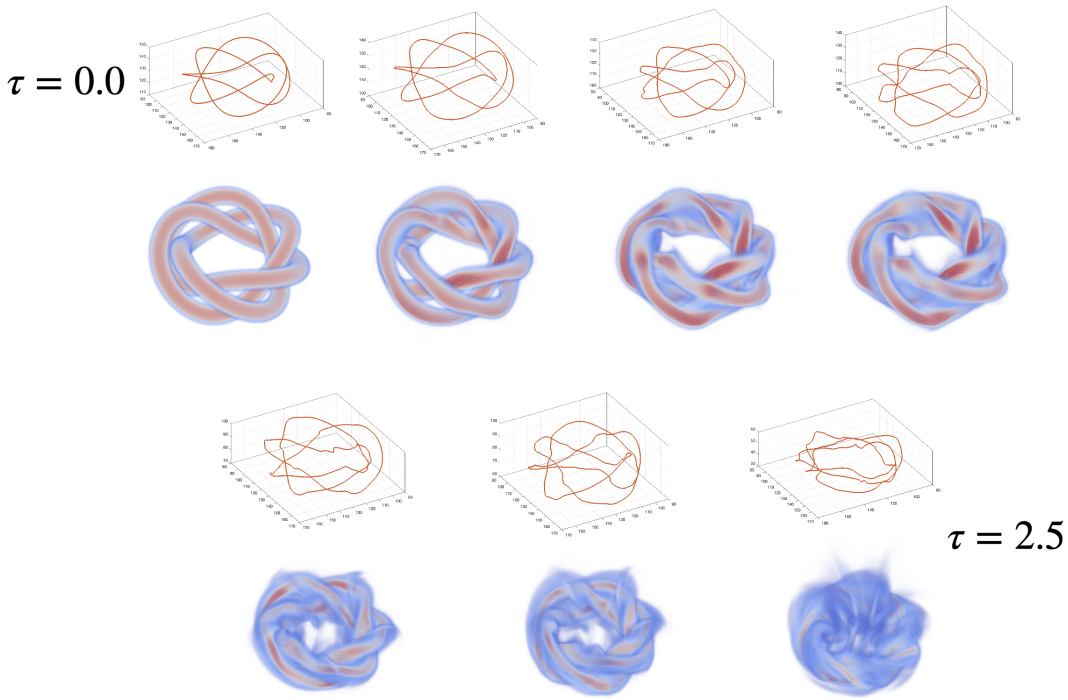

Figure 6.5: Time evolution of the geometry of the periodic knot along with its vortex centerline

The same methodology has been applied to the leapfrog configuration between a planar and a writhed ring. Thanks to the mask function presented in Appendix A, both $\overrightarrow{\omega}_1$ and $\overrightarrow{\omega}_2$ fields have been analysed separately. With the same procedure as for the periodic knot, the topological helicities of both rings have been plotted, aside with the evolution of the radius and of the mean curvature of the planar ring. Those results are presented in Fig. 6.6.

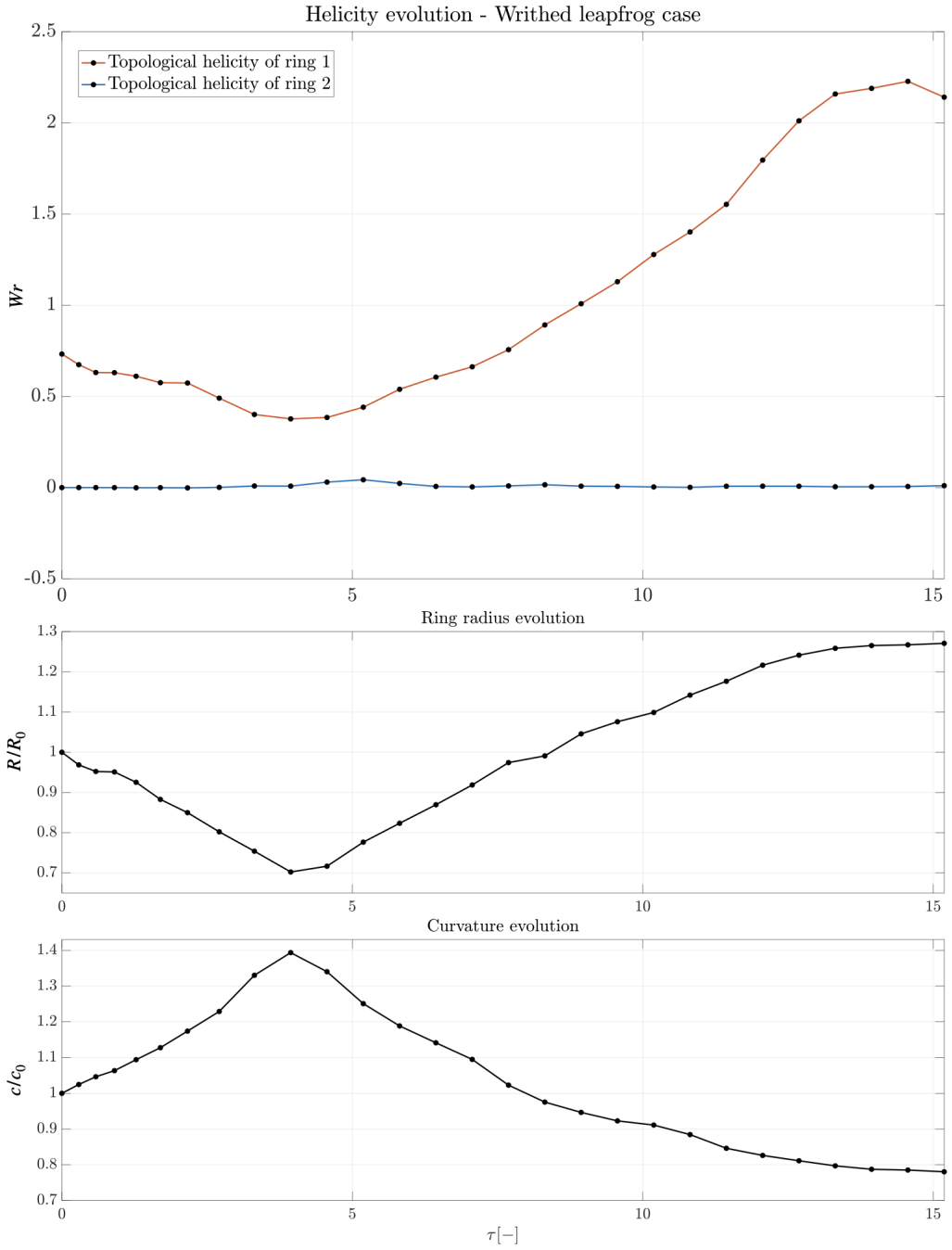

Figure 6.6: Evolution of the topological helicity of both rings involved in the leapfrog phenomenon

From it, it is concluded that the helicity content of the writhed ring does indeed decrease when it is extended by the passage of the planar ring inside of it. After that, its (topological) helicity content goes up as the ring compresses to go on the leapfrog phenomenon. These steps coincide well

with the evolution of the radius of the planar ring. The latter first compresses and then expands. Besides, the planar ring has initially no helicity (this was already shown previously), then creates some at $\tau \sim 5$, when the writhed ring enters its structure: the planar ring is slightly influenced by the writhed ring, conferring him a little bit of topological content. The suspicion of a potential transfer of writhing content from the writhed ring to the planar one may not be verified here after $\tau = 15$. Indeed, after the complex interaction between both rings, the mask function does not manage to separate the fields clearly anymore.

Concerning the writhed ring, the topological helicity of the configuration is presented in Fig. 6.7. At this stage, only $H_{topologic} = Wr = \frac{1}{4\pi} \oint_C \oint_C \frac{(\mathbf{s}-\mathbf{s}')\cdot(\mathbf{ds}\times\mathbf{ds}')}{|\mathbf{s}-\mathbf{s}'|^3}$ is considered.

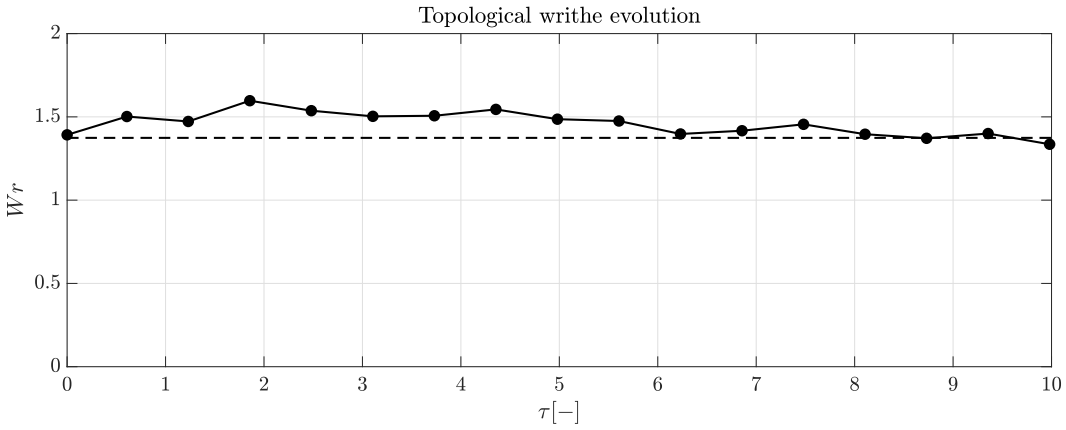

Figure 6.7: Evolution of the topological Wr helicity of the writhed ring (solid-dot) with the mean writhing content along the evolution (dash)

This again depicts the fact that the conservation of the topology of the ring allows for the conservation of an helicity content. However, as opposed to the other studied configurations, the content obtained by topology analysis and the helicity obtained based on $\overrightarrow{u}$ and $\overrightarrow{\omega}$ do not match. This suggests that the whole picture is in this case not shown by only considering the Wr contribution.

Indeed, the twisting computation must here be taken into account.

Twisting

It is first to be pointed out that talking about twisting does only make sense when considering at least two curves, or a bunch of some. In fact, a pair of curves is what is necessary to fully describe a **ribbon**. This particular geometry has been evoked when introducing the N spanwise vector earlier on.

The twisting of a structure is defined as

$$Tw = \frac{1}{2\pi} \oint_C \left(\mathbf{N} \times \frac{\partial \mathbf{N}}{\partial s} \right) \cdot d\mathbf{s} = \frac{1}{2\pi} \oint_C \left(\tau + \frac{\partial \theta}{\partial \xi} \right) d\xi \tag{6.11}$$

Where the spanwise vector is crossed with its variation along the contour. Eq. (6.11) may be split between two terms:

$$Tw = \mathcal{T} + \mathcal{N} = \underbrace{\frac{1}{2\pi}\oint_C \tau d\xi}_{torsion\ twist} + \underbrace{\frac{1}{2\pi}\oint_C d\theta}_{intrinsic\ twist} \tag{6.12}$$

When considering a ribbon (often used to define twist), the first term is relative to the torsion of the centerline of the latter ribbon, while the second term refers to the intrinsic twist of it. That second term is an integer, as it describes the number of turns the spanwise vectors does when travelling on the ribbon. For a one-sided ribbon, $\mathcal{N}$ is a multiple of π but not of 2π, as for two-sided ribbons (whose are described in the present chapter), $\mathcal{N}$ is a multiple of 2π. The torsion contribution may be seen as the integral under the torsion curve in Fig. 6.3 when considering the centerline of the ribbon.

In order to better depict those two contributions, two ribbons are described in Fig. 6.8. A ribbon is defined by two curves, C and C^*. In order to establish those curves, a centerline is first set (dotted-line). Then, both contour curves are added (solid lines). The ribbon is then described by the shaded area between those curves. The spanwise N vector is also represented along that area. For both of those ribbons, N performs 3 full rotations, thus $\mathcal{N} = 3$.

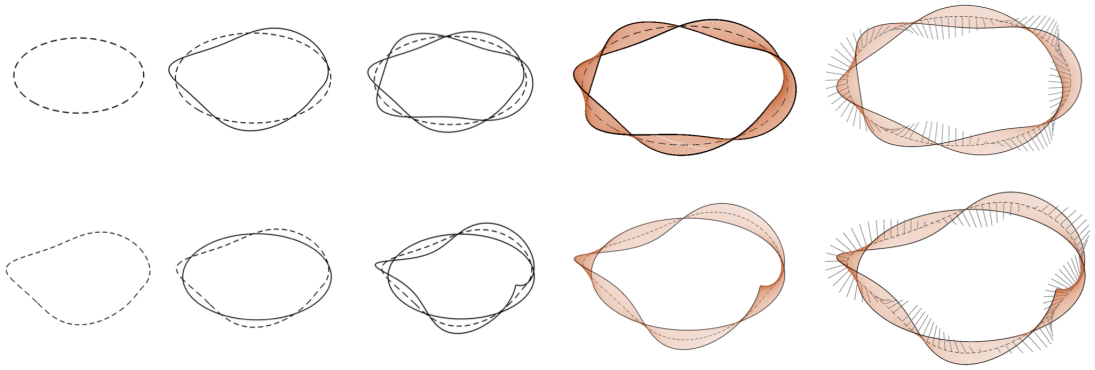

Figure 6.8: Implementation of two different ribbons

To further explore the contributions present in a ribbon structure, the Călugăreanu theorem is presented.

The Călugăreanu theorem

The Călugăreanu theorem is stated as follows:

For a ribbon delimited by two curves C and C^*, and under any isotopic continuous deformation,

$$n = Wr + Tw = Wr + \mathcal{T} + \mathcal{N} \qquad \text{is an invariant} \tag{6.13}$$

Also, the total helicity of the ribbon is then expressed as $H_{topologic} = \Gamma^2 n$.

For the two ribbons previously established, the different terms are computed:

Ribbon #1:

$$\mathcal{N} = 3 \qquad Tw = 2.993 \qquad \mathcal{T} \sim 0 \qquad Wr = Wr_1 + Wr_2 = 0.1142 + (-0.1142) = 0 \qquad \longrightarrow \qquad n = 3$$

As expected, the torsion part of the first ribbon is null. Its centerline is indeed planar. Both writhing contributions cancel out, leading to an helicity content only due to the intrinsic twist of the ribbon.

Ribbon #2:

$$\mathcal{N} = 3 \qquad Tw = 2.88 \qquad \mathcal{T} = -0.12 \qquad Wr = Wr_1 + Wr_2 = 0 + (-0.4027) = -0.4027 \qquad \longrightarrow \qquad n = 2.47$$

It is well verified that, for each ribbon, the identity $Tw = \mathcal{T} + \mathcal{N}$ is correct. Besides, the Călugăreanu number n is lower for the second ribbon. Those are thus not isotopic transformations of each other, but that is not the point here. For further precisions about isotopy classes, see [2].

Finally, considering a last ribbon (presented in Fig. 6.9) which could be compared, on a topological point of view, to the studied writhed ring of Section 3.1, the following values are obtained:

$$\mathcal{N} = 5 \qquad Tw = 3.44 \qquad \mathcal{T} = -1.45 \qquad Wr = Wr_1 + Wr_2 = -2.22 - 0.51 = -2.73 \qquad \longrightarrow \qquad n = 0.71$$

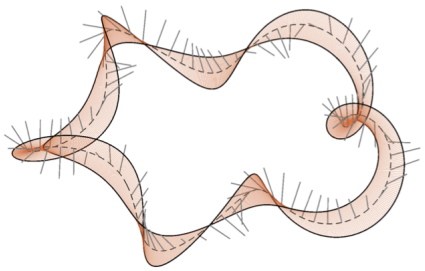

Figure 6.9: A ribbon with $\mathcal{N} = 5$, with a writhed centerline and two writhed delimiting curves C and C^*.

On this last example, it is observed that all contributions compensate to end up with a resulting Călugăreanu number wich is much lower than the ones previously obtained. This compensation of helicity contributions is the key to understand why the initial helicity content of the writhed ring configuration is not equal to the writhing content, and why it is nearly zero. What was first explained by comparing the results with the ones Scheeler obtained [4] can now be completely explained, component by component.

Although it is not possible to make a direct comparison between a ribbon provided with a circulation and a vortex ring, the latter developments show that it could be possible to initiate a ribbon whose helicity components would hardly compensate each others, as was obtained for the writhed ring in Section 3.1. It is finally illustrated that the detwisting of such a ribbon could only happen under the action of viscosity, as the transformation depicted in Fig. 6.10 is far from isotopic.

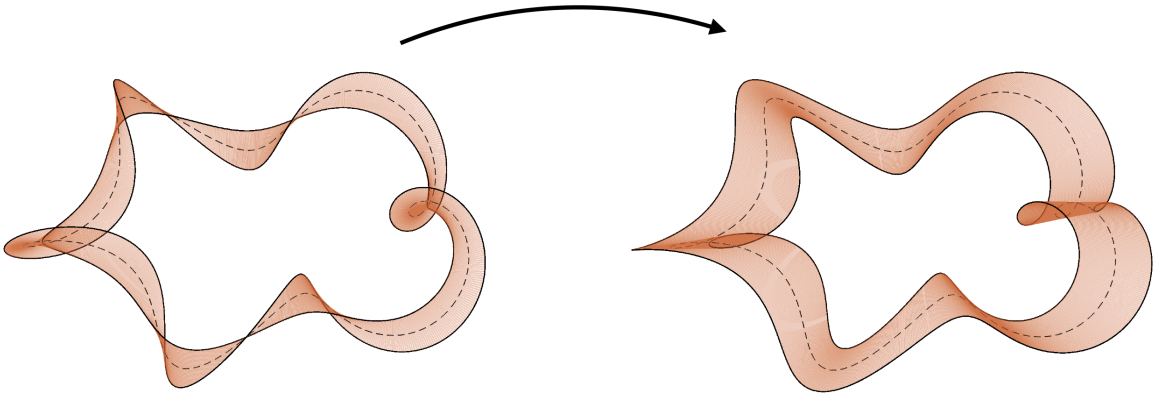

Figure 6.10: Detwisting of a ribbon, under the action of viscosity

6.4 Conclusion

The present chapter was intended to convey a more quantified description of the helicity content discussed in the previous chapters, by exploring formulas from the knot theory, describing the topology of contours and lines.
That study, coupled with the centerline extraction tool, has helped understanding more about the origins of the helicity content and to have a deeper insight of the mechanisms responsible for its partial conservation, or protection from viscosity. However, questions related to the transfer of it from mode to mode and ring to ring also require the taking into account of the fluid dynamics describing the interactions between vorticity structures, and not only the analysis of their vortex centerlines.

Chapter 7

Conclusion

The work performed in the context of this master's thesis is the result of several questionings which arose from the research made about the initial statement "*Study of the dynamics of vortex rings in a knot-type configuration*". That first investigation has allowed the discovery of numerous paths to explore, all of them concerning the helicity content in turbulent flows, and mainly in the context of vortex rings. That way, this work has aimed at the global tackling of the helicity content inside vortex rings arrangements and interactions between them. All of the sources composing the helicity have been explored through the discretisation of various structures, in the `VPM` research code, with the ultimate objective of being able to characterise the interactions between the different modes of the helicity content. Not only the transfer between those modes has been the focus of this work, but the main purpose has also been set to determine to what degree helicity was eager to be conserved, and by which means.

To some extent, those questions have been answered. But it is of major importance to identify the limits of the present methodology and results. Firstly, the mask function developed for fields separation purposes is questionable. Indeed, the diffusion of it is, at this stage, only ensured by the subgrid-scale model, which limits its use to applications where the fields do not interact in a too complex way. Yet, numerous results have been extracted thanks to it, whose may be trusted.

Also, it is quite evident that still a part of the obtained results may vary when increasing the grid resolution, and, more generally, be sensitive to numerical parameters. The simulations performed for this work were numerous, and also limited by resources management. A short numerical study has been undertaken, with the help of my supervisors, with the objective to investigate the effects of the subgrid-scale modeling, the reprojection step, the remeshing step and the grid resolution on the results for the helicity evolution of the knot-type configuration. This has led to the selection of a "numerical setup" to work with for the other simulations, consisting of a reasonable trade-off for computanional costs and allowing to have limited variations induced by the numerical setup.

In a general way, the subject of the research undertaken has been highly entertaining to work on, as constituting a completely new field of knowledge for me. I personally learned to try going further in the reasonings I led, and to ask myself appropriate questions, while attempting to discern pertinent information from irrelevant results.

Appendix A

Mask function implementation

As evoked previously, the isolation of the different components of the helicity have been performed through the implementation of a mask function on the vorticity field. This section aims at describing its development and functioning.

It is first reminded that helicity may be viewed as composed of mutual and individual contributions (referring to Fig. A.1):

$$H = \int_V \vec{u} \cdot \vec{\omega} \, dV = \underbrace{Linking}_{Mutual} + \underbrace{Writhing \; + \; Twisting}_{Individual} \tag{A.1}$$

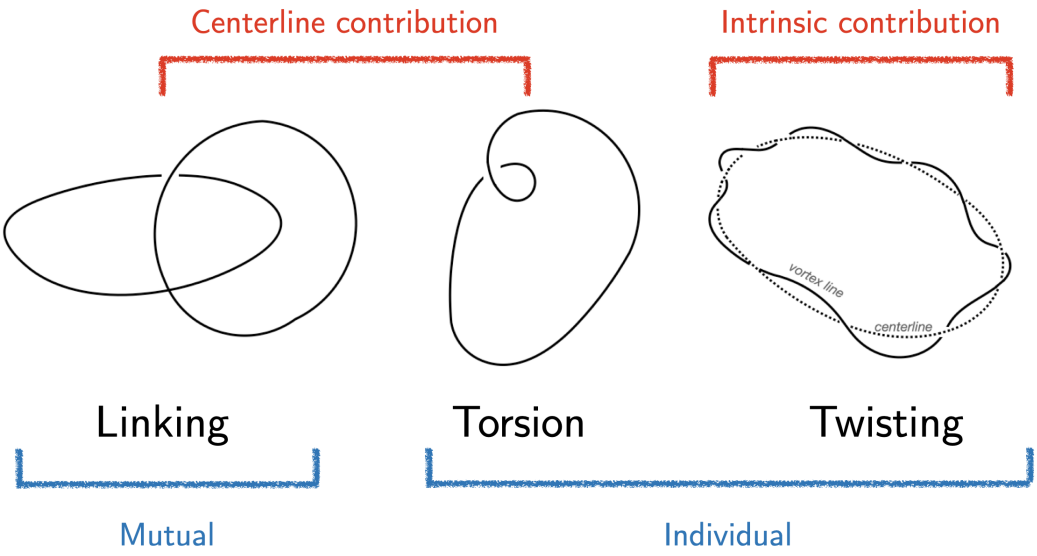

Figure A.1: Schematical representation of the three helicity components

Thereby, the linking component consists of the effect of velocity of the $ring_1$ on the vorticity of the

$ring_2$, and vice-versa. In other words:

$$H_{link} = \int_V \overrightarrow{u_1} \cdot \overrightarrow{\omega_2}\, dV + \int_V \overrightarrow{u_2} \cdot \overrightarrow{\omega_1}\, dV = 2 \int_V \overrightarrow{u_1} \cdot \overrightarrow{\omega_2}\, dV \tag{A.2}$$

To isolate this component, a mask function was necessary in order to apply, afterwards, an heavyside function on the vorticity field, in a way to distinguish the vorticity fields of both rings. This has been performed by the addition of 2 fields to the vorticity vector of the particles (as illustrated in Fig. A.2):

$$\omega_p = [\omega_x, \omega_y, \omega_z, \psi_1, \psi_2] \tag{A.3}$$

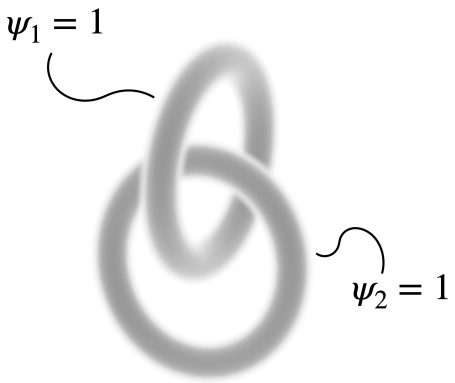

Figure A.2: Initiation of the masks based on the vorticity field

Where the subscripts 1 and 2 refer to both of the rings. The initiation ($\tau = 0$) of those scalar fields is thus performed in parallel to the one of the vorticities, i.e. on geometrical criteria. Then, the advection of the initial field is ensured by the transport of the particles.

The diffusion of the field could have been considered thanks to the addition of a RHS to the NS-equations:

$$\frac{D\,\psi}{D\,t} = \nu \nabla^2 \psi \tag{A.4}$$

and a Laplacian discretisation with a 4^{th} order finite differences:

$$\begin{aligned}
\nabla^2\psi \cong\ & \frac{1}{12(\Delta x)^2} \cdot \Big(16\left[\psi(x+\Delta x, y, z) + \psi(x-\Delta x, y, z)\right] - 30\left[\psi(x, y, z)\right] - \left[\psi(x+2\Delta x, y, z) + \psi(x-2\Delta x, y, z)\right]\Big) \\
& + \frac{1}{12(\Delta y)^2} \cdot \Big(16\left[\psi(x, y+\Delta y, z) + \psi(x, y-\Delta y, z)\right] - 30\left[\psi(x, y, z)\right] - \left[\psi(x, y+2\Delta y, z) + \psi(x, y-2\Delta y, z)\right]\Big) \\
& + \frac{1}{12(\Delta z)^2} \cdot \Big(16\left[\psi(x, y, z+\Delta z) + \psi(x, y, z-\Delta z)\right] - 30\left[\psi(x, y, z)\right] - \left[\psi(x, y, z+2\Delta z) + \psi(x, y, z-2\Delta z)\right]\Big)
\end{aligned}$$

However, the addition of such a RHS is not necessary, as the scalar field ψ already diffuses with the subgrid-scale model, as shown in Fig. A.3. Indeed, at $\tau = 0$, the field is well set to a binary value; 1 where vorticity takes a value, and 0 elsewhere.

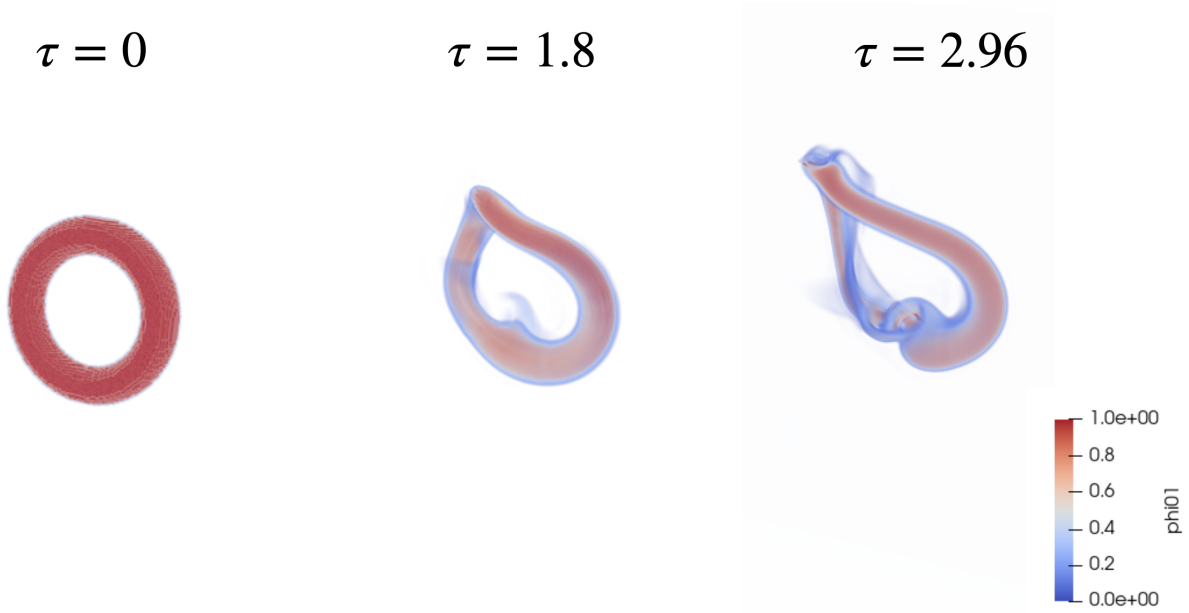

Figure A.3: Diffusion of the ψ field by the subgrid-scale model

Then, the action of time-integrating the NS-equations is performed by the `VPM` solver, considering the whole $\boldsymbol{\omega}$ vector; hence, the addition of a scalar field will not interfere with that.
A strength is thus added to the particles, related to the ψ field:

$$\alpha_{\psi,p} = \int_{V_p} \psi \, d\mathbf{x} \equiv \psi \cdot V_p \tag{A.5}$$

As is done for the vorticity field, the interpolation from the mesh to the particles is ensured by the M_4' scheme:

$$P2M: \qquad \psi(\mathbf{x}) = \sum_p \frac{\alpha_{\psi,p}}{h^3} M_4' \left(\frac{\mathbf{x} - \mathbf{x_p}}{h} \right) \tag{A.6}$$

$$M2P: \qquad \alpha_{\psi,p} = \sum_{\mathbf{x}} h^3 \psi(\mathbf{x}) M_4' \left(\frac{\mathbf{x} - \mathbf{x_p}}{h} \right) \tag{A.7}$$

The temporal update of ψ on the particules (after $M2P$) may be ensured by the low storage Runge Kutta 3 scheme. If the problem had been too stiff, as it was for the case of the temperature (Salerno's master's thesis, 2017 [12], from which most of the ideas of this appendix are drawn), the use of Euler implicit for the integration of the LHS of Eq. (A.4) should have been privileged:

$$\frac{\psi^{n+1} - \psi^n}{\Delta t} = \nu \nabla^2 \psi^{n+1} \tag{A.8}$$

With a Helmholtz equation considering $\Delta\psi^n = \psi^{n+1} - \psi^n$:

$$\frac{\Delta\psi^n}{\Delta t} = \nu\nabla^2(\Delta\psi^n) + \nu\nabla^2\psi^n \qquad \Longleftrightarrow \qquad \nabla^2(\Delta\psi^n) - \frac{1}{\nu\Delta t}\Delta\psi^n = -\nabla^2\psi^n \tag{A.9}$$

Which should have been solved for ΔT^n using Fast Fourier Transform.
The present added scalar field not variating to fast, the RK3 scheme is able to time-update it in a stable way.

The isolation of both $\boldsymbol{\omega}_1$ and $\boldsymbol{\omega}_2$ fields is then done by applying an heavyside function based on the value of ψ_1 and ψ_2 respectively. Both $\mathbf{v}_1$ and $\mathbf{v}_2$ fields based on the vorticity ones are obtained thanks to the vorticity-induced velocity law of Biot-Savart.

Due to the (highly turbulent) interaction between both rings, and the diffusion of the mask field, some particles sometimes take values for both mask fields. For those cases, a weighting is applied to distribute the total strength between both ω_1 and ω_2 components. Thus, for the particle i:

$$\omega_{1,i} = \frac{\psi_{1,i}}{\psi_{1,i} + \psi_{2,i}}\omega_i \qquad\qquad \omega_{2,i} = \frac{\psi_{2,i}}{\psi_{1,i} + \psi_{2,i}}\omega_i$$

Appendix B

Vortex centerline extraction tool

Motivation

The vortex centerline of a vorticity tube describes the topology of the latter, and thus enables the isolation of intrinsic phenomena from purely geometrical contributions to, for example, the helicity of a configuration. When studying helicity, this is of high relevancy, as helicity content itself may be split into two centerline contributions, writhing and linking, and a bulk contribution, or intrinsic helicity, twisting, which does not depend on the way the centerline(s) fold(s) on itself (theirselves), but how different streamlines inside a tube interact.

The establishment of a method to extract the centerline of a field, in those cases a vorticity field, will thus allow: firstly to discern centerline to bulk helicity, and secondly, with the help of the knot theory (see Chapter 6), to study the effect of the topology on the conservation of, or transfer inside, the helicity content.

Methodology

Any fluid dynamic notion is here put appart, as only a set of vertices with vectors of given orientation is considered. The extraction of the centerline, being a subset of the entire set of vertices (the grid points of the domain), is performed from a starting point x_{start}. For the case of a vortex tube, the starting point, at each timestep, is chosen to be the node with the highest value of $|\omega|$.

Based on the vertice i, the vertice $i+1$ is found by expanding a segment of length Δx in the direction tangent to the vorticity at the vertice i. The value of Δx is chosen but still limited by the resolution of the mesh used for the simulation.

If the vorticity field over the domain had been perfectly divergence free at each timestep, and depending on the Δx chosen, the streamline would have closed on itself perfectly. However, due to the reprojection being only performed each 20 timesteps, and to the complexity of the configuration increasing as the simulation evolves, this was not the case. In order to close each vortex centerline object, a precision requirement Δx_{max} is used. That way, as soon as the distance between vertice 1 and vertice n is lower than Δx_{max}, the line is closed by a last segment.

Appendix C

Detailed view of the interaction zone for the knot-type configuration

The present appendix aims at the description of the zones of high interaction between both rings involved in the evolution of the knot-type configuration.

An adaptative cut is thus performed at each timestep described hereunder, in order to place it in the interaction zone. A first global cut is first shown, followed by a close cut in the area of interest as well as a description of the localisation of the latter cut.

Figure C.1: Detailed interaction zones for the knot-type configuration

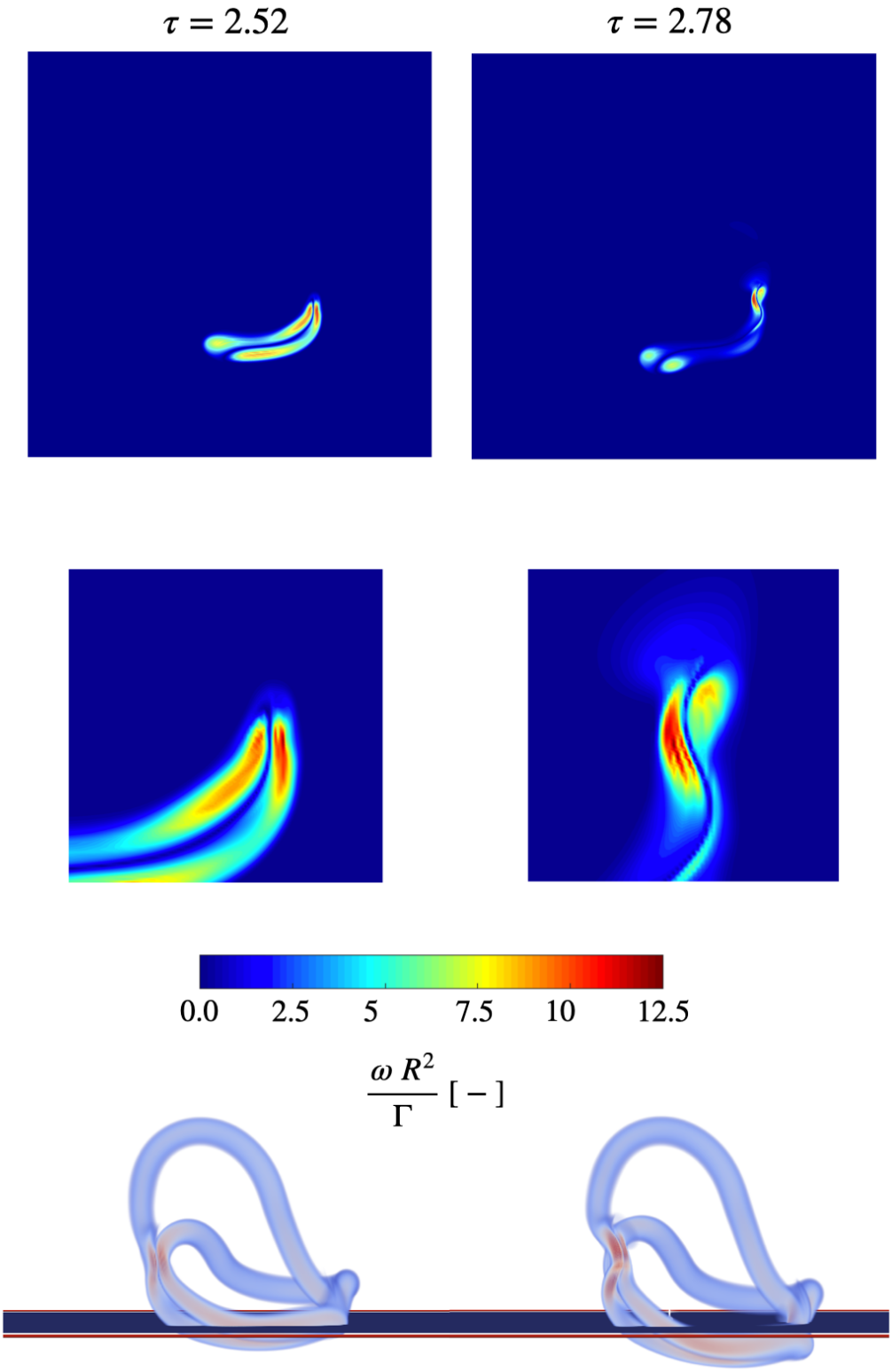

Figure C.2: Detailed interaction zones for the knot-type configuration

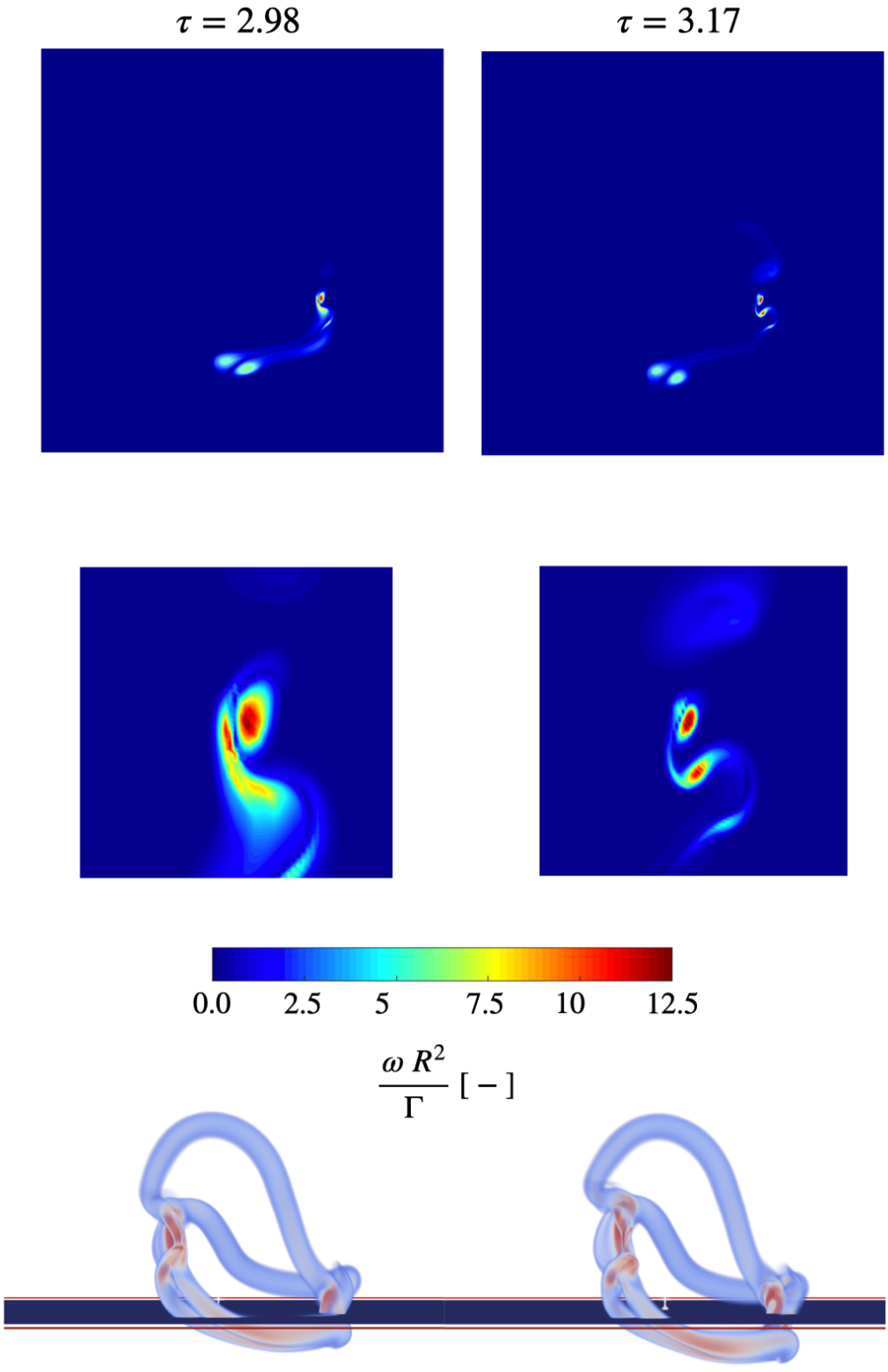

Figure C.3: Detailed interaction zones for the knot-type configuration

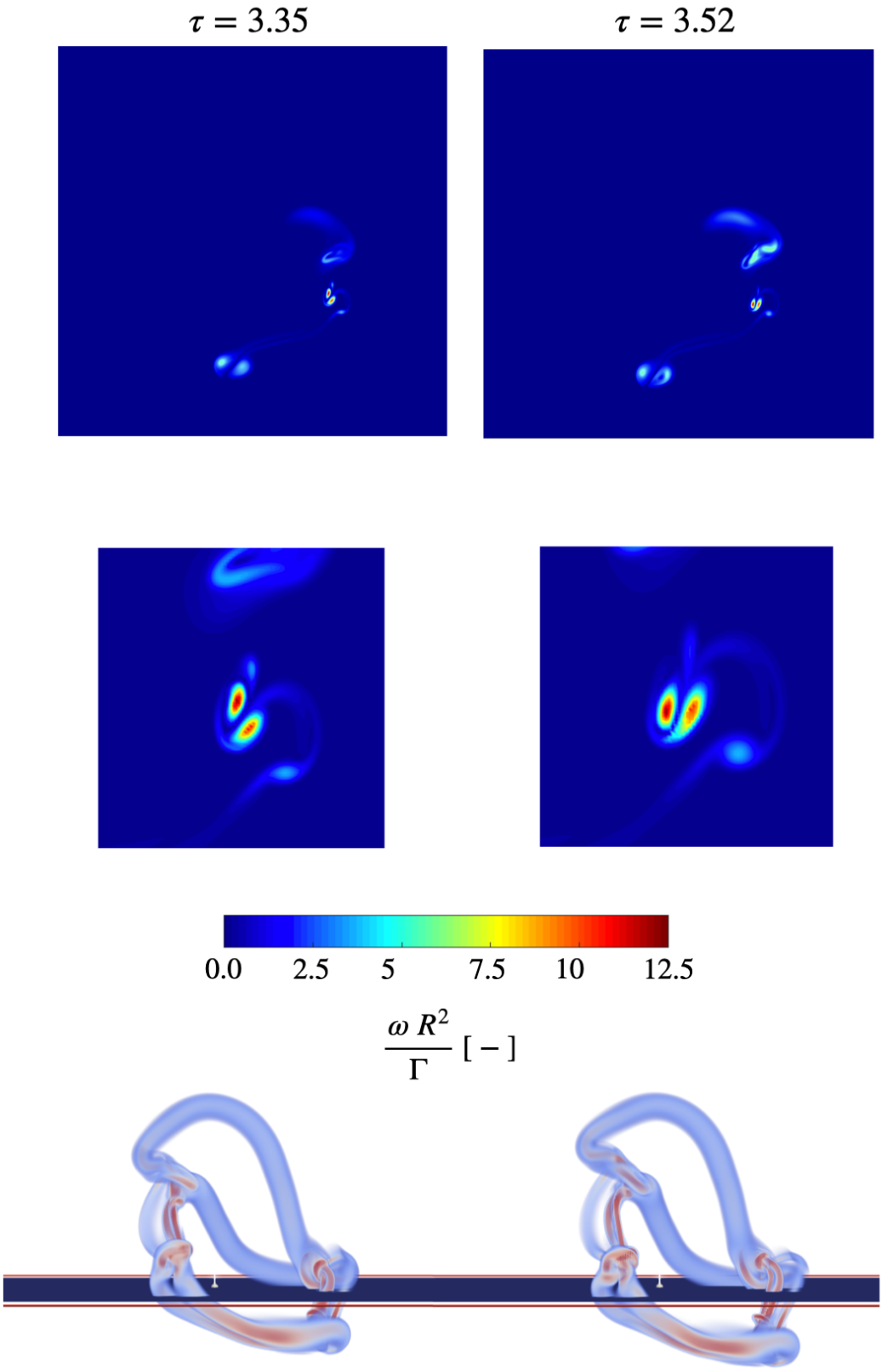

Bibliography

[1] Henry Keith Moffatt. The degree of knottedness of tangled vortex lines. *Journal of Fluid Mechanics*, 35(1):117–129, 1969.

[2] Grigore Călugăreanu. Sur les classes d'isotopie des noeuds tridimensionnels et leurs invariants. *Czechoslovak Mathematical Journal*, 11(4):588–625, 1961.

[3] F. Brock Fuller. The writhing number of a space curve. *Proceedings of the National Academy of Sciences*, 68(4):815–819, 1971.

[4] Martin Scheeler, Dustin Kleckner, Davide Proment, Gordon Kindlmann, and William Irvine. Helicity conservation by flow across scales in reconnecting vortex links and knots. *Proceedings of the National Academy of Sciences*, 111(43):15350–15355, 2014.

[5] Martin Scheeler, Wim M. van Rees, Hridesh Kedia, Dustin Kleckner, and William Irvine. Complete measurement of helicity and its dynamics in vortex tubes. *Science*, 357(6350):487–491, 2017.

[6] Philippe Chatelain, Alessandro Curioni, Michael Bergdorf, Diego Rossinelli, Wanda Andreoni, and Petros Koumoutsakos. Billion vortex particle direct numerical simulations of aircraft wakes. *Computer Methods in Applied Mechanics and Engineering*, 197(13-16):1296–1304, 2008.

[7] Hermann von Helmholtz. *3. Über Integrale der hydrodynamischen Gleichungen, welche den Wirbelbewegungen entsprechen*. De Gruyter, 2020.

[8] Henry Keith Moffatt and Renzo Ricca. Helicity and the călugăreanu invariant. In *Knots And Applications*, pages 251–269. World Scientific, 1995.

[9] Henry Keith Moffatt and Arkady Tsinober. Helicity in laminar and turbulent flow. *Annual review of fluid mechanics*, 24(1):281–312, 1992.

[10] Ming Cheng, Janet Lou, and T.T. Lim. Leapfrogging of multiple coaxial viscous vortex rings. *Physics of Fluids*, 27(3):031702, 2015.

[11] Michael H. Freedman and Zheng-Xu He. Divergence-free fields: energy and asymptotic crossing number. *Annals of Mathematics*, pages 189–229, 1991.

[12] Jérémy Salerno, Philippe Chatelain, Yann Bartosiewicz, Grégoire Winckelmans, and Jean-François Remacle. Simulation of a low prandtl shear layer.

[13] Philippe Chatelain, Matthieu Duponcheel, Denis-Gabriel Caprace, Yves Marichal, and Grégoire Winckelmans. Vortex particle-mesh simulations of vertical axis wind turbine flows: from the airfoil performance to the very far wake. *Wind Energy Science*, 2(1):317–328, 2017.

[14] Martin Scharlemann. Topology of knots. In *Topological aspects of the dynamics of fluids and plasmas*, pages 65–82. Springer, 1992.

[15] Risto Hänninen, Niklas Hietala, and Hayder Salman. Helicity within the vortex filament model. *Scientific reports*, 6(1):1–12, 2016.

UNIVERSITÉ CATHOLIQUE DE LOUVAIN
École polytechnique de Louvain
Rue Archimède, 1 bte L6.11.01, 1348 Louvain-la-Neuve, Belgique | **www.uclouvain.be/epl**